ABSTRACT

Title of Thesis: ANALYSIS OF HELICOPTER FLIGHT DYNAMICS THROUGH MODELING AND SIMULATION OF PRIMARY FLIGHT CONTROL ACTUATION SYSTEM

Degree Candidate: Hunter Barton Nelson

Degree and Year: Master of Science, 2015

Thesis directed by: Professor Roberto Celi
Department of Aerospace Engineering

A simplified second-order transfer function actuator model used in most flight dynamics applications cannot easily capture the effects of different actuator parameters. The present work integrates a nonlinear actuator model into a nonlinear state space rotorcraft model to determine the effect of actuator parameters on key flight dynamics.

The completed actuator model was integrated with a swashplate kinematics where step responses were generated over a range of key hydraulic parameters. The actuator-swashplate system was then introduced into a nonlinear state space rotorcraft simulation where flight dynamics quantities such as bandwidth and phase delay analyzed.

Frequency sweeps were simulated for unique actuator configurations using the coupled nonlinear actuator-rotorcraft system. The software package CIFER was used for system identification and compared directly to the linearized models. As

the actuator became rate saturated, the effects on bandwidth and phase delay were apparent on the predicted handling qualities specifications.

ANALYSIS OF HELICOPTER FLIGHT DYNAMICS THROUGH MODELING AND SIMULATION OF PRIMARY FLIGHT CONTROL ACTUATION SYSTEM

by

Hunter Barton Nelson

Thesis submitted to the Faculty of the Graduate School of the
University of Maryland, College Park in partial fulfillment
of the requirements for the degree of
Masters of Science
2015

Advisory Committee:

Professor Roberto Celi, Chairman/Advisor
Department Chair, Norman Wereley
Gessow Professor and Director of Gessow Rotorcraft Center, Inderjit Chopra

Dedication

To my parents, for teaching me to pursue my dreams.

Acknowledgments

First, I would like to extend my deepest thanks to my advisor, Dr. Roberto Celi. He has opened my eyes to the wonderful field of rotorcraft, and now I will never look back. His support and guidance was invaluable during my time at the University of Maryland.

I would also like to express my sincere gratitude to the members of my committee, Dr. Norman Wereley and Dr. Inderjit Chopra for their guidance and support.

Thanks to all my fellow grad students, Sid Kolluru, Andrew Lind, Jonathan Elliot, Jillian Alfred, Ananth Sridharan, Ondrej Juhasz, John Tritschler, William Staruk, Joseph Schmaus, Shane Boyer, Matt Collett, and Pratik Bhandari for the advice and encouragement. They helped make grad school such an enjoyable expe-rience.

Thank you to my wind tunnel family, Hareen Aparakakankanange, Ahmad Kassaee, Nicholas Kostreski, and Jon Geerts. I would like to express my deepest thanks to Dr. Barlow who has consistently fulfilled my need for knowledge and for challenging me when I was an undergraduate here at the University of Maryland.

Special thank you to Victoria Seng. She has kept me motivated when things get tough, and for that, I owe her so much.

Finally, I would like to thank my parents, who have always supported me in all my endeavors. Their unwavering support has meant everything to me, and I would not be where I am today without them.

Table of Contents

List of Tables vi

List of Figures vii

1 **Background** 1
- 1.1 Introduction . . . 1
- 1.2 Actuators & Flight Dynamics . . . 4
- 1.3 Modeling and Experimentation . . . 5
- 1.4 Rotorcraft System Identification . . . 8
- 1.5 Actuator Modeling and Experimentation . . . 8
- 1.6 Summary . . . 9
- 1.7 Objective of Present Work . . . 10
- 1.8 Outline of Thesis . . . 11

2 **Model Formulation** 13
- 2.1 Overview . . . 13
- 2.2 Modeling . . . 13
  - 2.2.1 Actuator Dynamics . . . 14
  - 2.2.2 Pressure Dynamics . . . 18
  - 2.2.3 Valve Dynamics . . . 21
- 2.3 Isolated Actuator Simulation . . . 25
  - 2.3.1 Differential Equation Overview . . . 25
  - 2.3.2 Actuator Control . . . 26
  - 2.3.3 Flow Smoothing . . . 28
  - 2.3.4 Constraining Actuator Motion . . . 33
  - 2.3.5 Differential & Algebraic Equation Solver Optimization . . . 41
  - 2.3.6 Model Summary . . . 53
- 2.4 Simulation Model . . . 55
  - 2.4.1 Helicopter Model . . . 55
  - 2.4.2 Coupling of Actuator Model and Helicopter Model . . . 59
  - 2.4.3 Trim . . . 60

3 **Analysis of Actuator Dynamics** 72
- 3.1 Overview . . . 72
- 3.2 Results . . . 73
  - 3.2.1 Supply Pressure . . . 74
  - 3.2.2 Valve Pressure Drop . . . 78
  - 3.2.3 Valve Flow Coefficient . . . 82
  - 3.2.4 Piston Area . . . 85
  - 3.2.5 Actuator Test Cases . . . 89

4 **Rotorcraft-Actuator Linearized Model** 94
4.1 Overview . . . 94
4.2 Linearization Methodology . . . 94
4.3 Results . . . 106
4.3.1 Supply Pressure . . . 106
4.3.2 Valve Pressure Drop . . . 111
4.3.3 Valve Flow Coefficient . . . 112
4.3.4 Piston Area . . . 114
4.3.5 Actuator Test Cases . . . 116

5 **Rotorcraft-Actuator Time History Model** 125
5.1 Overview . . . 125
5.2 CIFER . . . 125
5.3 System Identification Methodology . . . 126
5.4 Results . . . 127

6 **Concluding Remarks** 137
6.1 Overview . . . 137
6.2 Conclusion of the Study . . . 138
6.3 Remarks for Future Work . . . 139

List of Tables

2.1 Friction parameters for Eq. (2.3) used in Fig. 2.3 18

2.2 Trimmed swashplate angles in hover compared to swashplate limits from Ref. [1] 40

2.3 Distance to swashplate limits for swashplate in trimmed hover 40

2.4 HeliUM model and environment parameters used for actuator study . 58

2.5 States and inputs for the three swashplate actuators 61

3.1 Actuator configuration for study of supply pressure changes 73

3.2 Supply pressures, P_s, used in study 74

3.3 Valve pressure drops, P_v, used in study. 79

3.4 Valve flow coefficients, c_v, used in study 83

3.5 Piston areas, A_p, used in study 86

3.6 Model parameters for baseline, sluggish, and agile actuator models . . 90

3.7 Model parameters for baseline, sluggish, and agile actuator models . . 90

3.8 Step response rise time and settling time for baseline, sluggish, and agile actuator models 91

3.9 Step response max swashplate rate and max flow rate for baseline, sluggish, and agile actuator models 92

4.1 Supply pressures used in linearized actuator-rotorcraft study 106

4.2 Valve pressure drops used in the present study 111

4.3 Valve flow coefficients used in linearized actuator-rotorcraft study . . 113

4.4 Piston areas used in linearized actuator-rotorcraft study 116

List of Figures

2.1 Diagram of a typical hydraulic servo system, from Ref. [2]. 14

2.2 Hydraulic actuator 15

2.3 Example of Stribeck friction curve 17

2.4 Valve schematic 21

2.5 Example of flow rate Q as a function of normalized valve position . . 28

2.6 Slope of flow rate Q' as a function of normalized valve position 29

2.7 Example plot of flow rate with and without smoothing as a function of normalized valve position. 31

2.8 Example of slope of flow rate with and without smoothing as a function of valve position. 32

2.9 Sign function with and without smoothing. 33

2.10 Normal operation, Flag = 0. 34

2.11 Actuator fully extended and with positive forcing; Flag = 1. 34

2.12 Actuator fully retracted and with negative forcing; Flag = 2. 34

2.13 Actuator fully extended and with negative forcing; Flag = 3. 35

2.14 Actuator fully retracted and with positive forcing; Flag = 4 35

2.15 Constraint logic flow chart. 37

2.16 Example plot of actuator position, velocity, and normalized valve spool when the upper position limit is reached. 47

2.17 Example plot of actuator chamber pressures and flow rates when the upper position limit is reached. 48

2.18 Zoomed plot of normalized valve spool position and actuator chamber pressures and flow rates when the upper position limit is reached (same as in Figs. 2.16 and 2.17 but with an expanded time scale). . . 49

2.19 Optimized constraint logic flow chart 54

2.20 Rotorcraft swashplate angles and axes 64

3.1 Swashplate step response for unit degree step input at low supply pressures . . . 75

3.2 Swashplate step response for unit degree step input at high supply pressures . . . 76

3.3 Rise time (blue) and settling time (green) for swashplate step response over a range of supply pressures . . . 77

3.4 Rise time (blue) and settling time (green) for swashplate step response over a range of supply pressures on a log-log scale . . . 78

3.5 Swashplate step response for unit degree step input at low pressure drops . . . 80

3.6 Swashplate step response for unit degree step input at high pressure drops . . . 81

3.7 Rise time (blue) and settling time (green) for swashplate step response over a range of pressure drops on a log-log scale . . . 82

3.8 Swashplate step response for unit degree step input for low valve flow coefficients . . . 84

3.9 Swashplate step response for unit degree step input for high valve flow coefficients . . . 85

3.10 Rise time (blue) and settling time (green) for swashplate step response over a range of valve flow coefficients . . . 86

3.11 Swashplate step response for unit degree step input over a range of actuator piston areas . . . 87

3.12 Rise time (blue) and settling time (green) for swashplate step response over a range of actuator piston areas . . . 88

3.13 Swashplate step response for unit degree step input for UH-60, baseline, sluggish, and agile actuator models . . . 91

3.14 Swashplate rates for unit degree step input for baseline, sluggish, and agile actuator models . . . 92

3.15 Chamber A flow rate for unit degree step input for baseline, sluggish, and agile actuator models . . . 93

4.1 Overview of linearized test cases . . . 98

4.2 Inputs and outputs of linearized actuator and linearized helicopter dynamics . . . 100

4.3 Solution to input-output problem for test case C . . . 102

4.4 Pitch rate response to longitudinal stick for rotorcraft in hover, using baseline actuator model Case B and Case C . . . 103

4.5 Pitch rate response to longitudinal stick for rotorcraft in hover, using agile actuator model Case B and Case C . . . 104

4.6 Pitch rate response to longitudinal stick for rotorcraft in hover, using sluggish actuator model Case B and Case C . . . 105

4.7 Pitch rate response to longitudinal stick in hover as a function of supply pressure . . . 107

4.8 Roll rate response to lateral stick in hover as a function of supply pressure . . . 108

4.9 Heave response to collective stick in hover as a function of supply pressure . . . 108

4.10 Definitions of bandwidth and phase delay from Ref. [3] . . . 109

4.11 Satisfaction of ADS-33 requirements for small-amplitude pitch and roll attitude changes for target acquisition and tracking, Par. 3.3.2.1, as a function of supply pressure. . . . 110

4.12 Pitch rate response to longitudinal stick in hover as a function of valve pressure drop . . . 112

4.13 Roll rate response to lateral stick in hover as a function of valve pressure drop . . . 113

4.14 Heave response to collective stick in hover as a function of valve pressure drop . . . 114

4.15 ADS-33 requirements for small-amplitude pitch and roll attitude changes for target acquisition and tracking as a function of valve pressure drop 115

4.16 Pitch rate response to longitudinal stick in hover as a function of valve flow coefficient . . . 116

4.17 Roll rate response to lateral stick in hover as a function of valve flow coefficient . . . 117

4.18 Heave response to collective stick in hover as a function of valve flow coefficient . . . 118

4.19 ADS-33 requirements for small-amplitude pitch and roll attitude changes for target acquisition and tracking as a function of valve flow coefficient 119

4.20 Pitch rate response to longitudinal stick as a function of actuator piston area . . . 120

4.21 Roll rate response to lateral stick as a function of actuator piston area 120

4.22 Heave response to collective stick as a function of actuator piston area 121

4.23 ADS-33 requirements for small-amplitude pitch and roll attitude changes for target acquisition and tracking as a function of actuator piston area 121

4.24 Pitch rate response to longitudinal stick for baseline, sluggish, agile, and UH-60 transfer function models . . . 122

4.25 Roll rate response to lateral stick for baseline, sluggish, agile, and UH-60 transfer function models . . . 123

4.26 ADS-33 requirements for small-amplitude pitch and roll attitude changes for target acquisition and tracking for baseline, sluggish, agile, and UH-60 transfer function models . . . 124

5.1 Sample frequency sweep input function . . . 127

5.2 Pitch rate frequency response to longitudinal stick δ_{lon} with no actuator dynamics model, for the numerically linearized model and the model identified using CIFER . . . 128

5.3 Roll rate frequency response to lateral stick δ_{lat} with no actuator dynamics model, for the numerically linearized model and the model identified using CIFER . . . 129

5.4 Pitch rate frequency response to longitudinal stick δ_{lon} with baseline actuator dynamics model, for the numerically linearized model and the model identified using CIFER . . . 130

5.5 Roll rate frequency response to lateral stick δ_{lat} with baseline actuator dynamics model, for the numerically linearized model and the model identified using CIFER . . . 131

5.6 Pitch rate frequency response of HeliUM with sluggish actuator dynamics model, for the numerically linearized model and the model identified using CIFER 132

5.7 Roll rate frequency response of HeliUM with sluggish actuator dynamics model, for the numerically linearized model and the model identified using CIFER 133

5.8 Pitch rate frequency response of HeliUM with agile actuator model, for the numerically linearized model and the model identified using CIFER 134

5.9 Roll rate frequency response of HeliUM with agile actuator model, for the numerically linearized model and the model identified using CIFER 135

5.10 ADS-33 requirements for small-amplitude pitch and roll attitude changes for target acquisition and tracking without actuators (black), baseline (blue), sluggish (red), and agile (green) models derived from numeric linearization (circles) and CIFER (squares) 136

Nomenclature

A	Chamber area
C_h	Chamber hydraulic capacitance
C_{Li}	Internal leakage coefficient
c_v	Valve flow coefficient
D_v	Valve damping coefficient
d_v	Valve spool diameter
E'	Effective bulk modulus
$F_{actuator}$	Actuator force
F_{ext}	External force
F_f	Friction force
f_{hs}	Valve hysteresis
F_{net}	Total force on swashplate
K_p	Proportional gain
l_{ph}	Length of pitch horn
m_{fl}	Pipeline hydraulic fluid mass
$M_{aero,total}$	Total aerodynamic pitching moment over all blades
$M_{i_{x,aero}}$	Aerodynamic moment of blade i
$M_{inertial,total}$	Total inertial pitching moment over all blades
m_p	Piston mass
m_t	Total mass of piston assembly
n_b	Number of blades
P_1, P_2	Line pressures
P	Chamber pressure
P_{eq}	Equalized pressure
ΔP_N	Nominal pressure drop
P_s	Supply pressure
P_T	Tank pressure

$\dot{P}$	Rate of change of chamber pressure
Q	Pipeline volumetric flow rate
Q_{Le}	Volumetric flow rate of external leakage
Q_{Li}	Volumetric flow rate of internal leakage
Q_N	Nominal flow rate
$\tilde{Q}$	Approximate flow rate
$\tilde{Q}'$	Approximate rate of change of flow rate
Q'	Rate of change of flow rate
u_{v}^*	Normalized valve input
V	Chamber volume
V_{pl}	Pipeline volume
$\dot{V}$	Rate of change of chamber volume
x_p	Piston position
$x_{p,0}$	Initial piston position
x_v	Valve spool position
$\dot{x}_v$	Valve spool velocity
$\ddot{x}_v$	Valve spool acceleration
$x_{v,max}$	Max valve stroke
x_1	Piston position
x_2	Piston velocity
x_3	Chamber A pressure
x_4	Chamber B pressure
x_5	Normalized valve spool position
x_6	Normalized valve spool velocity
$\dot{x}_p$	Piston velocity
$\ddot{x}_p$	Piston acceleration

Greek Symbols

α	Ring side to piston side area ratio
α_d	Valve discharge coefficient
θ_{1c}	Lateral cyclic
θ_{1s}	Longitudinal cyclic
θ_{tr}	Tail rotor collective pitch
θ_z	Collective pitch
κ	Swashplate angle to actuator conversion factor
ρ	Hydraulic fluid density
ω_v	Valve natural frequency

Subscripts and Superscripts

$(\,)_A$	Chamber A
$(\,)_B$	Chamber B
$(\,)_{lower}$	Lower bound
$(\,)_{upper}$	Upper bound
$(\,)^*$	Normalized

Abbreviations

AE	Algebraic equation
DAE	Differential-Algebraic equation
ODE	Ordinary differential equation

Chapter 1

Background

1.1 Introduction

Throughout the history of aircraft, control has always been a topic of interest. No matter how impressive the aircraft lift to drag ratio, efficiency, or payload, it all means little if the aircraft is not easily controllable. Traditionally, mechanical flight control systems were used to control the deflection of control surfaces. A combination of cables, pulleys, and pushrods were, and sometimes still are, used to control the ailerons, elevator, and rudder on a fixed wing aircraft, and the swashplate on rotorcraft. This is as pure, and simple, as controlling an aircraft can be. The pilot is in direct control over the control surfaces of the vehicle.

When piloting an aircraft with a pure mechanical flight control system, the pilot must generate the necessary force to deflect the control surfaces, even under high aerodynamic loading. As the size and maneuverability requirements of these aircraft increases, the pilot must apply increasing force to the flight controls in order to overcome the inertial and aerodynamics forces on the flight control surfaces. Eventually, the force becomes too great for sufficient pilot controllability and mechanical assistance is required.

A hydraulic control system, composed of pumps, valves, and actuators is a system designed to decrease pilot workload, and is used on many of today's larger

aircraft and rotorcraft. The pilot control inputs are converted to actuator displacement either via mechanical linkages or, in more advanced aircraft, a fly-by-wire system.

In systems such as these, actuators can be thought of as the fundamental link between the pilot and the machine. Actuators are responsible for deflecting aircraft control surfaces in response to pilot inputs. Because actuators play such an important role in flight, it is important to have a better understanding of how different hydraulic system design parameters influence the flight dynamics characteristics of the aircraft.

With the responsibility of controlling the aircraft, actuators have to meet the performance requirements of the aircraft to ensure pilot controllability. For example, two very important flight dynamics and handling qualities criteria for rotorcraft that are affected by actuator characteristics are its bandwidth and phase delay [3].

Both bandwidth and phase delay are derived from the frequency response of the aircraft or rotorcraft. At frequencies below 1 Hz, flight dynamics are dominated by fundamental rotorcraft flight mechanics, the flight control system, and pilot actively controlling the helicopter [4]. At higher frequencies, actuator dynamics, rigid body elastic airframe modes, and rotor blade modes, all nonlinear, dominate the dynamics at 2 Hz and above [5]. At these high frequencies, it is important to have a robust, high fidelity simulation model, for a firm understanding of all the dynamic interactions taking place.

Bandwidth is a quantity used to describe the pilot authority over an aircraft at higher frequency [3]. This metric is broken down into the different axis, or channels,

the flight control system has authority over. The pitch, lateral, and heave channels are analyzed individually and the bandwidth for each channel is determined. A control system with high bandwidth design is able to respond to fast inputs by the pilot. In general, a larger control system bandwidth is more desirable. If an aircraft bandwidth is too small, the pilot will have difficulty performing maneuvers that require precise, high frequency inputs. On the other hand, a high bandwidth design requires faster and more powerful actuators, increasing complexity and cost.

Phase delay is a measure of the delay, or lag, between pilot input and aircraft response. Just like bandwidth, phase delay is broken down into each channel for analysis. Smaller phase delay is desired for improved control response. As phase delay increases, aircraft response time to a given pilot input increases. If the phase delay is too large, the aircraft response can become so delayed that the pilot has difficulty controlling the aircraft and instabilities can occur.

One issue in flight dynamics, Pilot-Induced Oscillations (PIOs), have been the source of many studies. PIOs, in the most simple definition, are inadvertent oscillations, sustained through the dynamic interaction between the pilot and the aircraft or rotorcraft. Pilot adaptation, or adjustment to the vehicle's dynamics, contributes to this phenomena [6]. Nonlinearities in the control system, such as actuator rate limiting, have been shown to place excessive demands on pilot adaptation. It has been shown that the susceptibility of an aircraft to PIOs can be increased through actuator rate limiting [7].

In flight dynamics, the process of system identification is designed to extract an accurate model of aircraft input-to-output behavior. Up until the early 1990s, con-

ventional time-domain techniques used for fixed-wing aircraft were typically used for rotorcraft, although they are not well suited for this purpose [8, 9]. Rotorcraft dynamics are inherently unstable, nonlinear, and strongly coupled, and measurements are typically noisy, making system identification especially difficult [10]. The Multiple-Input, Multiple-Output (MIMO) response due to high correlation between controls makes isolating a single control channel for system identification even harder. Additionally, rotorcraft have different flight modes including hover and forward flight in which dynamics can be drastically different. During an actual flight test, rotorcraft measurements are prone to contamination from mechanical vibration making data excessively noisy. Now, powerful system identification tools, designed with rotorcraft system identification in mind, are available to accurately extract system models.

1.2 Actuators & Flight Dynamics

Typically in the flight dynamics community, actuators are simply modeled as transfer functions, generally of second order. While this is a computationally efficient way of modeling actuator dynamics, it masks the details required to understand the role different actuator parameters play in the overall flight dynamics of an aircraft. For example, the transfer function

$$\frac{\theta_{1s}}{\delta_{lon}} = \frac{1}{0.00114s^2 + 0.0463s + 1} \tag{1.1}$$

is found in Ref. [1] and describes the swashplate angle response θ_{1s} to a given longitudinal stick displacement input δ_{lon}. While the equation is useful for most

flight dynamics applications, it is not intuitive. What happens if the supply pressure decreases or if the size of the actuator increases? These types of changes to the hydraulic system can not be easily represented by the transfer function in Eq. (1.1) and a new transfer function must be created for each specific application. The transfer function essentially becomes a 'black box' and hides the internal workings of the actuator dynamics.

1.3 Modeling and Experimentation

Modern rotorcraft flight control systems try to achieve high bandwidth, low time delay response characteristics for improved handing qualities. One of the issues that requires special attention is the overall time delay associated with various components. In particular, in a typical pitching maneuver, the primary flight servos can account for 14% of the overall time delay compared to 30% in the rotor [11]. This can leave very little room in the design for delays associated with the stabilization loop without risking rotorcraft stability.

Chen and Hindson investigated the influence of rotor and other high-order dynamics on rotorcraft control system performance. When investigating high bandwidth, high gain controller implementation on a simplified coupled rotor-fuselage CH47 rotorcraft model, delays such as those associated with actuators severely limited the usable values of the feedback gains and thus bandwidth of the control system [12]. As the required bandwidth of flight control systems increases, so does the importance of understanding the high frequency dynamics of rotorcraft systems.

Ballin and Dalang-Secrétan have focused on high frequency, nonlinear rotorcraft dynamics. In this report, a blade element simulation is compared against frequency sweep flight test data to assess the dynamic fidelity of the UH-60 simulation in hover and low-speed flight. In the analysis, no significant nonlinearities were noted between the simulation and flight test, however it is noted that the frequency sweeps used may not have the required input amplitudes to expose the rate limits of the actuators [13].

Fletcher developed a linear state space model for UH-60 flight dynamics in hover and forward flight. The model includes the fuselage rigid body degrees of freedom, rotor flap and lag dynamics as well as engine and governor dynamics. The model uses equivalent time delays on the control inputs to simulate the hydraulic response of the actuators. This results in an accurate rotorcraft simulation over typical handling qualities frequencies of interest, 0.3 to 20 rad/sec, but it does not fully capture the influence of the actuator dynamics on the final model [14].

Mitchell and Sahasrabudhe investigated how to determine aircraft bandwidth in the presence of system nonlinearities. They studied two aircraft models and introduced two common sources of nonlinearity, actuator rate limiting and cockpit control command shaping. The rate limit of the actuator controller was adjusted from 157 deg/sec down to 10 deg/sec and the frequency response of the aircraft was calculated. It was determined that the susceptibility of an airplane to PIOs can be effectively determined from airplane's pitch attitude bandwidth and phase delay, however, these parameters can be difficult to determine in the presence of nonlinearities [15].

A sophisticated state-space nonlinear helicopter model, called HeliUM, is used to model the advanced rotorcraft dynamics relevent for this actuator study. Originally specialized for the UH-60 Black Hawk, HeliUM is a derivation of the GenHel flight dynamics simulation model [23]. The original rotor model was composed of rigid blade flap and lag degrees of freedom. Torsional dynamics were modeled using a psuedo-modal approach and the fuselage was modeled as a rigid body with aerodynamic coefficients of the fuselage and empennage provided by look-up tables [24]. Ballin then improved upon the GenHel model and also implemented an engine model [25]. Kim et al. improved the main rotor inflow model using the Pitt-Peters dynamic inflow model and implemented a new trim procedure using the already available first order state space equations of motion [26]. The rotor modeling was then improved to include an aeroelastic rotor and the coupled rotor/fuselage forumulation [27, 28]. Peters and He finite state wake [29] was then added by Turnour. Currently there are several different upgrades and modifications ongoing to HeliUM, including the addition of actuator dynamics presented in this report, keeping the model as accurate and up-to-date as possible.

The need to understand high frequency rotorcraft dynamics exists. If the design model has inaccuracies, especially at high frequency, the controller's performance degrades leading to reduced maneuverability, performance, and in the worst case, instability. As the technical requirements of rotorcraft increase, it becomes increasingly important to have an accurate actuator mathematical model for improved rotorcraft flight dynamics modeling.

1.4 Rotorcraft System Identification

In flight dynamics, the process of system identification is designed to extract an accurate model of aircraft input-to-output behavior. Up until the early 1990s, conventional time-domain techniques used for fixed-wing aircraft were typically used for rotorcraft, although they are not well suited for this purpose [**?** 9]. Rotorcraft dynamics are inherently unstable, nonlinear, and strongly coupled, and measurements are typically noisy, making system identification especially difficult [10]. The Multiple-Input, Multiple-Output (MIMO) response due to high correlation between controls makes isolating a single control channel for system identification even harder. Additionally, rotorcraft have different flight modes including hover and forward flight in which dynamics can be drastically different. Finally, during an actual flight test, rotorcraft measurements are prone to contamination from mechanical vibration making data excessively noisy. Now, powerful system identification tools, designed with rotorcraft system identification in mind, are available to accurately extract system models.

1.5 Actuator Modeling and Experimentation

Hydraulic servo systems are well documented in literature. Nikiforuk et al. present a detailed analysis of a two-state electrohydraulic flow-control valve [16]. Typically, the frequency response characteristics of the valve load, i.e. the actuator, occur on a much smaller scale than that of the servo valve so the system dynamics can be summarized by those of the load. On some occasions, the response charac-

teristics of load reach high frequencies requiring a detailed valve mathematic model [16]. Various effects including spool acceleration force, viscous friction forces, flow reaction forces, leakage flow, and compressibility are documented. This model highlights the need for more detailed nonlinear valve models in order to more accurately describe servo actuator dynamics.

Valve dynamics are only one portion of the overall hydraulic system. Van Schothorst details a very detailed hydraulic servo system model for long stroke flight simulator motion control. Limits on the performance of hydraulic systems become apparent as performance demands of simulators increase [17]. Nonlinearities in the valve, pipeline, and actuator dynamics are analyzed and a linear model is obtained, describing the dynamic behavior of the hydraulic servo system. The modeling of the transmission lines between the valve and actuator becomes important as the length of the actuator stroke increases, as is the case with flight simulator motion control.

1.6 Summary

Many helicopter simulation models do not include hydraulic actuator dynamics. When these are integrated, the model is typically limited to an input delay or to a transfer function, usually of second order. This technique is sufficient for most applications but as rotorcraft performance requirements increase, the need for a more accurate actuator model may arise.

Actuator delay is especially important to understand. Instabilities in the presence of a high bandwidth controller can arise as the delay between the actuator and

rotor response to pilot input increases. As controller design places more demand on the hydraulic servo system, delays and discrepancies in the model used to design the controller can lead to degraded performance. Typically, stability augmentation system gains resulting from flight tests are often well below the originally designed and predicted values [12]. With an improved nonlinear hydraulic servo system model integrated into rotorcraft models, the coupled dynamics of actuator, rotorcraft, and controller design can be better understood and higher performance systems can be designed.

1.7 Objective of Present Work

The objectives of the present work are:

1. To describe the formulation of a state space, physics based, nonlinear hydraulic servo actuator model.

2. To analyze key parameters in the hydraulic servo model and quantify their effects on actuator time and frequency domain responses.

3. To integrate the hydraulic servo actuator model into a state space nonlinear helicopter simulation model.

4. To quantify the effects of key hydraulic servo actuator design parameters on rotorcraft flight dynamics quantities of interest such as bandwidth and phase delay.

The work presented in this thesis describes a hydraulic servo system consisting of valve and actuator dynamics. An empirical second order model is used to describe valve dynamics, and accounts for both internal friction and hysteresis. Pressure dynamics in the actuator are calculated using the continuity equation including the effects of fluid compressibility. Actuator dynamics are determined via Newton's second law and a force summation including chamber pressures, friction on the piston, and external forcing. The model is integrated with HeliUM, a state space nonlinear rotorcraft flight dynamics simulation model. A linearized dynamic analysis of coupled actuator and rotorcraft dynamics are carried out with models obtained using numerical linearization and frequency domain system identification. Rotorcraft performance is quantified through the use of frequency response data and handling qualities metrics. The effects of nonlinearities due to displacement and rate saturation on the dynamics of the rotorcraft are also studied in detail.

1.8 Outline of Thesis

Chapter 2 discusses the development of the models of the hydraulic servo system and of the helicopter, as well as the steps taken to integrate the two models. Various issues associated with actuator saturation are also discussed. In Chapter 3, results of the actuator study are presented. Time and frequency domain actuator response data is presented for various actuator configurations. Frequency response data for the integrated actuator rotorcraft dynamics study is presented in Chapter 4. Both numerical linearization and system identification are compared. Chapter 6

presents the main conclusions of the study, as well as suggestions for future research.

Chapter 2

Model Formulation

2.1 Overview

The hydraulic servo system can be seen as a complex balance of energy in the form of fluid flow rate and pressure. At one end of the system, a hydraulic pump supplies hydraulic fluid at a prescribed pressure to the valve where it is redirected to a hydraulic actuator. Depending on the control input to the valve, the pressure supplied by the pump is diverted to an actuator chamber and used to translate the actuator piston fore and aft. This process of moving an actuator is well understood and can be modeled using some basic principles and underlying assumptions. Modeling the hydraulic servo system is the first step to a deeper understanding of actuator dynamics and optimization.

2.2 Modeling

A hydraulic servo system consists of four main elements that combine to convert hydraulic energy generated by the power source into useful mechanical work. A hydraulic servo system consists of the following four elements:

- Power Supply
- Control Elements

- Actuating Elements
- Miscellaneous Elements

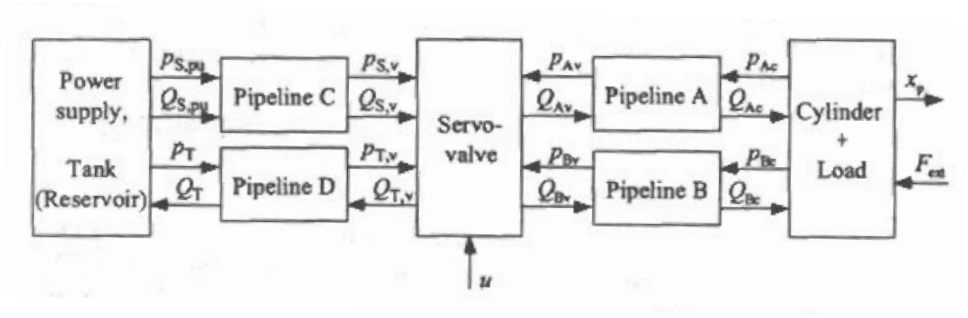

Fig. 2.1: Diagram of a typical hydraulic servo system, from Ref. [2].

The power supply is responsible for supplying hydraulic power to the system. This power is in the form of a supply pressure created by a pump and is converted to mechanical work by the actuating element. The control elements, in the form of valves, are responsible for controlling the direction, amount, and pressure of fluid flow to the actuator. The actuating elements are responsible for converting this hydraulic energy into usable mechanical energy. Actuating elements can either have linear output (cylinders, rams, jacks) or rotary output (rotary actuators, motors). Details on the dynamics of each of these components can be found below.

2.2.1 Actuator Dynamics

The actuator is the end of the hydraulic servo system chain and is responsible for the output of the entire system. After hydraulic pressure is produced by the pump and controlled by the valve, the actuator harnesses this energy, in the form of a pressure differential, and converts it to linear or rotary motion. On helicopters,

a group of linear actuators, or hydraulic cylinders, are responsible for tilting the swashplate, which changes azimuthal blade pitch.

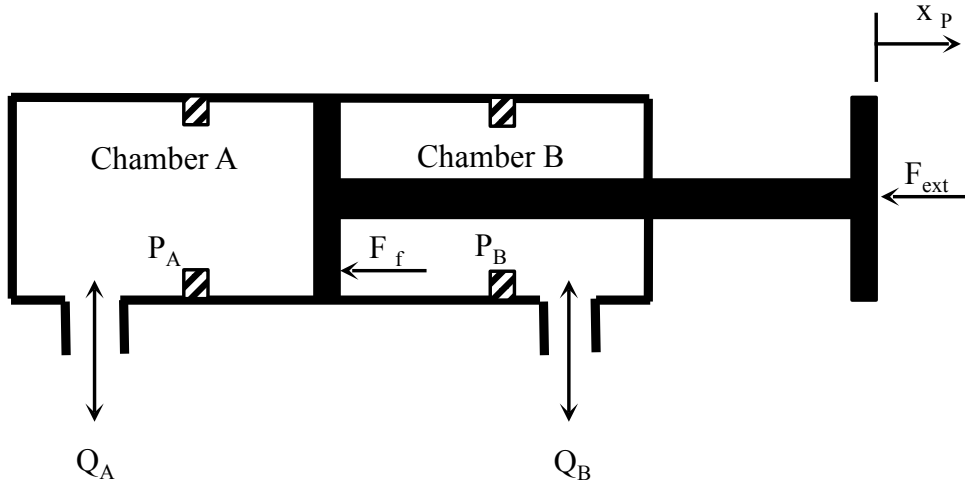

Fig. 2.2: Hydraulic actuator

A linear actuator, also known as a hydraulic cylinder, consists of a cylinder with two chambers and a piston. In this model, the chambers will be called chamber A and chamber B, shown schematically in Fig. 2.2. The differential pressure between the two chambers creates a force imbalance, resulting in the movement of the piston. This pressure differential is controlled independently by two pipelines connected to the valve.

The actuator dynamics can be modeled quite easily by applying Newton's Second Law. The forces acting on the piston include the pressure differential between chambers, friction, and external forcing on the piston rod such that

$$m_t \ddot{x}_p = P_A A_A - P_B A_B - F_f - F_{ext} \tag{2.1}$$

where m_t and $\ddot{x}_p$ are the total mass and acceleration of the piston. Chamber pressures are represented by P_A and P_B while chamber areas are represented by A_A and

A_B, F_f is the friction force generated from the actuator velocity, and F_{ext} is the external load applied to the end of the actuator rod.

In order for the actuator force to be applied, the actuators piston must run through the center of one of the chambers as illustrated in Figure 2.2 at the beginning of this chapter. To simplify calculations,

$$\alpha = \frac{A_B}{A_A}$$

where α is the ratio of the internal cross-section area of chamber B to that of chamber A.

The area A_A can now be represented by the more general A_p, piston area. We can now simplify Eq. (2.1) to

$$m_t \ddot{x}_p = (P_A - \alpha P_B)A_p - F_f - F_{ext}. \tag{2.2}$$

The external force, F_{ext}, allows this model to interact dynamically with its surrounding. When integrated with a helicopter simulation, this force will be derived from blade forces and moments transferred through blade pitch links to the swashplate and applied to each actuator.

The Stribeck friction curve [18]

$$F_f = \sigma \dot{x}_p + \text{sign}(\dot{x}_p)\left[F_{c0} + F_{s0}\exp\left(-\frac{|\dot{x}_p|}{c_s}\right)\right] \tag{2.3}$$

is used to calculate the friction force F_f. The piston velocity is represented by $\dot{x}_p$. The other parameters, σ, F_{c0},F_{s0}, and c_s are determined experimentally. The

quantity $\text{sign}(\dot{x}_p)$ is defined as,

$$\text{sign}(\dot{x}_p) = \begin{cases} 1 & \text{if } \dot{x}_p > 0 \\ 0 & \text{if } \dot{x}_p = 0 \\ -1 & \text{if } \dot{x}_p < 0 \end{cases} \tag{2.4}$$

Figure 2.3 shows an example friction curve for the parameters in Table 2.1. Note that different parameters were used for positive piston velocity and negative piston velocity.

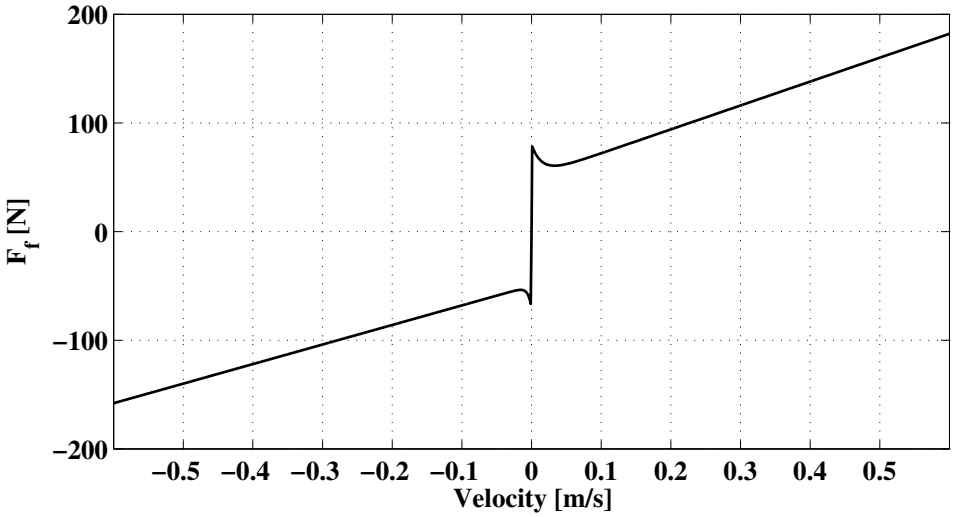

Fig. 2.3: Example of Stribeck friction curve

The total mass of the piston is given by

$$m_t = m_p + m_{A,fl} + m_{B,fl}$$

where m_p is piston mass and $m_{A,fl}$ and $m_{B,fl}$ represent hydraulic fluid mass in pipelines A and B, respectively.

Friction Parameter	$\dot{x}_p > 0$	$\dot{x}_p < 0$
$\sigma\ [\frac{Ns}{m}]$	220	180
$F_{c0}\ [N]$	50	50
$F_{s0}\ [N]$	30	20
$c_s\ [\frac{m}{s}]$	0.015	0.005

Table 2.1: Friction parameters for Eq. (2.3) used in Fig. 2.3

Hydraulic fluid mass in pipeline A and B are calculated below by multiplying hydraulic fluid density by the sum of pipeline and chamber volumes using [2]

$$m_{A,fl} = \rho[V_{pl,A} + (x_{p,0} + x_p)A_p] \tag{2.5}$$

$$m_{B,fl} = \rho[V_{pl,B} + (x_{p,0} - x_p)\alpha A_p] \tag{2.6}$$

where ρ is the density of the hydraulic fluid, $V_{pl,A}$ and $V_{pl,B}$ are the pipeline volumes from the pump and reservoir to chambers A and B, respectively, $x_{p,0}$ is the initial piston position, and x_p is the current piston position.

With Eq. (2.2), the dynamics of the piston can be modeled and understood. The driving inputs to the actuator equation are the chamber pressures P_A and P_B detailed below.

2.2.2 Pressure Dynamics

Pressure dynamics for each chamber in the actuator must be calculated independently by applying the continuity equation. Pressure is a function of volumetric flow rate, fluid leakage, and change in chamber volume. If a fluid, with some posi-

tive flow rate Q, is forced into a constant volume, the pressure of that fluid changes. Alternatively, if the fluid is forced into an expandable volume and held at a constant pressure, that control volume will expand. To start analyzing pressure dynamics, the continuity equation [2]

$$Q_A - Q_{Li} = \dot{V}_A + \frac{V_A}{E'(P_A)}\dot{P}_A \tag{2.7}$$

$$Q_B + Q_{Li} - Q_{Le} = \dot{V}_B + \frac{V_B}{E'(P_B)}\dot{P}_B \tag{2.8}$$

is applied. The terms Q_A and Q_B represent the volumetric flow rate of pipelines A and B, Q_{Li} is the volumetric flow rate of internal leakage and Q_{Le} is the volumetric flow rate of external leakage, V_A and $\dot{V}_A$ are the volume and rate of change of volume of chamber A, while V_B and $\dot{V}_B$ are the volume and rate of change of volume of chamber B, E' is the effective bulk modulus, $\dot{P}_A$ is the rate of change of pressure in chamber A, and $\dot{P}_B$ is the rate of change of pressure in chamber B.

The flow Q_{Li} can be calculated using [2]

$$Q_{Li} = C_{Li}(P_B - P_A)$$

i.e., it is a function of the pressure differential between chambers A and B with C_{Li} representing the internal leakage coefficient. External leakage, Q_{Le}, will be assumed to be small, and will be neglected for the rest of this discussion.

Volumes for chambers A and B are calculated similarly to Eqs. (2.5) and (2.6), and can be further simplified by assuming that the initial piston position, $x_{p,0}$, is

zero. The volumes are given by

$$V_A = V_{pl,A} + (x_{p,0} + x_p)A_p = V_{pl,A} + x_p A_p \tag{2.9}$$

$$V_B = V_{pl,B} + (x_{p,0} - x_p)\alpha A_p = V_{pl,B} - x_p \alpha A_p \tag{2.10}$$

Taking the derivative of Eqs. (2.9) and (2.10) yields

$$\dot{V}_A = A_p \dot{x}_p \tag{2.11}$$

$$\dot{V}_B = -\alpha A_p \dot{x}_p \tag{2.12}$$

Equations (2.11) and (2.12) represent the rate of change of each chamber volume respectively.

The effective bulk modulus, $E'(P)$, is given by [19]

$$E'(P) = a_1 E_{max} log_{10}\left(a_2 \frac{P}{P_{max}} + a_3\right)$$

This equation was derived empirically and is commonly used to calculate the effective bulk modulus for hydraulic cylinders [2]. Parameters $a_1 = 0.5$, $a_2 = 90$, $a_3 = 3$, $E_{max} = 18000$ bar, and $P_{max} = 280$ bar were determined empirically and account for the effects of entrained air as well as mechanical compliance.

Equations (2.7) and (2.8) can be rearranged as

$$\dot{P}_A = \frac{1}{C_{h,A}}(Q_A - A_p \dot{x}_p + Q_{Li}) \tag{2.13}$$

$$\dot{P}_B = \frac{1}{C_{h,B}}(Q_B + \alpha A_p \dot{x}_p - Q_{Li}) \tag{2.14}$$

to solve for $\dot{P}_A$ and $\dot{P}_B$ directly. Hydraulic capacitances, $C_{h,A}$ and $C_{h,B}$, are defined

as

$$C_{h,A} = \frac{V_A}{E'(P_A)} \tag{2.15}$$

$$C_{h,B} = \frac{V_B}{E'(P_B)} \tag{2.16}$$

Equations 2.13 and 2.14 are two additional differential equations that will be included in the final nonlinear state space actuator model.

2.2.3 Valve Dynamics

The valve is responsible for controlling the flow of hydraulic fluid to and from the actuator. In this simulation, the valve has two ports for supply and tank pressure and two ports leading to chambers A and B on the actuator. The valve spool, running down the center of the valve, controls the connection and flow of hydraulic fluid between each port, as shown in Fig. 2.4. The linear position of the valve spool determines the hydraulic flow rates between the actuator chambers, pump, and reservoir.

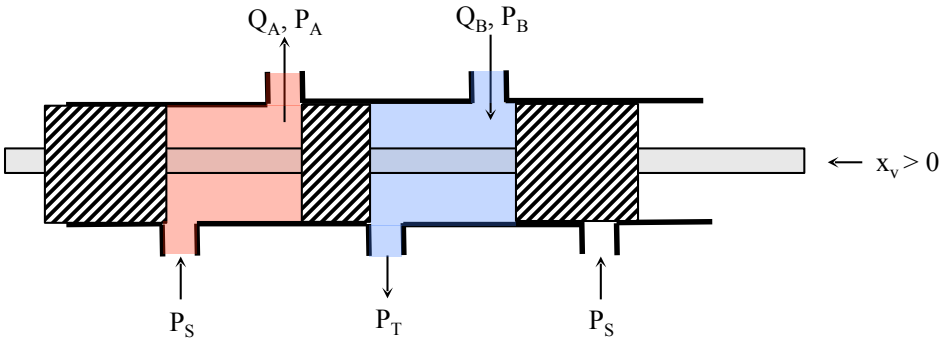

Fig. 2.4: Valve schematic

To solve for flow rates Q_A and Q_B, we must look at the dynamics of the valve.

Typically, the orifice equation is used to describe fluid flows through orifices such as those found in a valve. The flow rate through one orifice in the valve is given by [2]

$$Q = c_v x_v \text{sign}(P_1 - P_2)\sqrt{|P_1 - P_2|} \tag{2.17}$$

where c_v is the valve flow coefficient, x_v is the valve spool position, and P_1 and P_2 are line pressures on each side of the orifice. This equation assumes the orifices are round.

The valve flow coefficient is defined as [2]

$$c_v = \pi d_v \alpha_d \sqrt{\frac{2}{\rho}} \tag{2.18}$$

where d_v is the valve spool diameter, α_d is the valve discharge coefficient, and ρ is the fluid density.

Using valve specifications, the discharge coefficient can be calculated using [2]

$$\alpha_d = \frac{Q_N}{A(x_{v,max})\sqrt{\frac{\Delta P_N}{\rho}}}. \tag{2.19}$$

In the above equation, Q_N represents the nominal flow rate of the valve, ΔP_N is the nominal pressure drop across the valve, and $A(x_{v,max})$ is the maximum area of the valve orifice.

The valve flow coefficient, c_v, can also be calculated using valve manufacturer specifications from the equation [2]

$$c_v = \frac{Q_N}{\sqrt{\frac{\Delta P_N}{2}}} \frac{1}{x_{v,max}}. \tag{2.20}$$

Equation (2.17) takes into account both the magnitude and the direction of the pressure difference between two fluid lines. This equation can be extended to

describe the behavior of a valve where positive movements of the valve spool, x_v, result in different equations than negative movements using

$$Q_A = \begin{cases} c_{v,1} x_v \text{sign}(P_s - P_A)\sqrt{|P_s - P_A|} & \text{if } x_v \geq 0 \\ \\ c_{v,2} x_v \text{sign}(P_A - P_T)\sqrt{|P_A - P_T|} & \text{if } x_v < 0 \end{cases} \tag{2.21}$$

where P_s is the supply pressure from the pump and P_T is the reservoir pressure from the tank.

Equation (2.21) describes the changes in pipeline A connections that occur when the valve spool is moved from center. When a positive valve spool displacement occurs, pipeline A, leading to chamber A, is connected to the supply pressure, P_s. If the valve spool displacement is negative, pipeline A is connected to the reservoir, or tank pressure, P_T. Both equations vary linearly with valve displacement and can be combined as follows.

$$\begin{aligned} Q_A = {} & c_{v,1}\text{sg}(x_v)\text{sign}(P_s - P_A)\sqrt{|P_s - P_A|} \\ & - c_{v,2}\text{sg}(-x_v)\text{sign}(P_A - P_T)\sqrt{|P_A - P_T|} \end{aligned} \tag{2.22}$$

$$\begin{aligned} Q_B = {} & c_{v,3}\text{sg}(-x_v)\text{sign}(P_s - P_B)\sqrt{|P_s - P_B|} \\ & - c_{v,4}\text{sg}(x_v)\text{sign}(P_B - P_T)\sqrt{|P_B - P_T|} \end{aligned} \tag{2.23}$$

These expressions combine the piecewise Eq. (2.21) into one equation using $\text{sg}(x_v)$ defined as

$$\text{sg}(x) = \begin{cases} x & \text{if } x \geq 0 \\ \\ 0 & \text{if } x < 0. \end{cases} \tag{2.24}$$

Modeling of valves, in particular the valve spool dynamics, is more complex than both actuator and pressure dynamics. Valve dynamics are highly nonlinear due to the effects of dead band, saturation, hysteresis, response sensitivity, reversal error, repeatability, flow induced forces, and friction forces [2]. Valve manufacturers release step response and frequency response of specific valves, which can be used to develop simple model approximations of valves. For this simulation, a second order approximation [2]

$$\ddot{x}_{\mathrm{v}}^{*} = \omega_{\mathrm{v}}^{2}\left(u_{\mathrm{v}}^{*} - \frac{2D_v}{\omega_v}\dot{x}_{\mathrm{v}}^{*} - x_{\mathrm{v}}^{*} - f_{hs}sign(\dot{x}_{\mathrm{v}}^{*})\right) \tag{2.25}$$

was used. In Eq. (2.25), x_{v}^{*}, $\dot{x}_{\mathrm{v}}^{*}$, and $\ddot{x}_{\mathrm{v}}^{*}$ are normalized valve spool position, velocity, and acceleration, respectively, ω_v and D_v are the natural frequency and damping coefficient of the valve, f_{hs} is the valve hysteresis coefficient, and u_{v}^{*} is the normalized valve input.

The normalized valve input, u_{v}^{*}, dictates the desired position of the valve spool, from -1 to 1. The valve states are normalized using

$$x_{\mathrm{v}}^{*} = \frac{x_v}{x_{v,max}} \tag{2.26}$$

$$\dot{x}_{\mathrm{v}}^{*} = \frac{\dot{x}_v}{x_{v,max}} \tag{2.27}$$

$$\ddot{x}_{\mathrm{v}}^{*} = \frac{\ddot{x}_v}{x_{v,max}} \tag{2.28}$$

where $x_{v,max}$ is max valve spool displacement.

This second order differential equation describes normalized valve spool position, x_{v}^{*}, as a function of normalized valve input, u_{v}^{*}. This equation starts the sequence of events eventually leading to actuator displacement. When the pilot

moves the control stick, inputs will be sent to the valve ultimately leading to a desired actuator displacement. With the hydraulic system basics modeled, we can now begin to solve these equations to simulate various valve input-output responses.

2.3 Isolated Actuator Simulation

With the equations governing actuator, pressure, and valve dynamics laid out, we can now solve for the time histories of these quantities.

2.3.1 Differential Equation Overview

Before solving the equations that describe the actuator dynamics, it is important to point out the key assumptions used to simplify the model.

- Supply pressure, P_s, and tank pressure, P_T are constant
- Flow through the valve is considered turbulent
- Leakage flow is laminar
- Pipeline dynamics are neglected

Equations (2.2), (2.13), (2.14), and (2.25) can all be converted to first order implicit form. The implicit differential equations below are ready to be input into the differential equation solver and used to model actuator dynamics.

$$0 = \dot{x}_1 - x_2 \tag{2.29}$$

$$0 = m_t\dot{x_2} - (x_3 - \alpha x_4)A_p + F_f(x_2) + F_{ext} \tag{2.30}$$

$$0 = V_A(x_1)\dot{x_3} - E'(x_3)[Q_A(x_3, x_5) - A_p x_2 + Q_{Li}(x_3, x_4)] \tag{2.31}$$

$$0 = V_B(x_1)\dot{x_4} - E'(x_4)[Q_B(x_4, x_5) + \alpha A_p x_2 - Q_{Li}(x_3, x_4)] \tag{2.32}$$

$$0 = \dot{x}_5 - x_6 \tag{2.33}$$

$$0 = \dot{x}_6 - \omega_{\mathrm{v}}^2 \left[u_1 - \frac{2D_v}{\omega_v} x_6 - x_5 - f_{hs} sign(x_5)\right] \tag{2.34}$$

In the process of converting the equations, different properties have been converted to numbered states as follows:

$x_1 \equiv x_p$	piston position
$x_2 \equiv \dot{x}_p$	piston velocity
$x_3 \equiv P_A$	chamber A pressure
$x_4 \equiv P_B$	chamber B pressure
$x_5 \equiv x_{\mathrm{v}}^*$	normalized valve spool position
$x_6 \equiv \dot{x}_{\mathrm{v}}^*$	normalized valve spool velocity
$u_1 \equiv u_{\mathrm{v}}^*$	normalized valve input

2.3.2 Actuator Control

The normalized valve input, u_1, dictates the position of the valve spool, ultimately determining the velocity of the actuator. When $u_1 = 1$, the actuator will be

moving full speed in the positive direction and when $u_1 = -1$, the actuator will be moving full speed in the negative direction. When the input $u_1 = 0$, the actuator remains at rest. In many applications where hydraulic control is used, including aerospace, the operator is not interested in controlling the velocity of the actuator. Instead, the operator is interested in the final displacement position of the actuator.

When piloting a rotorcraft, the pilot's stick displacement corresponds to a particular swashplate displacement. When the pilot holds the stick at a particular position, unless there are separate flight control system inputs, the swashplate holds in a particular position. Because of this behavior, it is important to add a controller to the hydraulic system.

In this case, a proportional gain controller was implemented. This controller simply calculates the error between desired and actual actuator position to determine the magnitude of valve input required to reach the pilot's desired actuator position. Valve input can be calculated using

$$u_1 = K_p(u_{1_d} - x_1) \tag{2.35}$$

where K_p is the proportional gain. This controller is kept as simple as possible to minimize the effects on the dynamics of the hydraulic servo system.

In physical applications, a linear variable differential transformer, or LVDT, is used to determine an actuator position [20]. This reading can be sent to a valve with an integrated controller that determines the required valve spool input to achieve the desired actuator displacement. The controller described in Equation 2.35 is behaving as the valve model's integrated controller.

2.3.3 Flow Smoothing

When integrating the equations of motion of the actuator, the ODE solver can run into numerical difficulties due to discontinuities in some equations. The equations for flow rate, Eqs. (2.22) and (2.23), both contain discontinuities in their derivative. As valve position moves from positive to negative, the slope of the flow rate vs. valve position curve jumps at $x_{\mathrm{v}}^{*} = 0$, as illustrated in Figs. 2.5 and 2.6.

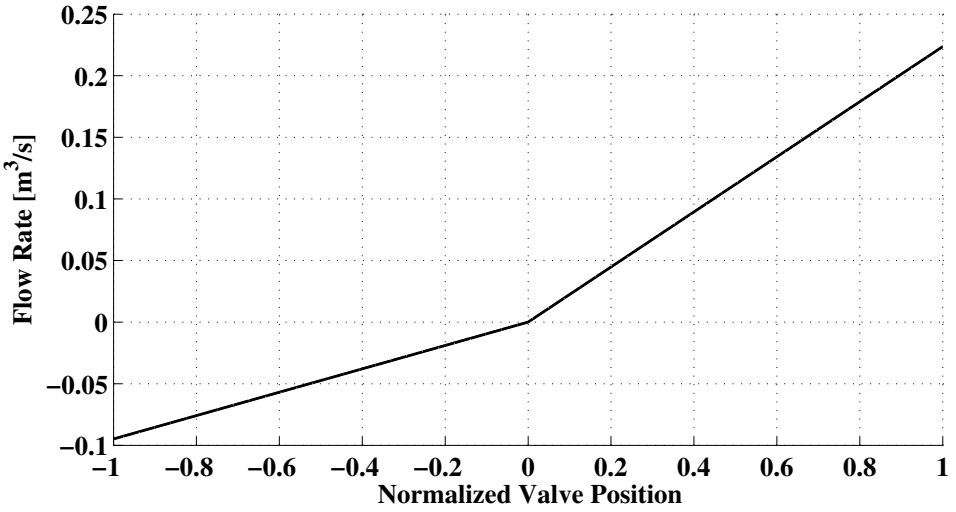

Fig. 2.5: Example of flow rate Q as a function of normalized valve position

This sharp change in slope leads to problems with convergence. To solve this problem, the flow rate was approximated by a continuous spline between the constant slopes of the flow rate while maintaining flow rate equal to zero at zero normalized valve position, e.g., $Q_A = 0$ at $x_{\mathrm{v}}^{*} = 0$.

To create the spline, a third order polynomial

$$\tilde{Q}' = Ax + Bx^2 + C \tag{2.36}$$

was fit between two points, a distance $\pm\Delta x$ from the origin of the flow rate slope.

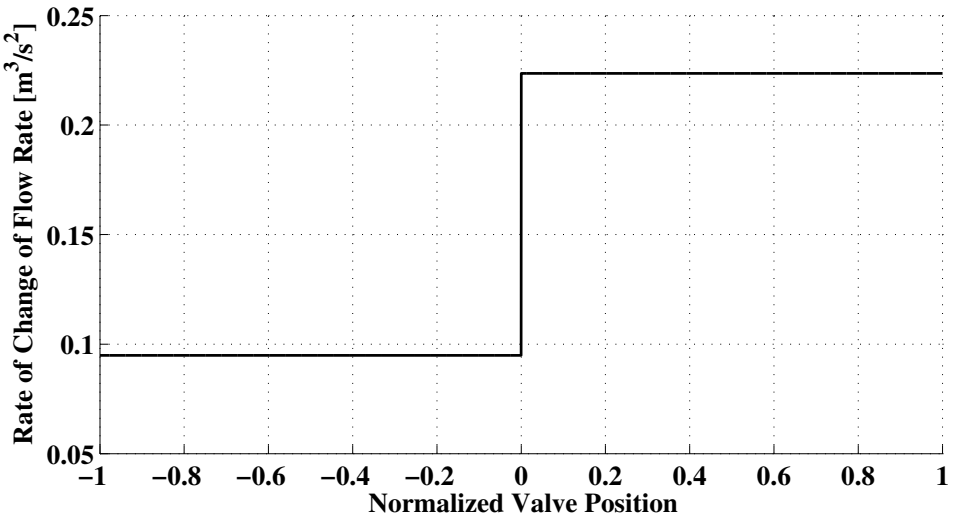

Fig. 2.6: Slope of flow rate Q' as a function of normalized valve position

Larger values of Δx create smoother splines but increase the relative error between the actual and approximated rate of change of flow rate. The constraints

$$\tilde{Q}'(0) = \frac{Q'(\Delta x) + Q'(-\Delta x)}{2} \tag{2.37}$$

$$\tilde{Q}''(\Delta x) = 0 \tag{2.38}$$

$$\tilde{Q}''(-\Delta x) = 0 \tag{2.39}$$

$$\tilde{Q}'(\Delta x) = Q'(\Delta x) \tag{2.40}$$

$$\tilde{Q}'(-\Delta x) = Q'(-\Delta x) \tag{2.41}$$

were used to determine A, B, and C, where $\tilde{Q}'$ is the approximate rate of change of flow rate, and $\tilde{Q}''$ is the approximate derivative.

Solving Eq. (2.36) using constraint Eqs. (2.37) through (2.41) yields the following equations:

If $\mathbf{x}_v^* > \mathbf{0}$

$$A = -2B\Delta x \tag{2.42}$$

$$B = \frac{C - Q'(\Delta x)}{\Delta x^2} \tag{2.43}$$

$$C = \frac{Q'(\Delta x) - Q'(-\Delta x)}{2} \tag{2.44}$$

If $\mathbf{x}_v^* < \mathbf{0}$

$$A = 2B\Delta x \tag{2.45}$$

$$B = \frac{C - Q'(-\Delta x)}{\Delta x^2} \tag{2.46}$$

$$C = \frac{Q'(\Delta x) - Q'(-\Delta x)}{2} \tag{2.47}$$

The coefficients are different depending on the sign of x_v^* since the slope of the flow rate, $Q'(\pm\Delta x)$ changes for positive and negative values of Δx.

The value of Q' can be obtained by taking the derivative of Eqs. (2.22) and (2.23) with respect to x_v^*. Doing so eliminates the $sg(x_v)$ and $sg(-x_v)$ function. In order to preserve the sign change associated with $sg(-x_v)$ that is lost when taking the derivative, Equations 2.50 and 2.51 have each had their signs reversed.

If $\mathbf{x}_v^* > \mathbf{0}$

$$Q'_A = c_{v,1} sign(P_s - P_A)\sqrt{|P_s - P_A|} \tag{2.48}$$

$$Q'_B = c_{v,4} sign(P_B - P_T)\sqrt{|P_B - P_T|} \tag{2.49}$$

If $\mathbf{x}_v^* < \mathbf{0}$

$$Q'_A = c_{v,2} sign(P_A - P_T)\sqrt{|P_A - P_T|} \tag{2.50}$$

$$Q'_B = c_{v,3} sign(P_s - P_B)\sqrt{|P_s - P_B|} \tag{2.51}$$

Now, these equations can be substituted back into Eq. (2.36) to solve for $\tilde{Q}'$.

$$\tilde{Q}' = Ax + Bx^2 + C \tag{2.52}$$

And flow rates Q_A and Q_B can be estimated by multiplying the estimated slope by normalized valve position.

$$\tilde{Q}_A = \tilde{Q}'_A x_{\mathrm{v}}^* \tag{2.53}$$

$$\tilde{Q}_B = \tilde{Q}'_B x_{\mathrm{v}}^* \tag{2.54}$$

These approximations are used for $-\Delta x \leq x_{\mathrm{v}}^* \leq \Delta x$, otherwise Eqs. (2.22) and (2.23) are used. The smoothed approximations are compared to the original in Figs. 2.7 and 2.8.

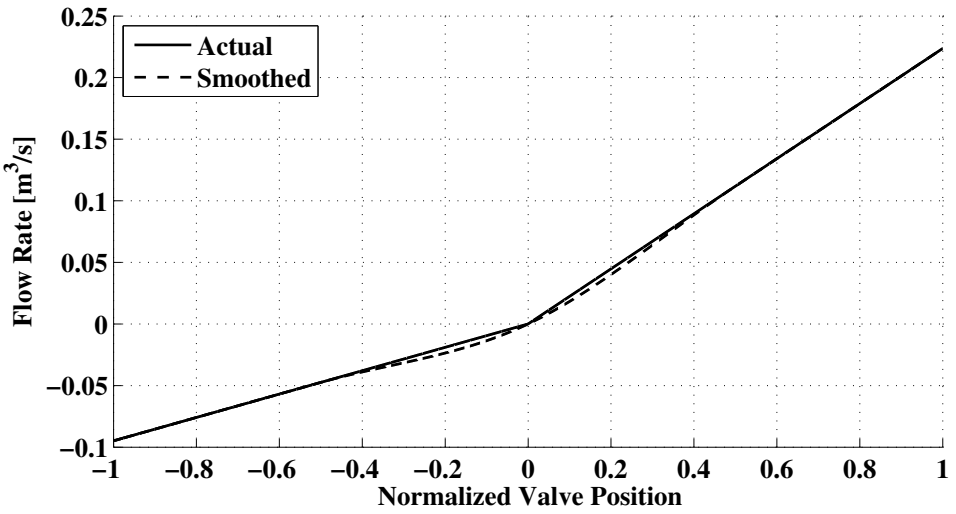

Fig. 2.7: Example plot of flow rate with and without smoothing as a function of normalized valve position.

In these plots, $\Delta x = 0.5$ to emphasize the smoothing and during simulation, Δx is typically much smaller. While the changes to Fig. 2.7 are subtle, the much

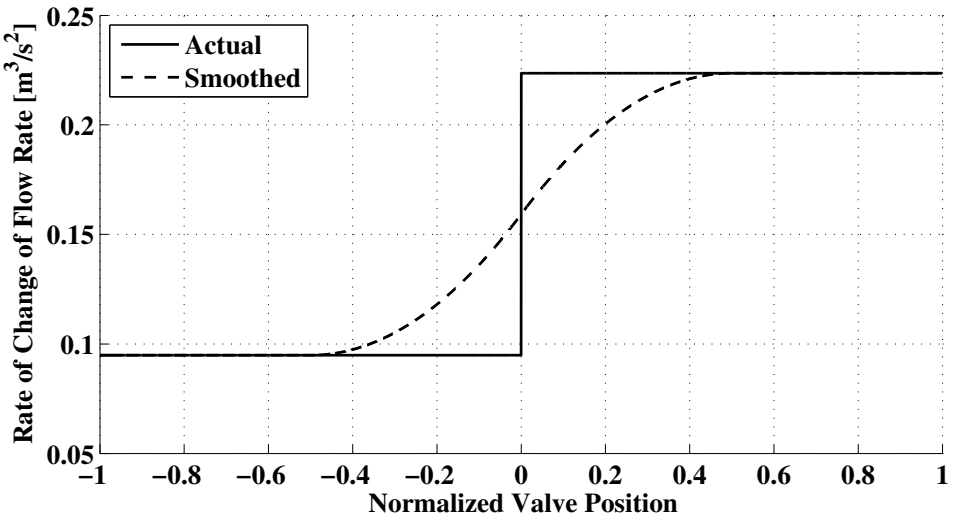

Fig. 2.8: Example of slope of flow rate with and without smoothing as a function of valve position.

more noticeable changes to Fig. 2.8 have large impacts on the convergence of the ODE solver used. It is also important to note that Fig. 2.7 is provided for illustration purposes only, and it is not a direct integration of Fig. 2.8.

This same method used above to smooth out Eq. (2.4). The sign(x) function is also discontinuous and may pose numerical problems for calculating friction and hysteresis in Eqs. (2.3) and (2.25). Figure 2.9 shows this function smoothed for a value of $\Delta x = 0.2$.

The value of Δx chosen for smoothing is very important. In general, choosing a large Δx increases the speed and computational efficiency of the ODE solver, but can generate significant model inaccuracies. It is important to choose the smallest Δx such that the ODE solver converges easily, and these artificial inaccuracies are minimized.

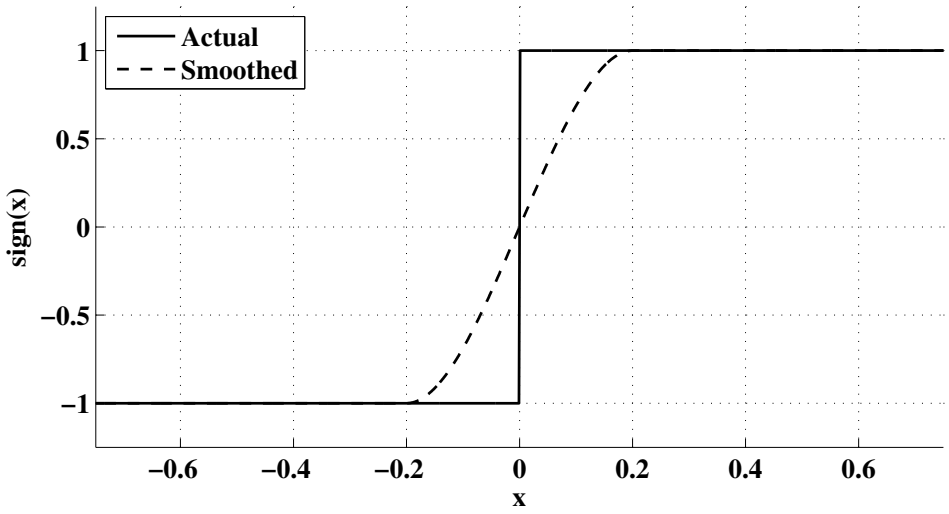

Fig. 2.9: Sign function with and without smoothing.

2.3.4 Constraining Actuator Motion

When modeling the actuator, special care has to be taken to assure the stroke of the actuator is contained within physical limits. To properly model actuator limits, a flag with five different operating values has been defined and integrated into the model. Note that when discussing forcing, positive forcing is defined as a net force in the positive x_p direction and negative forcing is defined as a net force in the negative x_p direction.

Flag = 0, Normal Operation: In this mode, the actuator is operating between its limits and the code checks to see if the actuator has reached minimum or maximum stroke by monitoring x_p

Flag = 1, Fully Extended and Positive Forcing: In this mode, shown in Fig. 2.11, the actuator is fully extended and the net force is trying to extend it further.

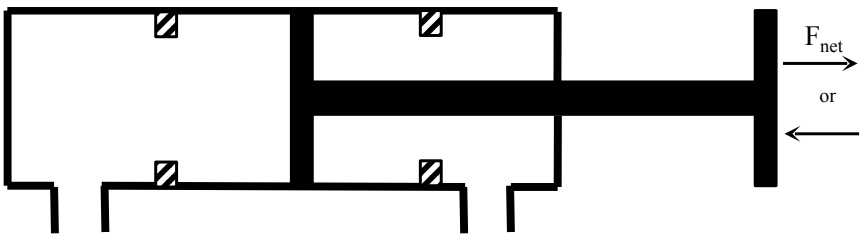

Fig. 2.10: Normal operation, Flag = 0.

The actuator position and velocity are held fixed with algebraic constraints since the actuator is fully extended and the net force is holding it in this position.

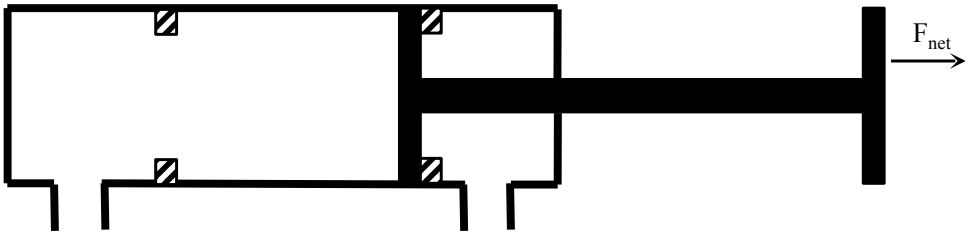

Fig. 2.11: Actuator fully extended and with positive forcing; Flag = 1.

Flag = 2, Fully Retracted and Negative Forcing: In this mode, shown in Fig. 2.12, the actuator is fully retracted and the net force is trying to retract it further. The actuator position and velocity fixed with algebraic constraints since the actuator is fully retracted and the net force is holding it in this position.

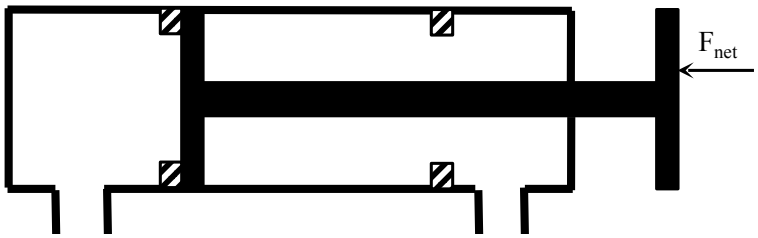

Fig. 2.12: Actuator fully retracted and with negative forcing; Flag = 2.

Flag = 3, Fully Extended and Negative Forcing: In this case, the actuator is fully extended but the net force is trying to retract it. Position and velocity initial conditions are set before resetting the differential equation solver. This mode is set when the actuator is previously in flag 1 and the net force changes negative, or when the actuator's momentum carries it into the fully extended stop despite negative acceleration.

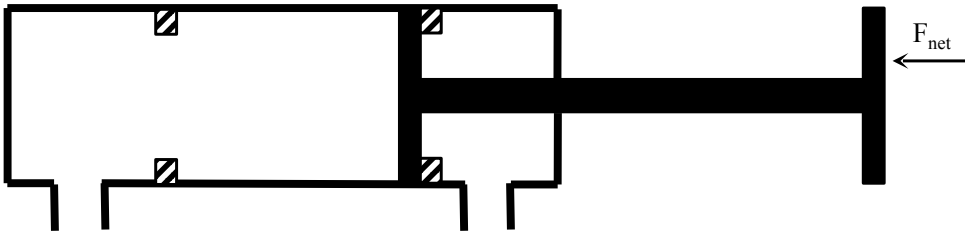

Fig. 2.13: Actuator fully extended and with negative forcing; Flag = 3.

Flag = 4, Fully Retracted and Positive Forcing: The actuator is fully retracted but the net force is trying to extend it. This mode sets position and velocity initial conditions before resetting the differential equation solver. This model is set when the actuator is previously in flag 2 and the net force changes positive, or when the actuator's momentum carries it into the fully retracted stop despite positive acceleration.

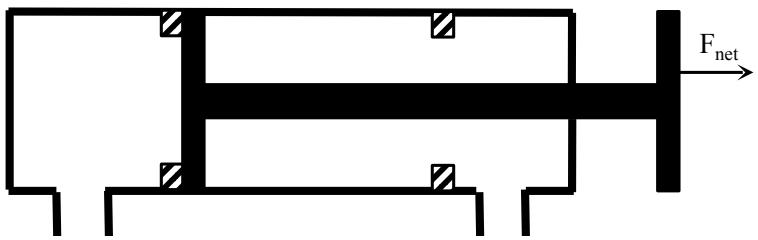

Fig. 2.14: Actuator fully retracted and with positive forcing; Flag = 4

The flow chart in Fig. 2.15 shows the logic followed by the ODE solver in dealing with actuator limits. Depending on the value of the actuator flag, the integration of the ODE solver is stopped, composition of the ODE system is changed, the system is reinitialized, and the integration is restarted (and continued until the next change of the value of the flag). The mode changes are implemented by taking advantage of a feature of the DAE solver DASKR used in the present study. In DASKR, it is possible to define "constraints equations" which are expressions that are monitored for zero crossings [21, 22]. When a constraint equation crosses zero, either from positive to negative, or negative to positive, the solver stops and the mode can be changed. Equations (2.55) through (2.60) describe the constraint equations used during each operational flag.

If Flag = 0,

$$R_1 = x_{1,max} - x_1 \tag{2.55}$$

$$R_2 = x_1 - x_{1,min} \tag{2.56}$$

If Flag = 1,

$$R_1 = F_{total} \tag{2.57}$$

If Flag = 2,

$$R_1 = F_{total} \tag{2.58}$$

If Flag = 3 or 4,

$$R_1 = F_{total} \tag{2.59}$$

$$R_2 = x_1 \tag{2.60}$$

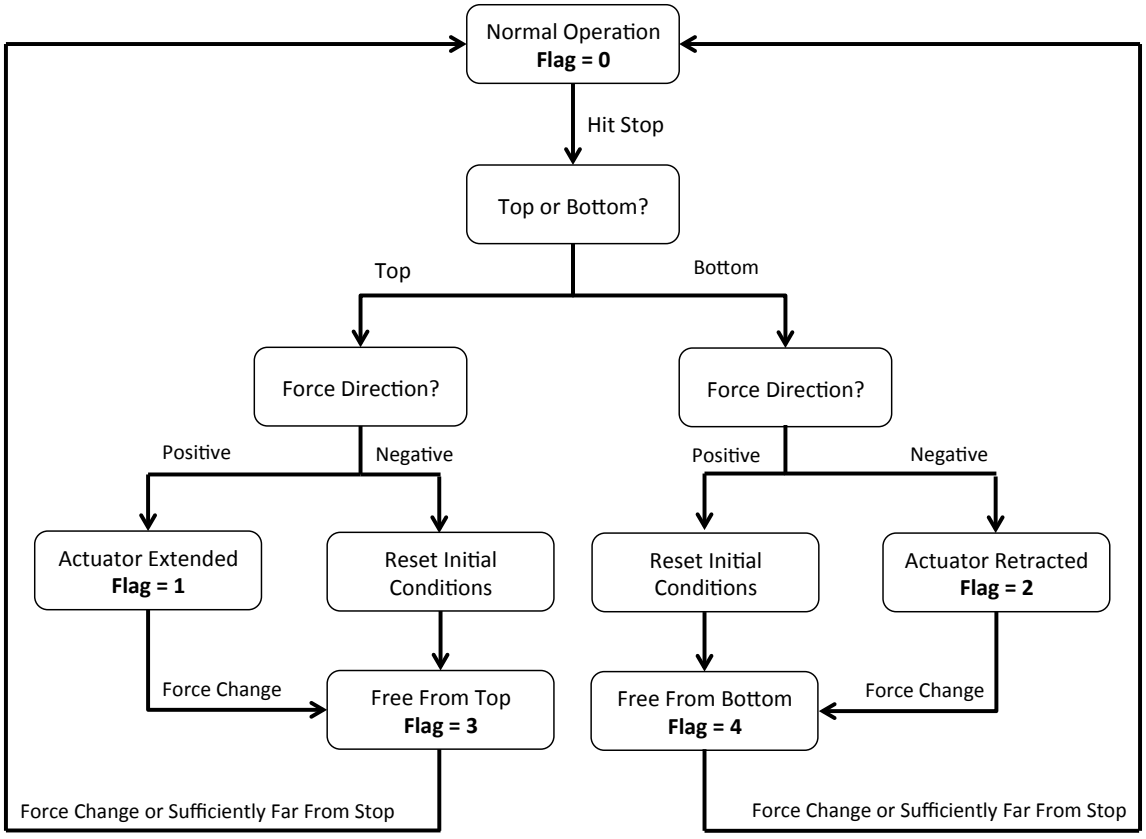

Fig. 2.15: Constraint logic flow chart.

In these equations, $x_{1,max}$ and x_{1_min} are the maximum and minimum piston displacements, respectively. The net force on the actuator, F_{total}, is equal to the right hand side of Eq. (2.2).

$$F_{total} = (P_A - \alpha P_B)A_p - F_f - F_{ext} \tag{2.61}$$

This is the same equation used to determine force direction when the actuator hits a stop.

If the force direction is in the same direction as the constraint, e.g., positive forcing against the upper constraint, the piston position and velocity are held con-

stant with algebraic equations instead of differential equations. The equations for these two situations are:

If Flag = 1

$$0 = x_1 - x_{1,max} \tag{2.62}$$

$$0 = x_2 \tag{2.63}$$

If Flag = 2

$$0 = x_1 - x_{1,min} \tag{2.64}$$

$$0 = x_2 \tag{2.65}$$

When the actuator is being forced while fully extended (Flag = 1) the algebraic equations, Eqs. (2.62) and (2.63) replace the ODEs, Eqs. (2.29) and (2.30), respectively. When the actuator is being forced while fully retracted (Flag = 2) the algebraic equations, Eqs. (2.64) and (2.65) replace the ODEs, Eqs. (2.29) and (2.30), respectively. It is important to note that these equations do not introduce any new physics, and simply force x_1 and x_2 to be constant. Meanwhile, all the pressure and valve dynamics are calculated as normal.

If the force direction is in the opposite direction as the constraint, e.g., negative forcing against the upper constraint, the piston position and velocity are set as initial conditions after a constraint equation has been triggered. For example, consider a heavy actuator extending quickly. Just before the actuator is fully extended, the net force becomes negative. With a net force opposite the direction of travel, the

actuator begins to decelerate but before it loses all its speed it reaches full extension. This example is one reason for having Flag = 3 and Flag = 4. When the actuator reaches this constraint, none of the differential equations change since the actuator is not being held into place by net force such as when Flag = 1 or Flag = 2. Rather, the actuator position and velocity are set as initial conditions and the differential equation solver is restarted.

If Flag = 3,

$$x_1 = x_{1,max} \tag{2.66}$$

$$x_2 = 0 \tag{2.67}$$

If Flag = 4,

$$x_1 = x_{1,min} \tag{2.68}$$

$$x_2 = 0 \tag{2.69}$$

Actuator limits were reconstructed from UH-60 limits described in References [1, 23]. To determine actuator travel limits, x_{max} for each actuator, the trimmed value was calculated and compared to the upper and lower limits provided in Ref. [1].

Upper and lower bounds δ_u and δ_l for swashplate lateral and longitudinal cyclic

Swashplate Angle	Trim Angle $[deg]$	Upper Limit $[deg]$	Lower Limit $[deg]$
Lateral Cyclic ($\theta_{1,c}$)	1.27	8.0	-8.0
Longitudinal Cyclic ($\theta_{1,s}$)	-1.74	16.3	-12.5

Table 2.2: Trimmed swashplate angles in hover compared to swashplate limits from Ref. [1]

were determined using

$$\delta_{\theta_{1,c},u} = \theta_{1,c,upper} - \theta_{1,c,trim} \tag{2.70}$$

$$\delta_{\theta_{1,c},l} = \theta_{1,c,trim} - \theta_{1,c,lower} \tag{2.71}$$

$$\delta_{\theta_{1,s},u} = \theta_{1,s,upper} - \theta_{1,s,trim} \tag{2.72}$$

$$\delta_{\theta_{1,s},l} = \theta_{1,s,trim} - \theta_{1,s,lower} \tag{2.73}$$

to calculate the distance in degrees from trimmed flight to the actuator limits. Table 2.3 shows the values of δ for lateral and longitudinal upper and lower limits.

Swashplate Angle	δ_{θ_u} $[deg]$	δ_{θ_l} $[deg]$
Lateral Cyclic ($\theta_{1,c}$)	6.73	9.27
Longitudinal Cyclic ($\theta_{1,s}$)	18.04	10.76

Table 2.3: Distance to swashplate limits for swashplate in trimmed hover

A representative $\delta = 12°$ was chosen for the upper and lower limits of each actuator, combining the effects of both cyclic and collective. An actuator under the effects of cyclic and collective must extend, or retract, for both control inputs. More information can be found in Section 2.4.3 where the conversion from actuator

displacement to swashplate angle is discussed. The physical limits of for actuator i are calculated using this representative δ using

$$x_{i,max} = x_{i,trim} + \kappa \left(\frac{\pi \delta}{180} \right) \tag{2.74}$$

$$x_{i,min} = x_{i,trim} - \kappa \left(\frac{\pi \delta}{180} \right) \tag{2.75}$$

where κ is the conversion factor between swashplate angle and actuator displacement, discussed in Section 2.4.3.

As a note, the present study is not trying to reproduce the specific actuator dynamics of the UH-60. However, representative data on the UH-60 swashplate limits is readily available and therefore it is used to create reasonable swashplate limits for this simulation.

2.3.5 Differential & Algebraic Equation Solver Optimization

The methods described in Section 2.3.4 which combine algebraic equations with differential equations, can increase computation time drastically, and may not be the most efficient. This is the case with the actuator dynamics, where computation times increased when the the algebraic equations were substituted for differential equations when the actuator was being forced against a stop.

In Section 2.3.4, when Flag = 1 or Flag = 2, (actuator fully extended or fully retracted, and fluid pressure holding it against the stop) the first two differential equations, Eqs. (2.29) and (2.30), were removed and replaced by algebraic equations, in order to hold the actuator position to fully extended or fully retracted, and velocity was set equal to zero. Instead of wasting unnecessary computation time

integrating the algebraic equations into the math, the original differential equations can be replaced by temporary, easy to solve differential equations, since the states corresponding to actuator position and actuator velocity are known.

In this situation, the algebraic equations presented in Eqs. (2.62) through (2.65) are replaced by the easily solvable, dummy, differential equations below.

If Flag = 1 or 2

$$0 = \dot{x}_1 - x_2 \tag{2.76}$$

$$0 = \dot{x}_2 - x_1 - x_2 \tag{2.77}$$

Ideally any easily solvable differential equation can be used. In addition, initial conditions for the states described in these dummy differential equations are reset to zero for a consistent, easily solvable set of equations.

If Flag = 1 or 2

$$x_1 = 0 \tag{2.78}$$

$$\dot{x}_1 = 0 \tag{2.79}$$

$$x_2 = 0 \tag{2.80}$$

$$\dot{x}_2 = 0 \tag{2.81}$$

Now that the necessary states have been reset to zero in order to solve an easy set of temporary differential equations, it is important to adjust any equations in our actuator model that rely on the states x_1, x_2, or their derivatives since these states are now all temporary. These necessary adjustments are described below.

Equation (2.35), which controls valve input must be adjusted depending on the actuator's flag by replacing the time dependent piston position x_1, with its constant maximum value, $x_{1,max}$, or minimum value, $x_{1,min}$ respectively:

If Flag = 1

$$u_1 = K_p(u_{1_d} - x_{1,max}) \tag{2.82}$$

If Flag = 2

$$u_1 = K_p(u_{1_d} - x_{1,min}) \tag{2.83}$$

Next, the Eqs. (2.9) and (2.10), used for calculating chamber volumes must be modified in a similar way (recall that $x_p \equiv x_1$).

If Flag = 1

$$V_A = V_{pl,A} + (x_{p,0} + x_{1,max})A_p \tag{2.84}$$

$$V_B = V_{pl,B} + (x_{p,0} - x_{1,max})\alpha A_p \tag{2.85}$$

If Flag = 2

$$V_A = V_{pl,A} + (x_{p,0} + x_{1,min})A_p \tag{2.86}$$

$$V_B = V_{pl,B} + (x_{p,0} - x_{1,min})\alpha A_p \tag{2.87}$$

Since the actuator is held at a constant position and velocity is zero, the friction force F_f, from Eq. (2.3), can be set to zero, i.e.

If Flag = 1 or 2

$$F_f = 0 \tag{2.88}$$

Finally, when saving the states from the differential equation solver at each time step, it is important to ignore the temporary states and save the known, actual states

If Flag = 1

$$x_1 = x_{1,max} \tag{2.89}$$

$$\dot{x}_1 = 0 \tag{2.90}$$

$$x_2 = 0 \tag{2.91}$$

$$\dot{x}_2 = 0 \tag{2.92}$$

If Flag = 2

$$x_1 = x_{1,min} \tag{2.93}$$

$$\dot{x}_1 = 0 \tag{2.94}$$

$$x_2 = 0 \tag{2.95}$$

$$\dot{x}_2 = 0 \tag{2.96}$$

When leaving Flag = 1 and Flag = 2, it is important to remember to reset the initial conditions for the states x_1 and x_2 as well as their derivatives before restarting the solver.

If leaving Flag = 1 and entering Flag = 3

$$x_1 = x_{1,max} \tag{2.97}$$

$$\dot{x}_1 = 0 \tag{2.98}$$

$$x_2 = 0 \tag{2.99}$$

$$\dot{x}_2 = 0 \tag{2.100}$$

If leaving Flag = 2 and entering Flag = 4

$$x_1 = x_{1,min} \tag{2.101}$$

$$\dot{x}_1 = 0 \tag{2.102}$$

$$x_2 = 0 \tag{2.103}$$

$$\dot{x}_2 = 0 \tag{2.104}$$

Replacing algebraic equations with "temporary" differential equations is a good way to avoid the additional computational time and effort associated with solving a DAE system. There is, however, another strategy that can reduce computational effort. Using the method above, when an actuator hits the stop, the ODEs Eqs. (2.31) through (2.34) are active, and continue to be integrated. In reality, the ODEs that describe actuator chamber pressures, Eqs. (2.31) and (2.32), give a constant pressure solution when the actuator is operating under Flag = 1 or Flag = 2.

When the actuator is forced up against a stop, it is unnecessary to calculate the pressure dynamics until the valve approaches the neutral position, preempting

a pressure change between each actuator chamber and the supply pressure and reservoir pressure as seen in Figs. 2.16 and 2.17.

Figure 2.18, shows some of the same quantities as Figs. 2.16 and 2.17, on an expanded time scale during the transition of valve position from positive to negative. The actuator chamber pressure and chamber flow rates do not move until the valve crosses the neutral position. In this case, the ODEs describing chamber pressures, Eqs. (2.31 and (2.32) can be replaced with algebraic equations similar to the method for actuator position and velocity used in Section 2.3.4. For improved efficiency, the ODEs describing chamber pressures can be replaced by temporary differential equations using the same method described previously in this section.

For the best increase in efficiency, and avoid any trouble with the inclusion of algebraic equations, the temporary differential equation method is used. When the actuator first enters operation under Flag = 1 or Flag = 2, the pressures $P_A = x_3$ and $P_B = x_4$ are held constant at supply and tank pressure, and Eqs. (2.31) and (2.32) are replaced by the temporary, dummy differential equations below.

If Flag = 1 or 2

$$0 = \dot{x}_3 - x_4 \tag{2.105}$$

$$0 = \dot{x}_4 - x_3 - x_4 \tag{2.106}$$

These equations have no physical meaning and are simply used to keep the number of differential equations constant while the differential equation solver integrates. Just like above, initial conditions for the states x_3 and x_4 are set to zero to ensure a consistent, easily solvable set of equations.

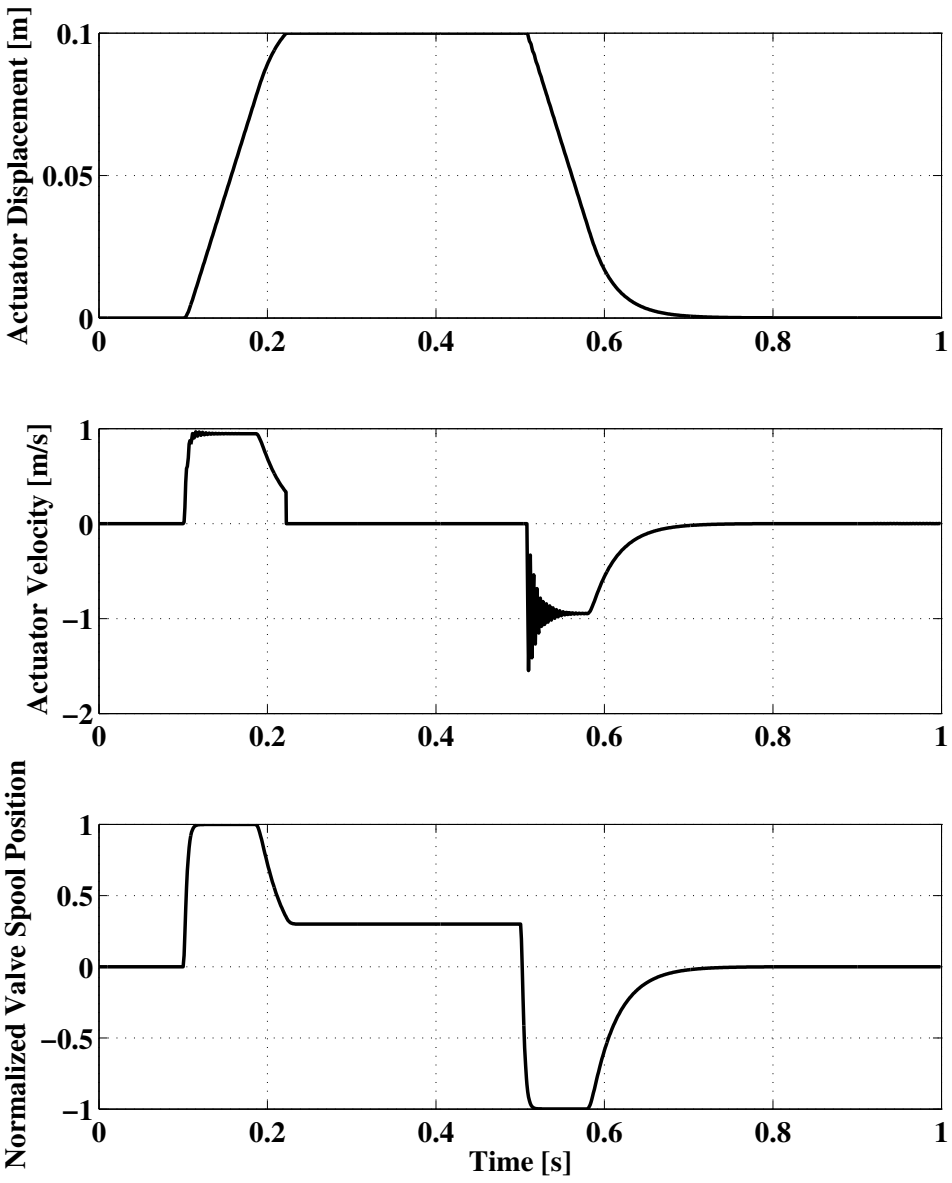

Fig. 2.16: Example plot of actuator position, velocity, and normalized valve spool when the upper position limit is reached.

If Flag = 1 or 2

$$x_3 = 0 \tag{2.107}$$

$$\dot{x}_3 = 0 \tag{2.108}$$

$$x_4 = 0 \tag{2.109}$$

$$\dot{x}_4 = 0 \tag{2.110}$$

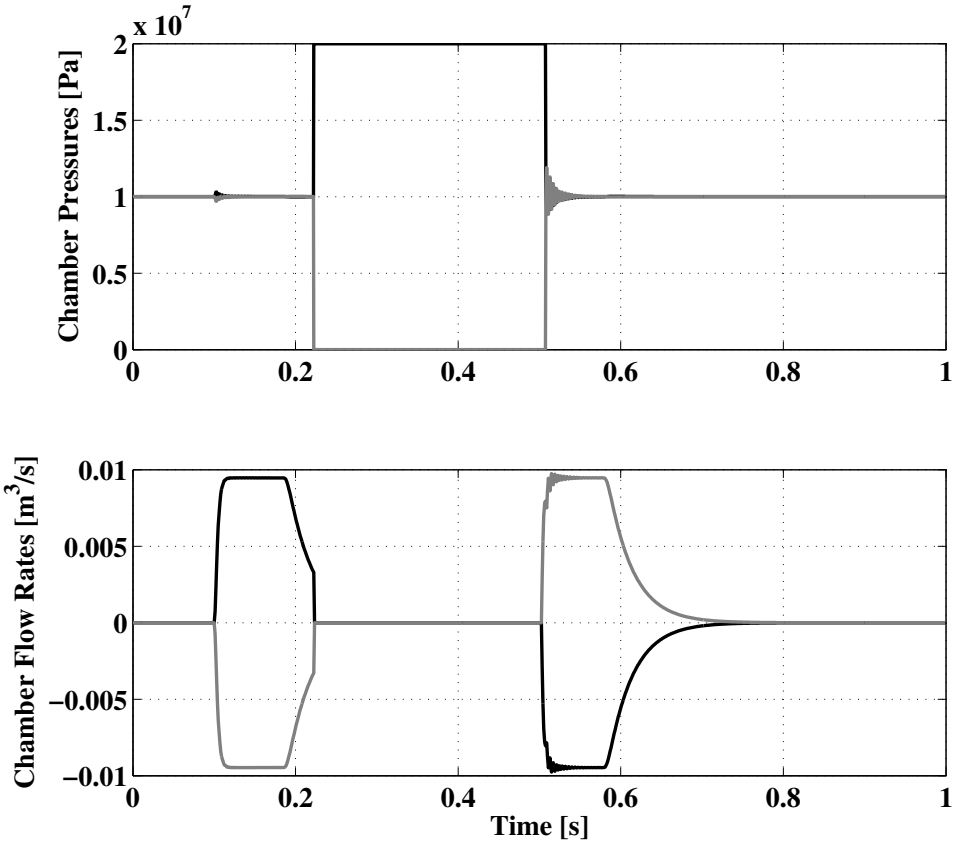

Fig. 2.17: Example plot of actuator chamber pressures and flow rates when the upper position limit is reached.

Since states x_3 and x_4 are now temporary and have no physical meaning, any equations that depend on actuator pressure dynamics must be modified. Equations (2.7) and (2.8) describing chamber flow rates, are modified by replacing

If Flag = 1

$$Q_A = 0 \tag{2.111}$$

$$Q_B = 0 \tag{2.112}$$

$$Q_{Li} = C_{Li}(P_T - P_s) \tag{2.113}$$

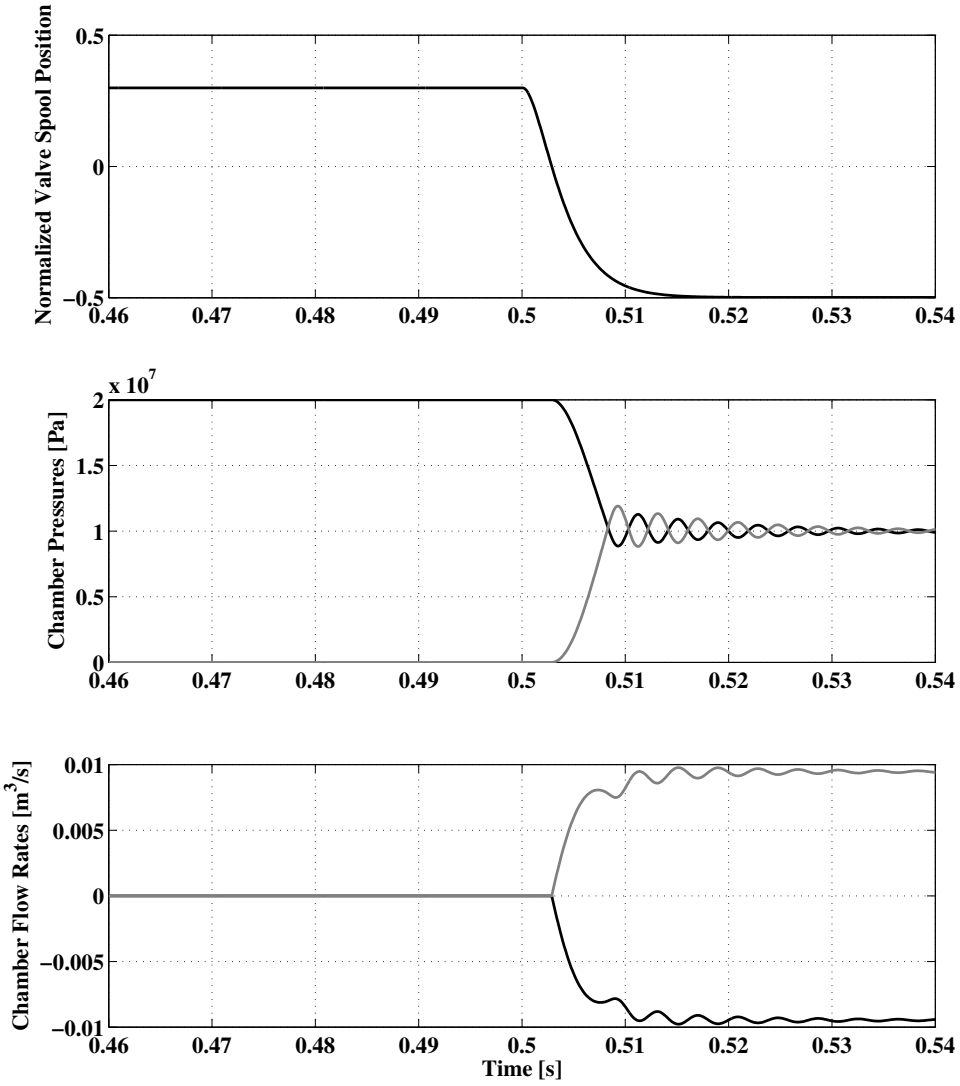

Fig. 2.18: Zoomed plot of normalized valve spool position and actuator chamber pressures and flow rates when the upper position limit is reached (same as in Figs. 2.16 and 2.17 but with an expanded time scale).

If Flag = 2

$$Q_A = 0 \tag{2.114}$$

$$Q_B = 0 \tag{2.115}$$

$$Q_{Li} = C_{Li}(P_s - P_T) \tag{2.116}$$

Additionally, the effective bulk moduli used in Eqs. (2.15) and (2.16) must be calculated using supply pressure, P_s, or tank pressure, P_T, depending on the actuator position.

If Flag = 1

$$C_{h,A} = \frac{V_A}{E'(P_s)} \tag{2.117}$$

$$C_{h,B} = \frac{V_B}{E'(P_T)} \tag{2.118}$$

If Flag = 2

$$C_{h,A} = \frac{V_A}{E'(P_T)} \tag{2.119}$$

$$C_{h,B} = \frac{V_B}{E'(P_s)} \tag{2.120}$$

While operating with the pressure dynamics off, it is important to ignore the values of the temporary states and save the values of the actual, known states

If Flag = 1

$$x_3 = P_s \tag{2.121}$$

$$\dot{x}_3 = 0 \tag{2.122}$$

$$x_4 = P_T \tag{2.123}$$

$$\dot{x}_4 = 0 \tag{2.124}$$

If Flag = 2

$$x_3 = P_T \tag{2.125}$$

$$\dot{x}_3 = 0 \tag{2.126}$$

$$x_4 = P_s \tag{2.127}$$

$$\dot{x}_4 = 0 \tag{2.128}$$

While the actuator is operating at constant pressure under Flag = 1 or Flag = 2, additional constraint equations can be added to tell the system when to reinstate full pressure dynamics. A pressure change is imminent when the valve spool nears the neutral position. Once the valve spool cross the neutral position, the supply and reservoir pressure lines connect to different chambers and the pressure dynamics resume an important role in determining actuator position, making it important to turn the pressure dynamic ODEs back on.

In addition to Eq. (2.57) when Flag = 1 and Eq. (2.58) when Flag = 2, the equations

If Flag = 1

$$R_2 = x_5 - 0.001 \tag{2.129}$$

If Flag = 2

$$R_2 = x_5 + 0.001 \tag{2.130}$$

are added to tell the ODE solver when to reactivate the pressure dynamics that were temporarily shut off. For example, if the actuator is in the fully extended position and the pressure dynamics are turned off, when the valve position, x_5, crosses 0.001,

the differential equation solver will stop the integration with the pressure dynamics ODEs removes, and restart it with those ODEs reinserted. The value of 0.001 was chosen to turn the pressure dynamics back on just before the valve spool crosses the neutral position. If the pressure dynamics are turned back on too early then efficiency is lost.

Similarly, if the actuator is in the fully retracted position and the pressure dynamics ODEs are removed, the solver will stop when the valve position crosses -0.001. This assures that the pressure dynamics are on and ready before the valve spool crosses the neutral position and pressure dynamics begin to react.

When reintroducing the pressure dynamics ODEs in the model, it is important to remove all the temporary state values used in the dummy ODEs, and replace those state with their actual value. If Flag = 1, the chamber A pressure, x_3, is set back to P_s and chamber B pressure, x_4, is set back to P_T. These values are dependent on which flag the actuator is operating under and will reverse if the Flag = 2 as seen below.

If Flag = 1

$$x_3 = P_s \tag{2.131}$$

$$\dot{x}_3 = 0 \tag{2.132}$$

$$x_4 = P_T \tag{2.133}$$

$$\dot{x}_4 = 0 \tag{2.134}$$

If Flag = 2

$$x_3 = P_T \tag{2.135}$$

$$\dot{x}_3 = 0 \tag{2.136}$$

$$x_4 = P_s \tag{2.137}$$

$$\dot{x}_4 = 0 \tag{2.138}$$

With these algorithmic modifications in place, calculation time is decreased substantially without sacrificing model accuracy.

2.3.6 Model Summary

Figure 2.19 shows an updated flow chart detailing the logic used during the time integration process.

The ODEs that make up the actuator model for each of the five operating conditions are summarized below:

If Flag = 0 or Flag = 3, or Flag = 4,

$$0 = \dot{x}_1 - x_2$$

$$0 = m_t\dot{x_2} - (x_3 - \alpha x_4)A_p + F_f(x_2) + F_{ext}$$

$$0 = V_A(x_1)\dot{x_3} - E'(x_3)[Q_A(x_3, x_5) - A_p x_2 + Q_{Li}(x_3, x_4)]$$

$$0 = V_B(x_1)\dot{x_4} - E'(x_4)[Q_B(x_4, x_5) + \alpha A_p x_2 - Q_{Li}(x_3, x_4)]$$

$$0 = \dot{x}_5 - x_6$$

$$0 = \dot{x}_6 - \omega_v^2 \left[u_1 - \frac{2D_v}{\omega_v}x_6 - x_5 - f_{hs}sign(x_5)\right]$$

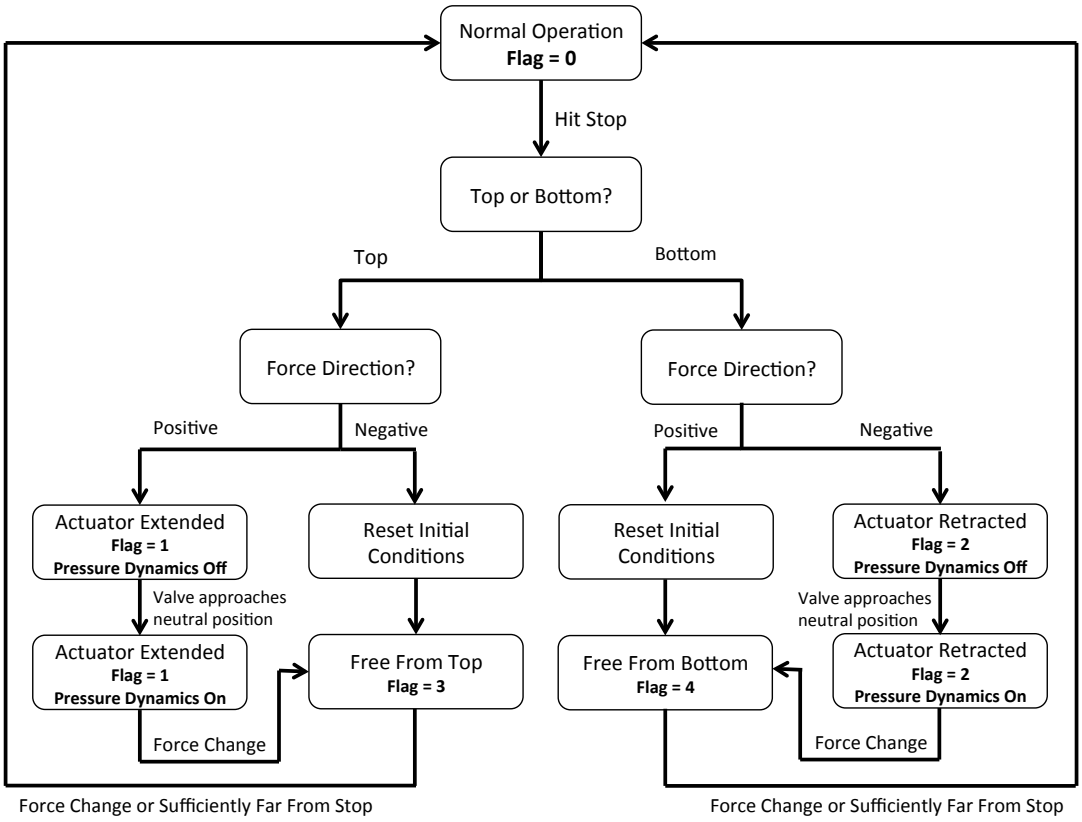

Fig. 2.19: Optimized constraint logic flow chart

If Flag = 1 or Flag = 2 and press dynamics on,

$$0 = \dot{x}_1 - x_2 \qquad \text{(dummy ODE)}$$

$$0 = \dot{x}_2 - x_1 - x_2 \qquad \text{(dummy ODE)}$$

$$0 = V_A(x_1)\dot{x_3} - E'(x_3)[Q_A(x_3, x_5) - A_p x_2 + Q_{Li}(x_3, x_4)]$$

$$0 = V_B(x_1)\dot{x_4} - E'(x_4)[Q_B(x_4, x_5) + \alpha A_p x_2 - Q_{Li}(x_3, x_4)]$$

$$0 = \dot{x}_5 - x_6$$

$$0 = \dot{x}_6 - \omega_{\mathrm{v}}^2 \left[u_1 - \frac{2D_v}{\omega_v} x_6 - x_5 - f_{hs} sign(x_5) \right]$$

If Flag = 1 or Flag = 2 and press dynamics off,

$$0 = \dot{x}_1 - x_2 \qquad \text{(dummy ODE)}$$

$$0 = \dot{x}_2 - x_1 - x_2 \qquad \text{(dummy ODE)}$$

$$0 = \dot{x}_3 - x_4 \qquad \text{(dummy ODE)}$$

$$0 = \dot{x}_4 - x_3 - x_4 \qquad \text{(dummy ODE)}$$

$$0 = \dot{x}_5 - x_6$$

$$0 = \dot{x}_6 - \omega_{\mathrm{v}}^2 \left[u_1 - \frac{2D_v}{\omega_v} x_6 - x_5 - f_{hs} sign(x_5) \right]$$

2.4 Simulation Model

2.4.1 Helicopter Model

The helicopter simulation model used in this study is composed of a coupled set of nonlinear ordinary differential equations [30]. Four rotor blades are modeled using beam finite elements and include coupled torsion and flap-lag bending degrees of freedom. A finite state Peters inflow model that permits both radial and higher harmonic azimuthal variations of the rotor inflow is used. Aerodynamic, structural, and inertial forces and moments are calculated at specific points internal to each finite element. A modal reduction is used to reduce the number of degrees of freedom. The aerodynamic and inertial blade pitching moment are used to calculate forces on each pitch link, which are then transferred to the swashplate supported by three independent actuator models.

There are many different assumptions made in the formulation of the mathe-

matical model under which HeliUM operates [30]. These assumptions include:

1. No sweep, droop, or torque offsets are included in the undeformed blade.
2. External wind velocity is zero.
3. The airframe is modeled as a rigid body with a constant mass and a uniform mass distribution; the x-z plane is a plane of symmetry.
4. Wind tunnel tests without the main rotor are used to derive fuselage and tail surface aerodynamics. Look-up tables are used to calculate aerodynamic coefficients as functions of angle of attack and sideslip. Stall, compressibility, and unsteady aerodynamic effects are neglected for the fuselage and tail.
5. Inboard of the flap and lag hinges, the blade is assumed rigid in flap, lag, and torsion.
6. Flap, lag, and pitch hinges are coincident
7. Blade cross sections are symmetric with respect to the major principal axes
8. Blade center of gravity, aerodynamic center, and elastic axis are not necessarily coincident.
9. Blade chord, twist, stiffness and mass properties, and cross-sectional offsets are defined at discrete spanwise locations and vary linearly in between.
10. An isotropic, linearly elastic material is used to model the blade.

11. Blade cross-section remains perpendicular to the elastic axis during deformations (Bernoulli-Euler beam theory). The effects of shear deformation are neglected.

12. The blade undergoes moderate deflections implying small strains and finite rotations.

13. Aerodynamic forces and moments on the blade section are based on the airflow velocity at the elastic axis of the blade.

14. All blades are assumed uniform.

15. Blades rotate at a constant angular speed, Ω. Engine and engine control systems are neglected.

16. Tail rotor collective control is attached rigidly to the pilot controls.

HeliUM models the main rotor blades individually in the rotating frame. This allows for superior flexibility when modeling individual blades, including analysis of rotor systems with dissimilar blades. For the purposes of this study, the main rotor blades are assumed symmetric.

The main rotor blades are modeled as flexible beams undergoing coupled flap, lag, torsion and axial motion. The nonlinear, coupled, partial differential equations with period coefficients are transformed into a system of nonlinear, coupled, ordinary differential equations using finite element discretization based on Galerkin's method of weighted residuals. A total of 15 nodal degrees of freedom are tracked per blade. These include flap and lag bending displacements and slopes at the ends of the

element, for 8 total degrees of freedom, torsional rotations at the ends and mid-point of each element, and axial displacements at four equally spaced nodes between the end points of the element. To reduce the number of degrees of freedom, a modal coordinate transformation is used. This has the effect of reducing the number of equations required to describe the dynamics of each rotor blade. Coupled, rotating blade mode shapes are used resulting in a system of nonlinear, coupled, second order ordinary differential equations with time-varying coefficients.

For the simulation, HeliUM was configured to represent a mid-size utility helicopter with a single, four-bladed main rotor. Rotorcraft model and environment parameters are listed in Table 2.4.

Parameter	Value
Altitude	3777 $[ft]$
Ambient Pressure	14.696 $[psi]$
Ambient Temp.	58.44 $[F]$
Helicopter Weight	15324 $[lbs]$
I_{xx}	4659.00 $[Slugs - ft^2]$
I_{xy}	1882.00 $[Slugs - ft^2]$
I_{yy}	38512.00 $[Slugs - ft^2]$
I_{zz}	36796.00 $[Slugs - ft^2]$

Table 2.4: HeliUM model and environment parameters used for actuator study

2.4.2 Coupling of Actuator Model and Helicopter Model

The ODEs that make up the actuator model have been summarized in Section 2.3.6. The key is to use program the current simulation stick inputs as reference swashplate angle inputs to the actuator model and use the actual actuator positions to calculate the actual swashplate angle. A typical time step calculation in HeliUM during a time integration routine works in the following steps:

1. Calculate swashplate angles based on stick inputs
2. Calculate rotorcraft ODE residuals
3. Iterate state approximations and repeat until convergence on solution for a given time step
4. Repeat until final time is reached

When implementing actuator dynamics, the swashplate angles calculated based on stick inputs are passed to the actuator model where they are decomposed into individual actuator reference inputs. These actuator reference inputs are desired actuator displacements to achieve the reference swashplate angle. With reference displacements, the actuator valve inputs are calculated and used to calculate actuator residuals. Next, the actual actuator displacements are converted to swashplate angles and sent back into HeliUM where they are used for the rest of the residual calculations. The steps are outlined below with new steps in bold.

1. Calculate swashplate angles based on stick inputs (these will be used as reference inputs to the actuator model)

2. Calculate actual swashplate angles based on actual actuator states

3. Calculate helicopter residuals (now including actuator residuals)

4. Iterate state approximations and repeat until convergence on solution for a given time step

5. Repeat until final time is reached

Because HeliUM is designed around implicit differential equations and the calculation of residuals, it is simple to add the 18 equations used to describe the dynamics of three actuators used to calculate swashplate angle. By simply rerouting the pilot's input to the actuator inputs, and rerouting the actuator displacements to swashplate angles, the hydraulic system can be easily modeled without major changes to the rotorcraft simulation.

2.4.3 Trim

Trimming in HeliUM is a process designed to achieve period blade response such that the helicopter maintains equilibrium in space. Helium calculates the forces and moments generated by the rotor which should be equal and opposite to those generated by other parts of the helicopter. This is the first step and is required before beginning either linearization or time integration. Before performing any other analysis, it is important to make sure the rotorcraft has successfully trimmed.

The coupling of the actuators with the rest of the helicopter model is based on the assumption that the actuator affects the blades dynamics by changing their

root pitch angle through the swashplate. Conversely, the blades affect the actuator dynamics by changing the force acting on the actuators. These forces are transmitted by the pitch links to the swashplate, and from here to the actuators.

When adding the actuator dynamics to the trim process, trim unknowns, which can be thought of as the simulation's initial conditions, all states, including the new actuator states. To simplify this conversion, the actuators states are assumed fixed through the entire revolution of the rotor when trimmed. Using this assumption, we know $\dot{x}_p = 0$ and $\ddot{x}_p = 0$, that is, the actuators have zero velocity and acceleration. If the actuators are stationary, we know the valve must be closed and not moving. This means $x_{\mathrm{v}}^* = \dot{x}_{\mathrm{v}}^* = 0$. Additionally, the pressures in each chamber of the actuator are constant, that is, $\dot{P}_A = \dot{P}_B = 0$.

State	Actuator 1	Actuator 2	Actuator 3
x_p	x_1	x_7	x_{13}
$\dot{x}_p$	x_2	x_8	x_{14}
P_A	x_3	x_9	x_{15}
P_B	x_4	x_{10}	x_{16}
x_{v}^*	x_5	x_{11}	x_{17}
$\dot{x}_{\mathrm{v}}^*$	x_6	x_{12}	x_{18}
$\dot{u}_{\mathrm{v}}^*$	u_1	u_2	u_3

Table 2.5: States and inputs for the three swashplate actuators

The only nonzero states that need to be recalculated at trim are the actuator position $x_p = x_1$ and actuator chamber pressures $P_A = x_3$ and $P_B = x_4$.

When trimmed, the actuators will extend such that the desired swashplate angle is achieved. The required extension will depend on where each actuator is located. In the present study, actuators 1, 2, and 3, are located at $\psi = 0$, $\psi = 90$, and $\psi = 270$ degrees, respectively, as shown schematically in Fig. 2.20.

To achieve a positive roll response (right side down) for a positive lateral cyclic stick input, the swashplate must tilt right. To tilt the swashplate to the right, actuator 2, located at $\psi = 90$, must be lowered, and actuator 3, located at $\psi = 270$, must be raised using

$$x_7 = -\kappa_{7,s}\theta_{1s} \tag{2.139}$$

$$x_{13} = \kappa_{13,s}\theta_{1s}. \tag{2.140}$$

In the equation above, $\kappa_{7,s}$ and $\kappa_{13,s}$ are conversion factors between swashplate angle and actuator displacement. Specifically, it converts lateral cyclic to actuator 2 and 3 displacement respectively. This is largely depended on the geometry of the pitch link and is discussed in more detail below.

To tilt the tip path plane aft in the presence of positive longitudinal cyclic, actuator 1 must be lowered using

$$x_1 = -\kappa_{1,c}\theta_{1c}. \tag{2.141}$$

Collective, θ_{col}, increases each blade's pitch an equal amount and is not dependent on the blade's azimuth. As such, applying positive collective requires each actuator to rise an equal amount.

$$x_1 = \kappa_{1,col}\theta_{col} \tag{2.142}$$

$$x_7 = \kappa_{7,col}\theta_{col} \tag{2.143}$$

$$x_{13} = \kappa_{13,col}\theta_{col} \tag{2.144}$$

Typically during flight, the pilot is required to apply more than one input at a time. During the simulation, in the presence of more than one input, the required actuator displacements are added together. The final equations for actuator displacement are

$$x_1 = \kappa_{1,col}\theta_{col} - \kappa_{1,c}\theta_{1c} \tag{2.145}$$

$$x_7 = \kappa_{7,col}\theta_{col} + \kappa_{7,s}\theta_{1s} \tag{2.146}$$

$$x_{13} = \kappa_{13,col}\theta_{col} - \kappa_{13,s}\theta_{1s}. \tag{2.147}$$

The swashplate angle to actuator displacement conversion factor, κ, is used to dictate how much the actuator must move for a unit displacement in swashplate angle. In this report, all factors κ are equal but they can each be adjusted independently. Currently swashplate angles are calculated in radians and actuator displacements are calculated in meters so the units for κ are $^{m}/_{rad}$.

Now that trimmed actuator displacements x_1, x_7, and x_{13} are calculated, pressure states x_3, x_4, x_9, x_{10}, x_{15} and x_{16} must be calculated. These states are byproducts of the actuator's position as well as external forces so they are calculated after the trim process rather than during the trim process.

Part of the trim process in HeliUM involves calculating blade aerodynamic forces and moments as well as inertial forces and moments. The external forces used for calculating chamber pressures for each actuator are associated with the aerodynamic and inertial blade pitching moments, which result in a net force on the pitch link via the pitch horn, and are is then summed at the swashplate.

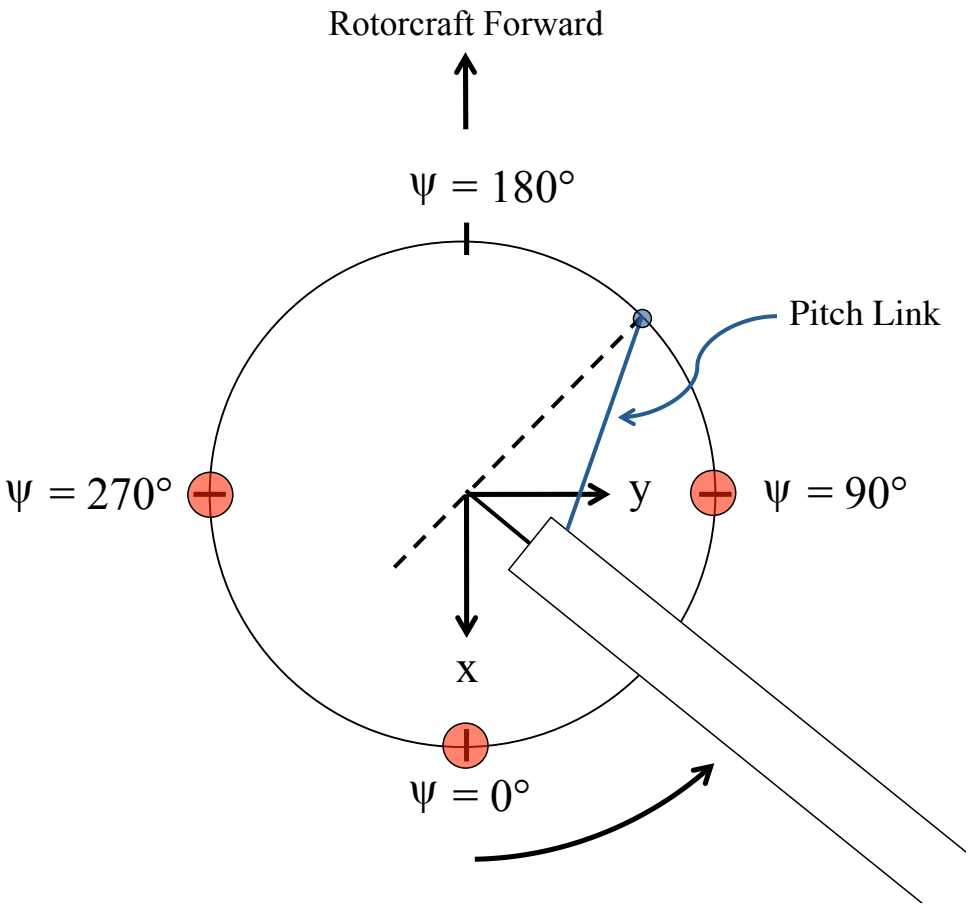

Fig. 2.20: Rotorcraft swashplate angles and axes

To calculate the net force on the swashplate, the aerodynamic and inertial pitching moments of each blade and are summed together.

$$M_i = M_{i_{x,aero}} + M_{i_{x,inertial}} \tag{2.148}$$

where $M_{i_{x,aero}}$ and $M_{i_{x,inertial}}$ are the blade aerodynamic and inertial pitching moment respectively. The total moment is then divided by the pitch horn length, l_{ph}, to yield the total force on pitch link i

$$F_i = \frac{M_i}{l_{ph}}. \tag{2.149}$$

With the total force on each pitch link, force and moment equilibrium can be enforced using

$$\sum F_z = 0 \tag{2.150}$$

$$\sum M_x = 0 \tag{2.151}$$

$$\sum M_y = 0. \tag{2.152}$$

$$\tag{2.153}$$

The unknown actuator forces, $F_{act,k}$, can be summed with the known pitch link forces using

$$0 = \sum_{k=1}^{n_a} F_{act,k} + \sum_{i=1}^{n_b} F_i \tag{2.154}$$

which can be expanded to form

$$0 = F_{act,1} + F_{act,2} + F_{act,3} + F_1 + F_2 + F_3 + F_4 \tag{2.155}$$

for a simulation with three actuators and four blades.

For the moment equilibrium, consider the rotorcraft shaft x and y axis. The x axis extends along the longitudinal direction of the rotorcraft with positive x pointing in the $\psi = 0°$ direction. The y axis extends along the lateral direction of the rotorcraft with positive y pointing in the $\psi = 90°$

First, the two-dimensional moment along the x axis generated by blade i at azimuthal position ψ can be described by

$$M_{x,i}(\psi) = -r_{sp} \sin(\psi) F_i \tag{2.156}$$

where r_{sp} is the swashplate radius from the shaft to the pitch link. A blade $\psi = 0°$ or $\psi = 180°$, exerts no moment about the x axis. A force in the downward direction at $\psi = 90°$ creates a negative moment about the x axis and a force in the downward direction at $\psi = 270°$ creates a positive moment about the x axis as described by Eq. (2.156).

The actuators supporting these forces generated by the blade moments are calculated the same as Eq. (2.156) however the sign of the equation is reversed since the actuators are applying force in the opposite direction. Moments due to the actuators are calculated using

$$M_{x,act_2} = r_{act} \sin(90°) F_2 = r_{act} F_{act,2} \tag{2.157}$$

$$M_{x,act_3} = r_{act} \sin(270°) F_3 = -r_{act} F_{act,3} \tag{2.158}$$

where r_{act} is the radius from the shaft axis to the actuator The final moment equation about the x axis is

$$r_{act} F_{act,2} - r_{act} F_{act,3} + \sum_{i=1}^{n_b} -r_{sp} sin(\psi) F_i. \tag{2.159}$$

The equation for moment equilibrium about the y axis can be derived the same way resulting in

$$-r_{act}F_{act,1} + \sum_{i=1}^{n_b} r_{sp}cos(\psi)F_i. \tag{2.160}$$

Equations (2.155), (2.159), and (2.160) can be simultaneously solved to derive the actuator forces $F_{act,1}$, $F_{act,2}$, and $F_{act,3}$.

In a trimmed actuator with no external forces present, the chamber pressures will be equal. This equalized pressure, P_{eq} is the average between supply pressure, P_s, and tank pressure, P_T.

$$P_{eq} = \frac{P_s + P_T}{2} \tag{2.161}$$

The equalized pressure can be thought of as an equilibrium and external forcing on actuator k creates a pressure differential between chambers A and B. If $F_{act,k}$ is positive, the pressure in chamber A will increase. The force $F_{act,k}$ must be divided by chamber A area A_A and added to the equalized pressure for chamber A. If $F_{act,k}$ is negative, the pressure in chamber B will increase. The force $F_{act,k}$ must be divided by chamber B area A_B and added to the equalized pressure for chamber B. The

trimmed actuator pressures for each actuator can be calculated using

$$x_3 = P_{eq} + \frac{F_{act,1}}{A_A} \tag{2.162}$$

$$x_4 = P_{eq} - \frac{F_{act,1}}{A_B} \tag{2.163}$$

$$x_9 = P_{eq} + \frac{F_{act,2}}{A_A} \tag{2.164}$$

$$x_{10} = P_{eq} - \frac{F_{act,2}}{A_B} \tag{2.165}$$

$$x_{15} = P_{eq} + \frac{F_{act,3}}{A_A} \tag{2.166}$$

$$x_{16} = P_{eq} - \frac{F_{act,3}}{A_B} \tag{2.167}$$

Which can be simplified to

$$x_3 = P_{eq} + \frac{F_{act,1}}{A_p} \tag{2.168}$$

$$x_4 = P_{eq} - \frac{F_{act,1}}{\alpha A_p} \tag{2.169}$$

$$x_9 = P_{eq} + \frac{F_{act,2}}{A_p} \tag{2.170}$$

$$x_{10} = P_{eq} - \frac{F_{act,2}}{\alpha A_p} \tag{2.171}$$

$$x_{15} = P_{eq} + \frac{F_{act,3}}{A_p} \tag{2.172}$$

$$x_{16} = P_{eq} - \frac{F_{act,3}}{\alpha A_p} \tag{2.173}$$

using α, the ratio of internal cross-section areas.

The derivation for the blade aerodynamic and inertial moments in HeliUM is described in detail in Reference [30]. A brief overview is included here for convenience.

Two-dimensional quasi-stead aerodynamics [31] is used for aerodynamic blade section force and moment calculations. Blade lift, L, and pitching moment, M, is

described by

$$L = L_Q + \frac{1}{2} a \rho (bR)^2 V_0 \dot{\alpha} \tag{2.174}$$

$$M = L_Q x_A - \frac{1}{2} a \rho V_0 \dot{\alpha} (bR - x_A)(bR)^2 \tag{2.175}$$

where lift-curve slope a, a function of the angle of attack and mach number, is obtained from look-up tables, ρ is the air density, b is the non-dimensional semi-chord length, R is the blade radius, α is the total pitch angle of the blade section, V_0 is the freestream velocity as seen by the blade element, x_A is the blade cross-sectional aerodynamic center offset from the elastic axis, and $\dot{\alpha}$ is the rate of change of the total blade pitch angle. Acceleration terms $\ddot{h}$ and $\ddot{\alpha}$ are neglected for simplification.

Freestream velocity V_0 and L_Q, the quasi-steady lift, can be calculated using

$$V_0 = \sqrt{U_{\mathrm{P}}^2 + U_{\mathrm{T}}^2 + U_{\mathrm{R}}^2} \tag{2.176}$$

$$L_Q = \frac{1}{2} \rho V_0^2 c \left[C_L + \frac{a \dot{\alpha}}{V_0} \left(\frac{c}{2} - x_A \right) \right] \tag{2.177}$$

where c is the local blade chord.

Chord c can be substituted for the semi-chord b in Equation 2.174 giving

$$L = L_Q + \frac{1}{8} a \rho_A V_0 c^2 \dot{\alpha} \tag{2.178}$$

The aerodynamic drag can be calculated using

$$D = C_D \frac{1}{2} \rho_A V_0^2 c \tag{2.179}$$

where C_D is the steady drag coefficient determined from look-up tables.

Now that the section lift and drag have been calculated, they must be trans-

formed to the local blade sectional aerodynamics coordinate system.

$$f_p = \frac{1}{V_0}\left[L\frac{U_T}{cos(\gamma_I)} + DU_p\right] \tag{2.180}$$

$$f_t = \frac{1}{V_0}\left[DU_T - LU_P cos(\gamma_I)\right] \tag{2.181}$$

$$f_R = \frac{1}{V_0}\left[DU_R - L\frac{U_P cos(\gamma_I)U_R}{U_T}\right] \tag{2.182}$$

The aerodynamic force component f_p points along the e_p axis, f_T points along the e_R axis, and f_R along the e_P axis. The e_T axis points aft, in the blade lag direction, e_p points outboard, along the tangent to the elastic axis, and e_R is normal to the $e_T - e_P$ plane and is defined as positive up.

The total pitching moment can be described as the sum of three terms

$$M = M_S + M_Q + M_{\dot{\alpha}} \tag{2.183}$$

where M_S is the result of the pitching moment coefficient C_M, M_Q is the component from Equation 2.175 resulting from the quasi-steady lift, and $M_{\dot{\alpha}}$ is the component from Equation 2.175 representing the non-circulatory pitch damping contribution. The components can be calculated as follows:

$$M_S = \frac{1}{2}C_M \rho V_0^2 c^2 \tag{2.184}$$

$$M_Q = f_p\frac{L_q}{L}x_A cos(\theta_G) + f_T\frac{L_Q}{L}x_A sin(\theta_G) \tag{2.185}$$

$$M_{\dot{\alpha}} = -\frac{1}{8}a\rho V_0 c^2 \dot{\alpha}\left(\frac{c}{2} - x_A\right) \tag{2.186}$$

where θ_G is the geometric pitch angle of the blade and the ratio $\frac{L_Q}{L}$ is required to scale the force components f_p and f_T which contain total lift and not just the quasi-steady lift component required.

Now the distributed aerodynamic loads are transformed into the undeformed preconed blade coordinate system for use in the swashplate equations above. The distributed aerodynamic moments are

$$q_A = -Mcos\zeta cos\beta \hat{e}_x - Msin\zeta cos\beta \hat{e}_y - Msin\beta \hat{e}_z \tag{2.187}$$

$$= q_{Ax}\hat{e}_x + q_{Ay}\hat{e}_y + q_{Az}\hat{e}_z \tag{2.188}$$

where

$$M_{i_{x,aero}} = q_{Ax} \tag{2.189}$$

for use in Equation 2.148.

Calculation of the distributed inertia moment acting on the blade are given by the equation

$$q_I = -\int_A \rho \left[(y_0 \hat{e}_x^{'} + z_0 \hat{e}_y^{'}) \times (a_P + gk_I) \right] dA \tag{2.190}$$

$$= q_{Ix}\hat{e}_x + q_{Iy}\hat{e}_y + q_{Iz}\hat{e}_z \tag{2.191}$$

where ρ is the density of the blade, y_0 and z_0 are the coordinates of the mass point on the blade cross section A, and gk_I is the contribution due to gravity. For equation 2.148, it can be shown that

$$M_{i_{x,inertial}} = q_{Ix}. \tag{2.192}$$

For more information on the derivation of q_{Ix} please refer to Reference [30].

Chapter 3

Analysis of Actuator Dynamics

3.1 Overview

With the hydraulic model in place, detailed analysis of the effects of hydraulic parameters on actuator performance can be examined. The analysis is based on the actuator equations of motions described in Eqs. (2.29) through (2.34), from which a time history of the actuator response to an arbitrary input over time can be calculated. The key parameters used in the simulation are those listed in Table 3.1 unless otherwise noted. For the results of this section, the actuator is given a step input corresponding to 1° of swashplate displacement. The swashplate is initially trimmed at zero degrees displacement and the actuator displacement is trimmed at zero piston displacement from its reference position. At $t = 0$ seconds, the simulation begins and remains in a trimmed state until $t = 0.1$ seconds when the hydraulic system is given an input corresponding to one degree of positive collective. During this simulation the swashplate is assumed to have zero mass. The states and key parameters of actuator 1 are recorded during the integration and compiled in the results below.

It should be noted that since collective pitch is being applied, all three actuators will exhibit the exact same behavior and only the time history of one actuator needs to be represented. In other simulations, such as the entire helicopter dynam-

ics model coupled with the actuator model, the actuators will each receive unique inputs based on the trim condition and prescribed inputs.

Parameter	Value
P_s	200 $[bar]$
P_t	0 $[bar]$
C_v	3.0x10^{-6}
C_{li}	0
$V_{pl_{A,B}}$	0.01 $[m^3]$
A_p	0.01 $[m^2]$
α	1
M_p	6.6 $[kg]$
ρ	890 $[\frac{kg}{m^3}]$

Table 3.1: Actuator configuration for study of supply pressure changes

3.2 Results

The step input was applied to the swashplate as 1° reference collective. This input is then converted to reference actuator positions through Eqs. (2.145) through (2.147). These reference actuator displacements are used to solve for reference valve spool inputs, u_{i}^*, for actuator i, via Eq. (2.35) where u_{i_d} is the desired piston position of actuator i.

3.2.1 Supply Pressure

The first set of actuator results involves changing the supply pressure, P_s supplied by the pump. Table 3.2 shows the range of pressures used in the study. Figure 3.1 shows the swashplate step response, actuator velocity, and flow rates for the five lowest supply pressures of the table. As supply pressure increases, the influence of supply pressure on the step response decreases. The largest influence of supply pressure is evident when comparing the two smallest supply pressures $P_s = 1$ $[bar]$ and $P_s = 5$ $[bar]$. This small change in supply pressure decreases the settling time significantly. The peak velocity of the actuator essentially doubles from this small change.

Category	Supply Pressure [bar]
Low pressure	1, 5, 15, 30, 50
High pressure	75. 125, 200, 300

Table 3.2: Supply pressures, P_s, used in study

The chamber flow rates shown are for chambers A and B. As supply pressure increases, the chamber A flow rate curve color changes from green to red. The chamber B flow rate curve changes from green to blue. Chamber B flow rate is negative indicating flow is traveling out of the chamber.

Figure 3.2 shows the step response for actuators at much higher pressures. Unlike Fig. 3.1, the step response of the actuator-swashplate system does not change significantly with large changes in supply pressure.

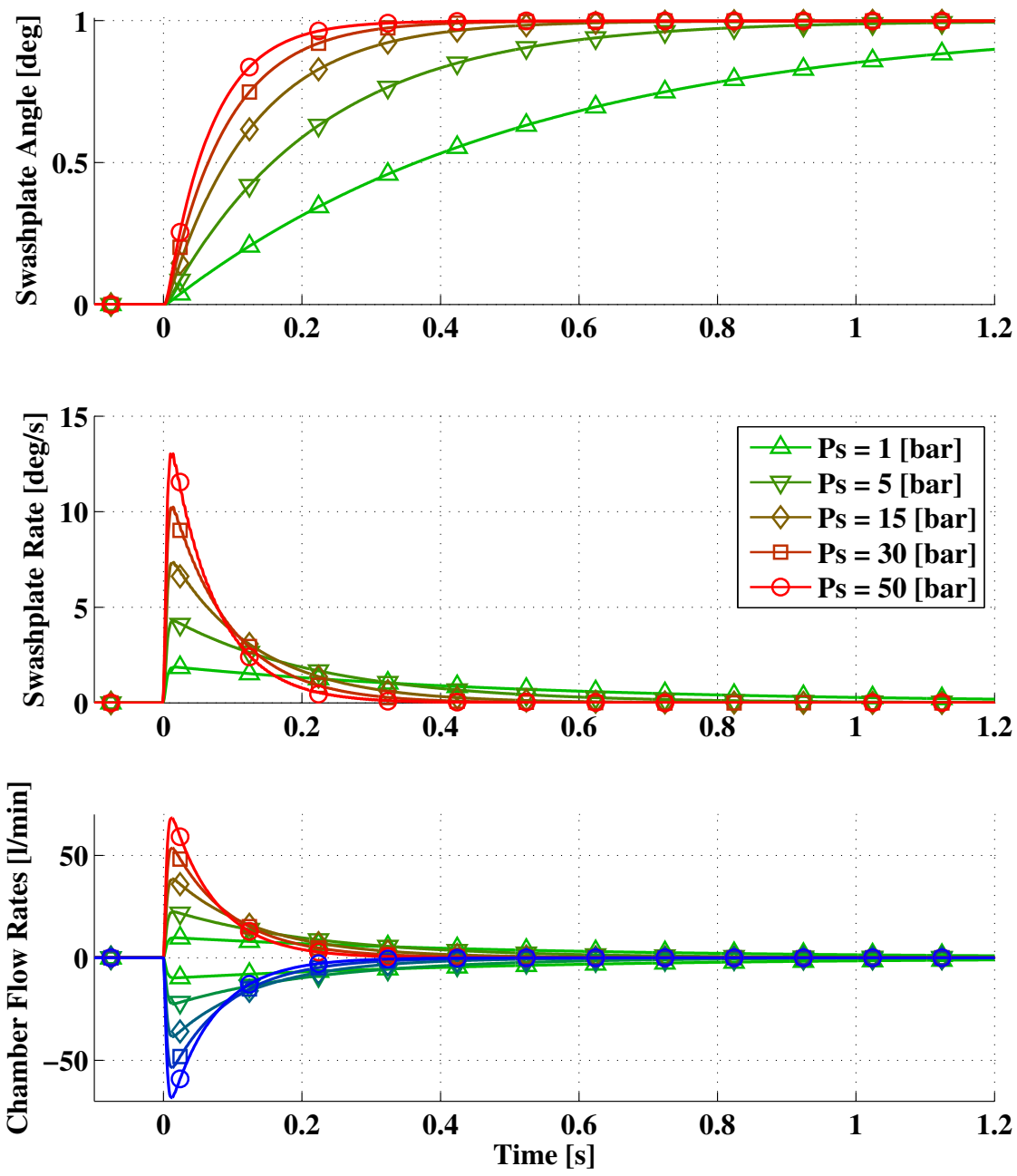

Fig. 3.1: Swashplate step response for unit degree step input at low supply pressures

Supply pressure's main influence is on the equations for flow rate, Eqs. (2.22)

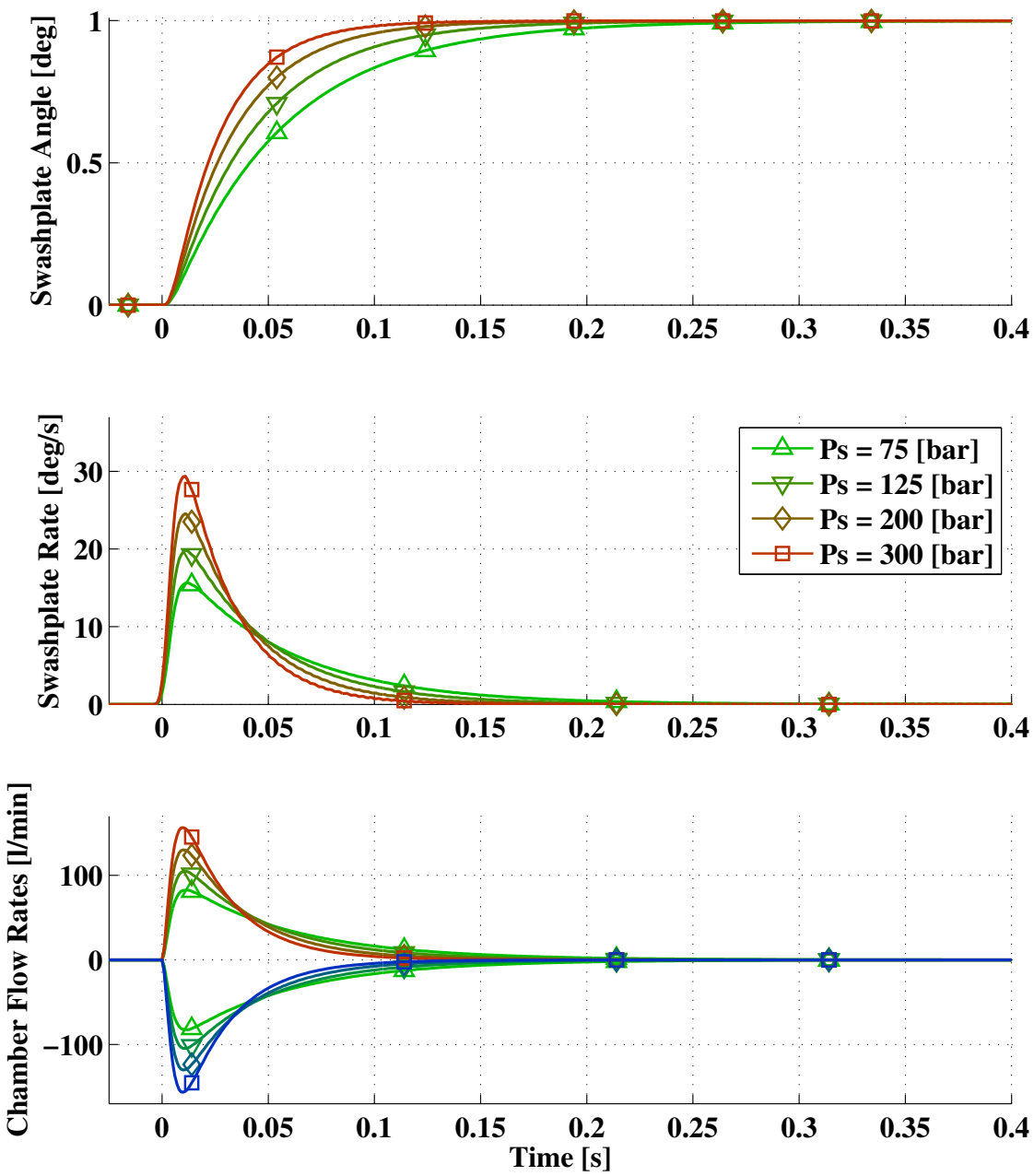

Fig. 3.2: Swashplate step response for unit degree step input at high supply pressures

and (2.23):

$$Q_A = c_{v,1}\mathrm{sg}(x_v)\mathrm{sign}(P_s - P_A)\sqrt{|P_s - P_A|}$$

$$- c_{v,2}\mathrm{sg}(-x_v)\mathrm{sign}(P_A - P_T)\sqrt{|P_A - P_T|} \qquad (2.22) \quad \text{repeated}$$

Using actuator chamber A as an example, the chamber flow rate is a function of $\sqrt{|P_s - P_A|}$ for a positive valve displacement. As pressure increases, flow rate increases by the square root of supply pressure. In order to double the flow rate, assuming all other parameters are held constant, the supply pressure must be quadrupled. This agrees with the simulation findings in which small pressure changes at low supply pressures had a much greater impact on the step response of the swashplate.

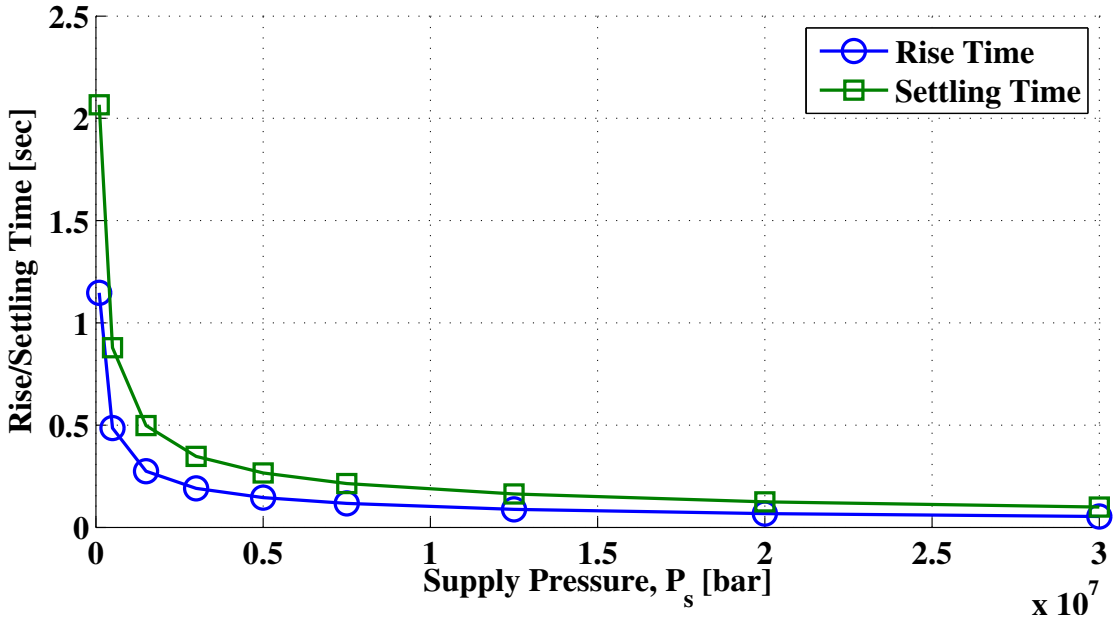

Fig. 3.3: Rise time (blue) and settling time (green) for swashplate step response over a range of supply pressures

Figure 3.3 shows the rise time and settling time of the swashplate step response as a function of supply pressure. Rise time is defined as the time it takes the swashplate to move between 10% and 90% displacement, or from 0.1° to 0.9°. In the present study, settling time is defined as the time it takes the swashplate to achieve and maintain at most a ±2% error between desired and actual displacement,

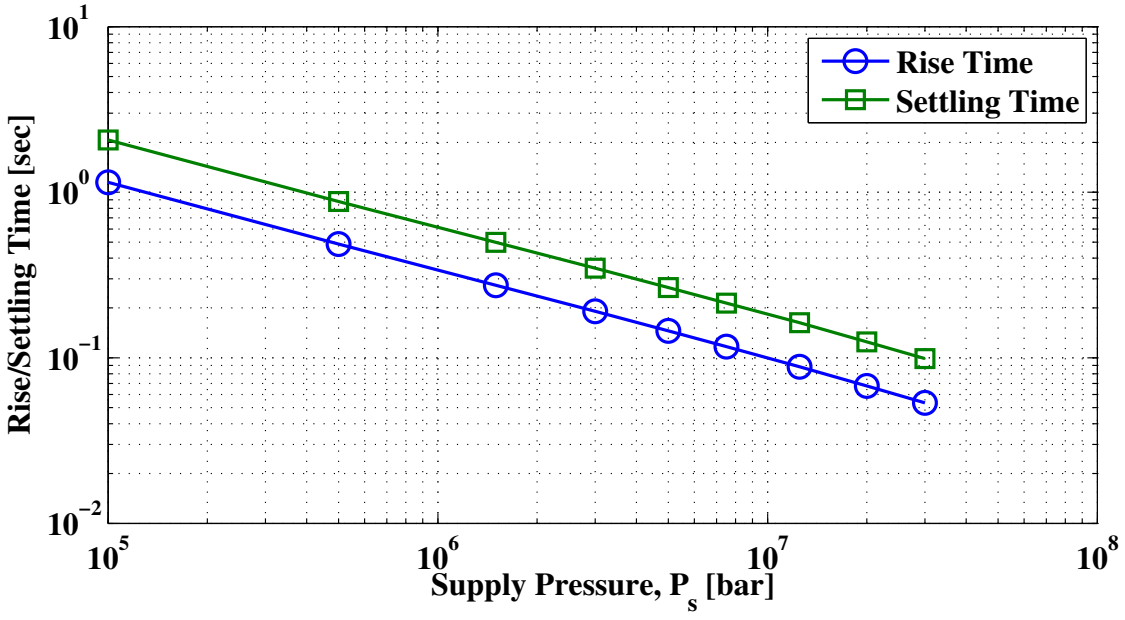

Fig. 3.4: Rise time (blue) and settling time (green) for swashplate step response over a range of supply pressures on a log-log scale

meaning remain between 0.98° and 1.02°. The exponential response of the rise and settling time can be seen in Fig. 3.4. The slope, -0.5, shows an inverse square root relationship between supply pressure and rise and settling time. To decrease rise time by a factor of two, the supply pressure must be quadrupled.

3.2.2 Valve Pressure Drop

The next parameter studied is pressure drop, P_v. Pressure drop is defined as supply pressure minus return pressure, minus load pressure, that is

$$P_v = P_s - P_T - P_l \tag{3.1}$$

where load pressure P_l is calculated from the external force on the actuator piston using

$$P_l = \frac{F_{ext}}{A_p} \tag{3.2}$$

To perform this sweep, return pressure was increased to reduce the valve pressure drop. Table 3.3 lists the pressure drops used during this study.

Category	Pressure Drop [bar]
Low drops	1, 5, 15, 25, 50
High drops	75. 100, 150, 175, 195

Table 3.3: Valve pressure drops, P_v, used in study.

Figure 3.5 shows the swashplate step response for low valve pressure drops. Situations such as these occur when there is a large external force on the actuator, or when the difference between supply pressure P_s and return pressure P_T is small. The results are similar to changes in the supply pressure above. Like in the supply pressure study above, the focus will be on Eqs. (2.22) and (2.23).

When there is a large external force on the actuator, extra pressure is being applied to the actuator chambers. This phenomena is discussed in Section 2.4.3, when discussing the effects of external forcing on actuator trim pressures. First, assume the actuator is at rest and no external forces are applied, then chamber pressures A and B will equalize to P_{eq}. Now, while still at rest, apply a large external force. This causes the pressure in chamber A to increase, as described by

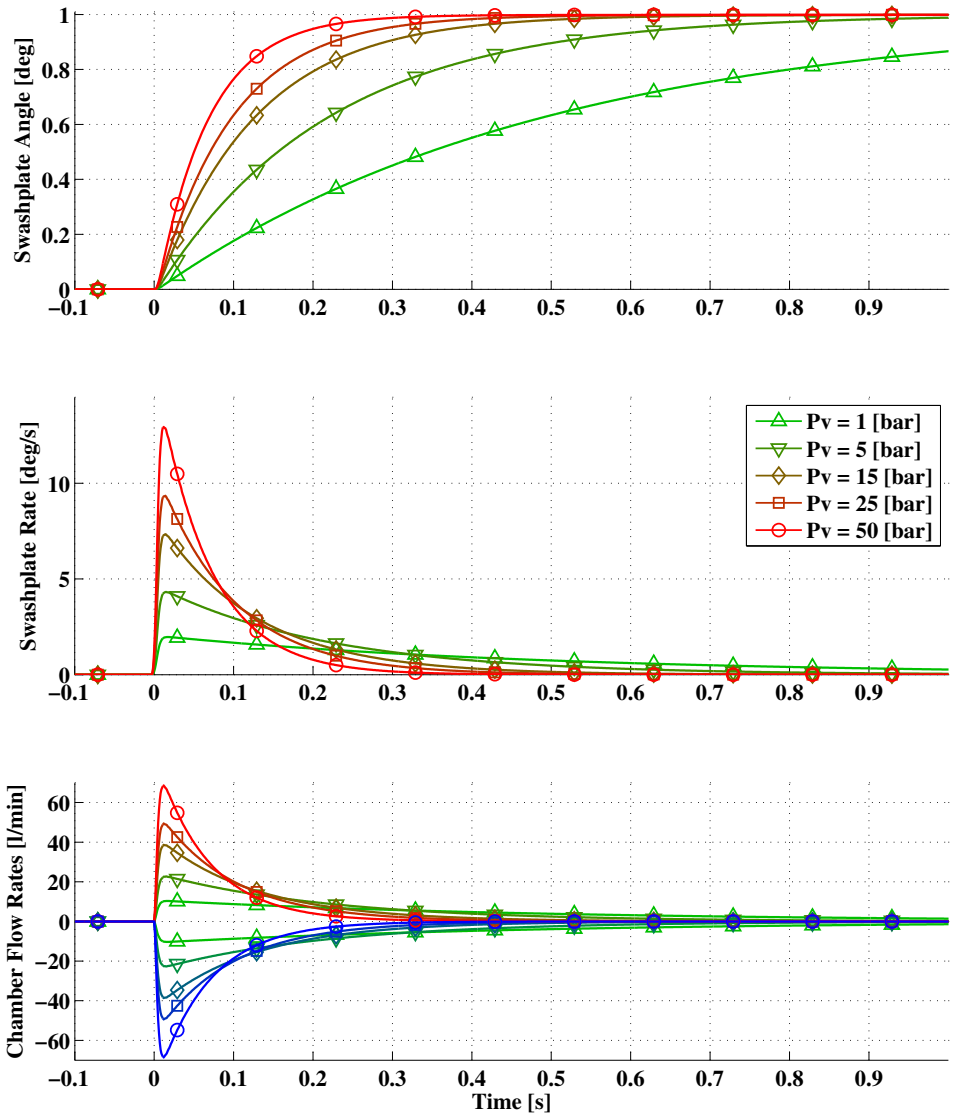

Fig. 3.5: Swashplate step response for unit degree step input at low pressure drops

Eq. (2.168) and the pressure in chamber B to decrease, as described by Eq. (2.169):

$$x_3 = P_{eq} + \frac{F_{act,1}}{A_p} \qquad (2.168) \quad \text{repeated}$$

$$x_4 = P_{eq} - \frac{F_{act,1}}{\alpha A_p} \qquad (2.169) \quad \text{repeated}$$

These pressures, P_A and P_B can be found using the equations for flow rates, Eqs. (2.22) and (2.23). For a positive valve displacement, as external force increases, P_A in-

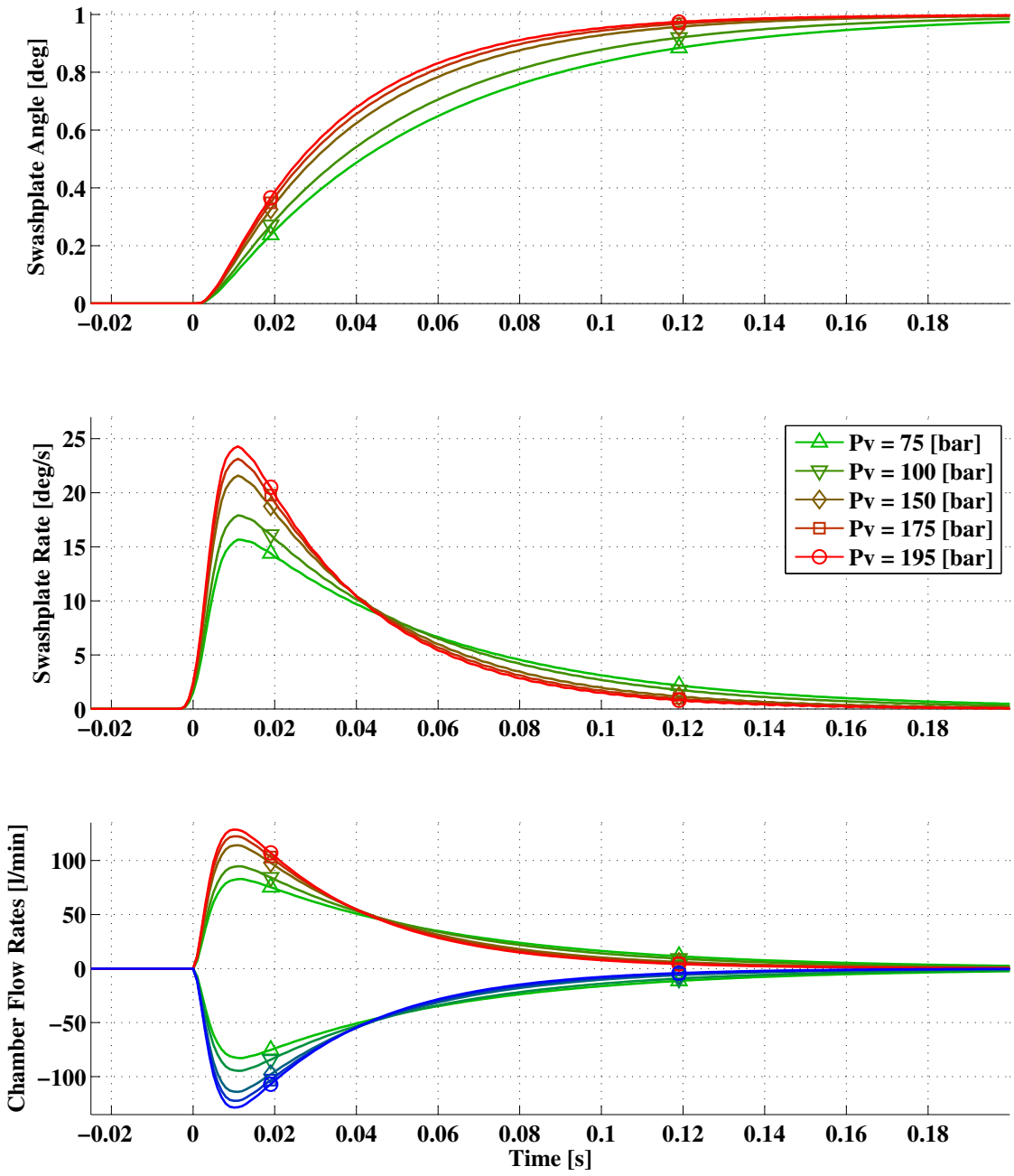

Fig. 3.6: Swashplate step response for unit degree step input at high pressure drops

creases, thus the $\sqrt{|P_s - P_A|}$ term in Eq. (2.22) decreases and P_B decreases, thus the $\sqrt{|P_B - P_T|}$ term in Eq. (2.23) decreases.

Raising P_T has the same effect. As P_T increases, equalized chamber pressures

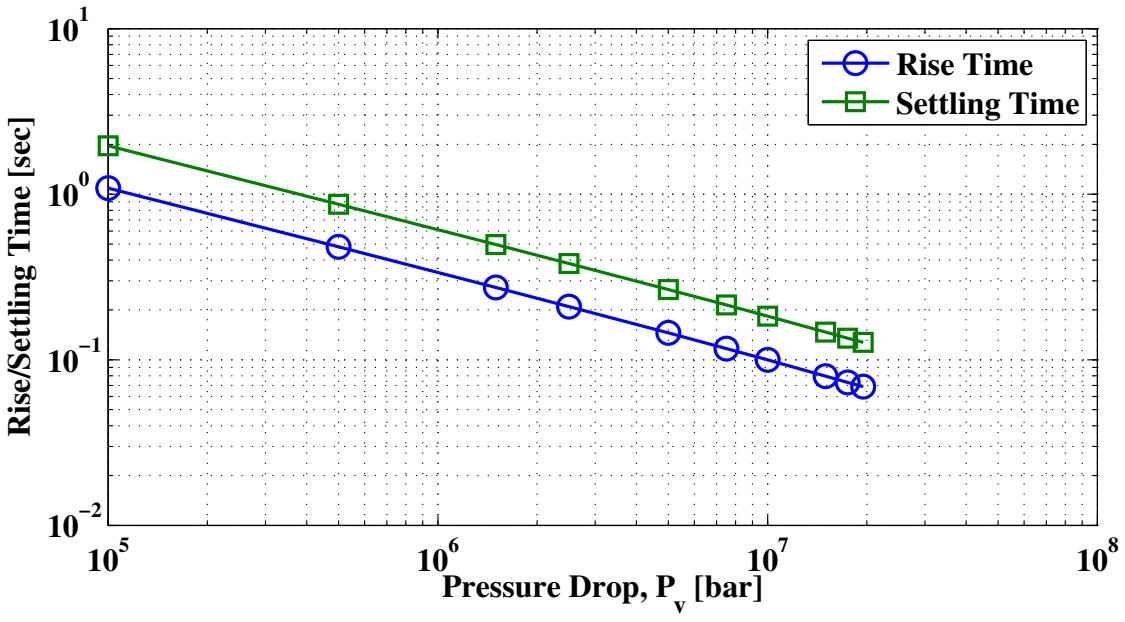

Fig. 3.7: Rise time (blue) and settling time (green) for swashplate step response over a range of pressure drops on a log-log scale

P_A and P_B increase. This reduces the $\sqrt{|P_s - P_A|}$ term found in Eq. (2.22), and ultimately decreases flow rate to and from the actuator.

The effects of larger values of valve pressure drop can be seen in Fig. 3.6. As valve pressure drop increases, small changes in P_v have little to no effect on the step response. Figure 3.7 shows the rise and settling time for different valve pressure drops. The inverse-square root relationship between valve pressure drop and rise and settling time can be seen.

3.2.3 Valve Flow Coefficient

Valve flow coefficient has a very prominent effect on the swashplate step response. Valve flow coefficient, a function of valve geometry, can be calculated using

Eq. (2.18). The valve flow coefficient can be found in the flow equations, Eqs. (2.22) and (2.23).

Category	Flow coefficients (x10^{-7})
Low coefficients	1, 2.5, 5, 7.5, 10
High coefficients	10, 25, 40, 50

Table 3.4: Valve flow coefficients, c_v, used in study

The parameters affecting the valve flow coefficient are valve spool diameter, d_v, valve discharge coefficient, α_d, and fluid density ρ. As the valve spool diameter increases, more fluid can travel through the valve per unit time and c_v increases. As the fluid density increases, viscous and inertial effects of the fluid reduce the flow rate through the valve and c_v decreases. The valve discharge coefficient summarizes the effects of the dynamic interaction between the valve spool and the orifice, as the discharge coefficient decreases, so does the flow coefficient. Table 3.4 shows the different values of c_v used for this study. During this simulation, all four valve flow coefficients were modified.

Figures 3.8 and 3.9 show the swashplate step response for low and high valve flow coefficients, respectively. The coefficient C_v linearly scales the maximum flow rate as can be seen by Fig. 3.10. As valve flow coefficient increases, so does the maximum flow rate.

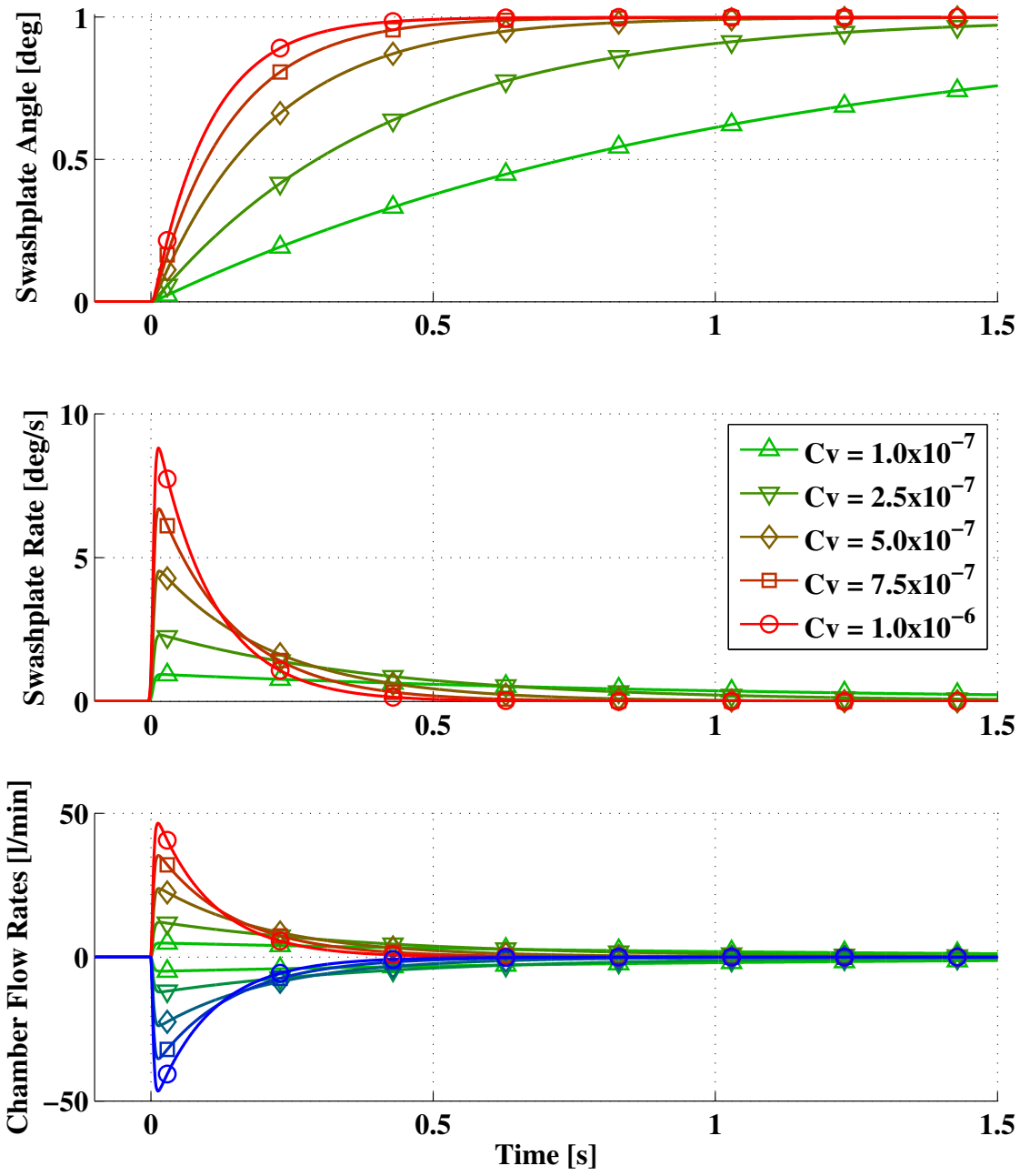

Fig. 3.8: Swashplate step response for unit degree step input for low valve flow coefficients

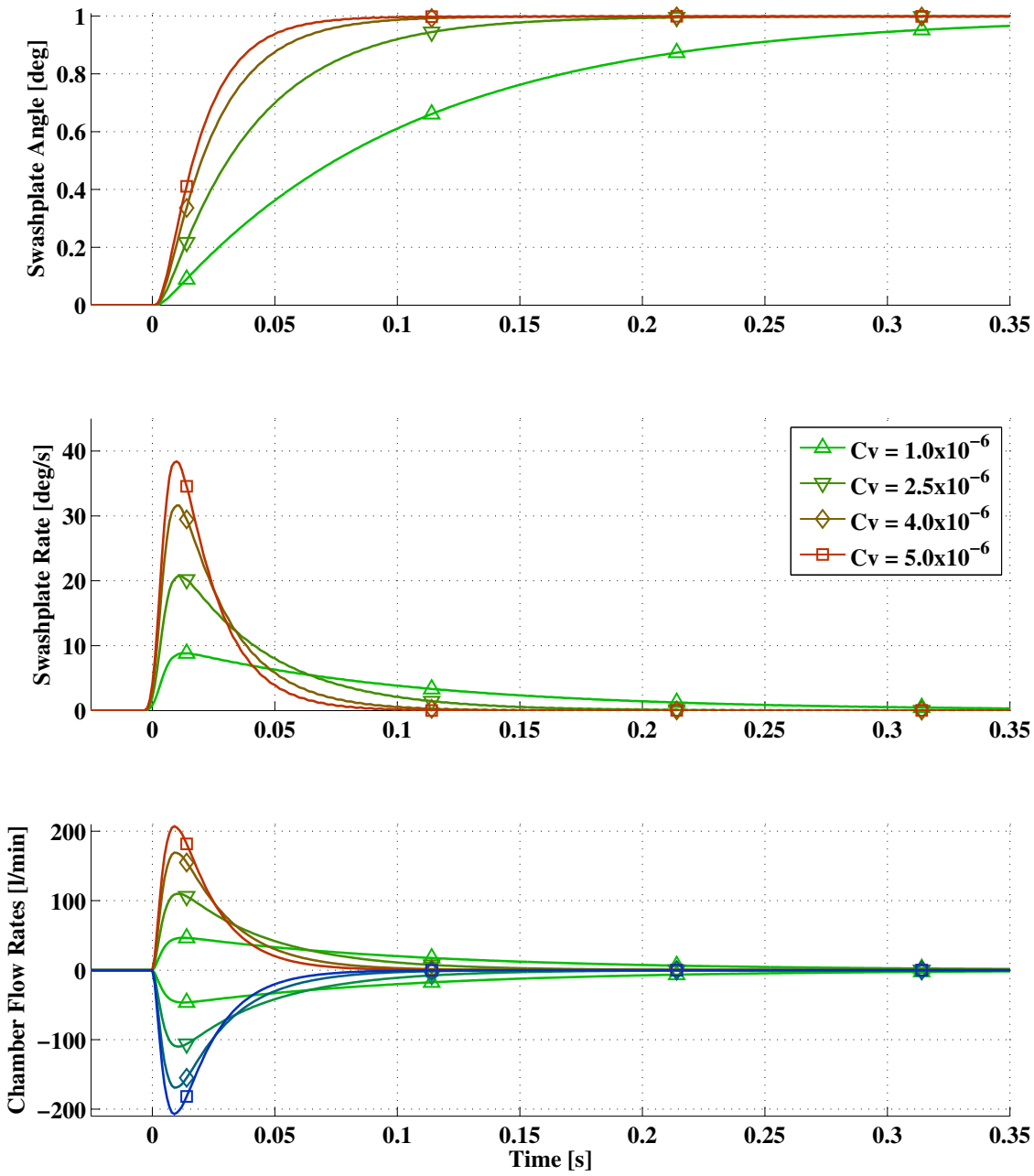

Fig. 3.9: Swashplate step response for unit degree step input for high valve flow coefficients

3.2.4 Piston Area

The internal actuator cross sectional area, on which the working fluid acts, is defined by the actuator piston area, A_p. Table 3.5 lists the actuator piston areas

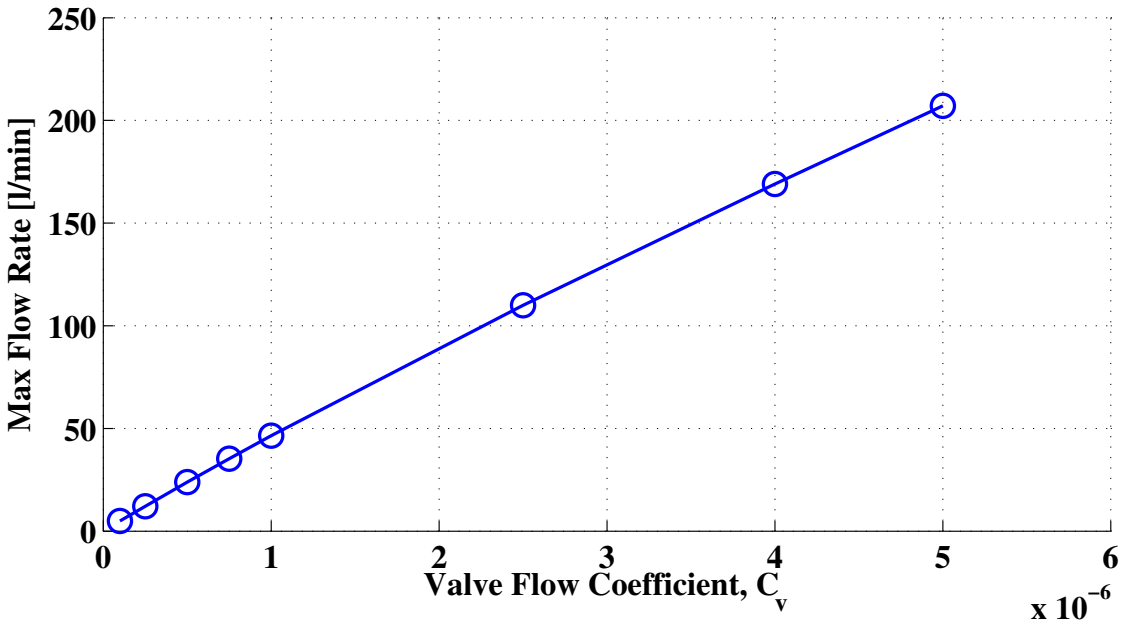

Fig. 3.10: Rise time (blue) and settling time (green) for swashplate step response over a range of valve flow coefficients

examined.

Category	Piston Area $[m^2]$
Piston Area	0.05, 0.04, 0.03, 0.02, 0.01

Table 3.5: Piston areas, A_p, used in study

Equations (2.9) and (2.10), used to calculate total volume of actuator chambers A and B, both contain A_p. As piston area increases, the effects of piston displacement, x_p on the chamber volumes are increased. Equations (2.31) and (2.32) describe the rate of change of pressure in chambers A and B respectively.

$$0 = V_A(x_1)\dot{x_3} - E'(x_3)[Q_A(x_3, x_5) - A_p x_2 + Q_{Li}(x_3, x_4)] \quad (2.31) \quad \text{repeated}$$

$$0 = V_B(x_1)\dot{x_4} - E'(x_4)[Q_B(x_4, x_5) + \alpha A_p x_2 - Q_{Li}(x_3, x_4)] \quad (2.32) \quad \text{repeated}$$

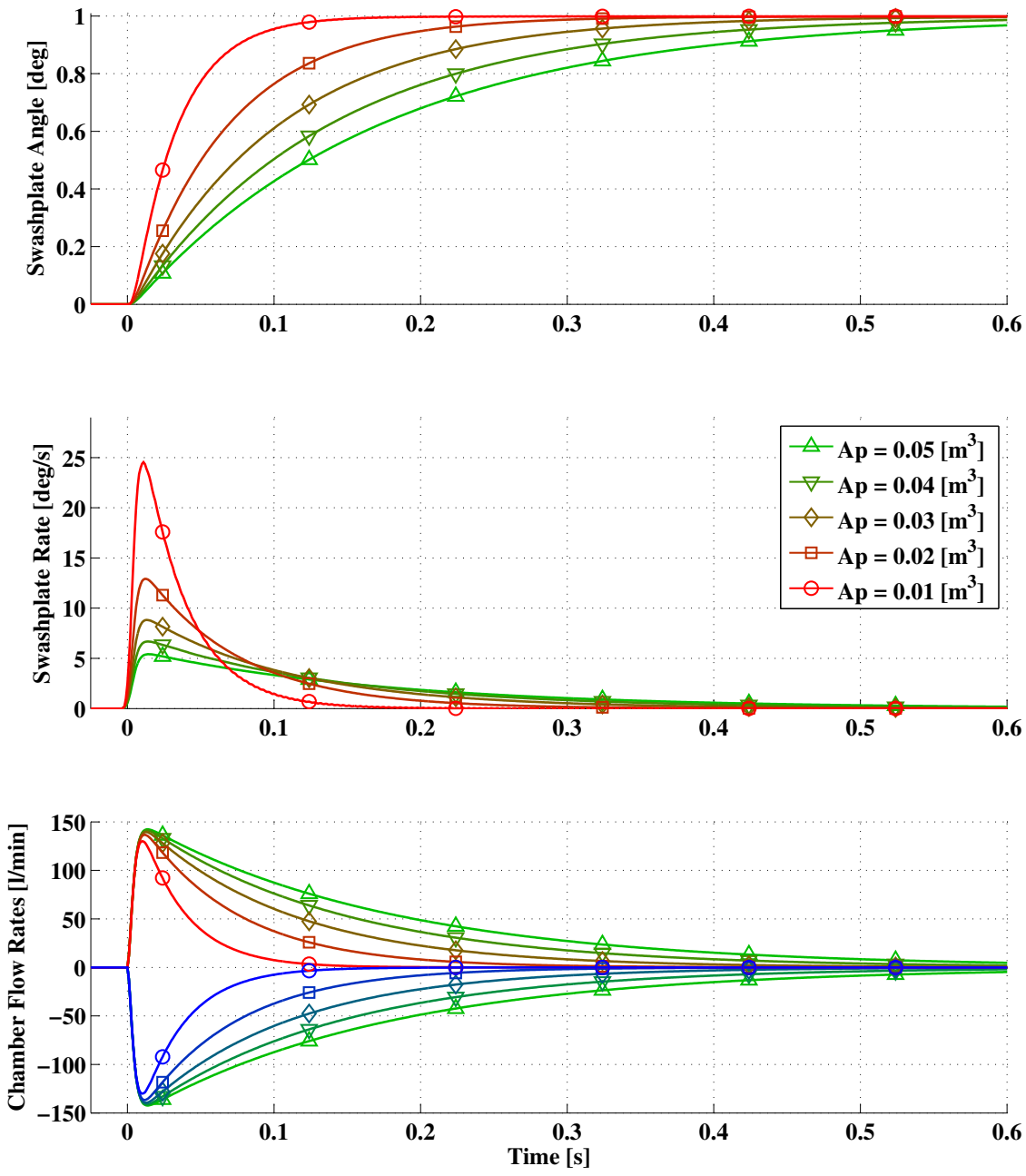

Fig. 3.11: Swashplate step response for unit degree step input over a range of actuator piston areas

As chamber volume increases, pressure change is damped. As actuator piston area increases, actuator chamber pressure changes decrease, effectively damping actuator

displacement.

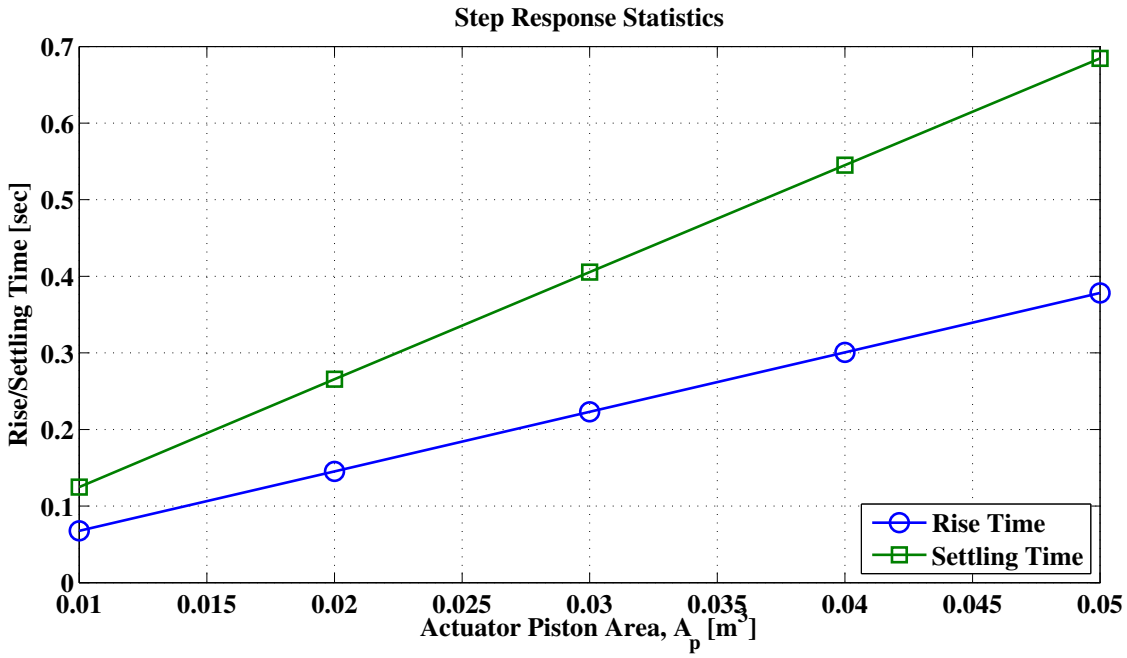

Fig. 3.12: Rise time (blue) and settling time (green) for swashplate step response over a range of actuator piston areas

Figure 3.11 shows the step response of chamber flow rate Q_A and Q_B (bottom plot), actuator rate $\dot{x}_p$ (middle plot), and swashplate angle (top plot), over a range of piston areas. All configurations share approximately the same maximum chamber flow rate, however the configurations with larger actuator piston area have more volume to fill, and thus require a higher flow rate over a longer period of time. The factor limiting actuator displacement is the amount of fluid needed to expand the actuator chamber volume.

Figure 3.12 shows the relationship between actuator piston area and rise and settling time. This relationship is linear (note that this figure is not on a log-log

scale like Figs. 3.4 and 3.7).

3.2.5 Actuator Test Cases

With a basic understanding of how different key actuator parameters affect actuator step response, four actuators will be described here that will be referred to throughout the rest of the thesis.

The first actuator is a primary servo actuator transfer function and can be considered representative of the primary servo actuator of the UH-60.

$$\frac{\theta_{1s}}{\delta_{lon}} = \frac{1}{0.00114s^2 + 0.0463s + 1} \tag{3.3}$$

This actuator configuration will be referred to as the "UH-60 actuator" model, and is completely defined by its transfer function. Its detailed geometry and mechanical properties are considered proprietary, and therefore are not available. The second actuator, referred to as the "baseline" actuator, is designed to reproduce the step response of the UH-60 actuator. The third actuator model, referred to as the "sluggish" actuator, is configured to be a slow actuator, experiencing heavy rate saturation. Both the supply pressure and valve flow coefficient have been reduced while simultaneously increasing the piston area. The fourth actuator is configured to have a quick step response. This actuator will be called the "agile" model. Supply pressure and valve flow coefficient were increated and piston area decreased. Design parameters used for the these actuators can be found in table 3.7.

Figure 3.13 shows the step response for each actuator for a unit degree swashplate displacement. Table 3.8 show the rise time and settling time for the three

Actuator Parameter	Baseline	Sluggish	Agile
Supply Pressure, P_s $[bar]$	200	150	300
Return Pressure, P_T $[bar]$	1	1	1
Valve Flow Coefficient, C_v	3x10^{-6}	2x10^{-6}	6x10^{-6}
Internal Leakage Coefficient, C_{li}	0	0	0
Pipeline A/B Volume, $V_{pv_{A,B}}$ $[m^3]$	0.01	0.01	0.01
Piston Area, A_p $[m^2]$	0.01	0.015	0.01
Chamber Area Ratio, α	1	1	1
Piston Mass, M_p	6.6	6.6	6.6
Fluid Density, ρ	890	890	890

Table 3.6: Model parameters for baseline, sluggish, and agile actuator models

Actuator Parameter	Baseline	Sluggish	Agile
Supply Pressure, P_s $[bar]$	200	150	300
Valve Flow Coefficient, C_v	3x10^{-6}	2x10^{-6}	6x10^{-6}
Piston Area, A_p $[m^2]$	0.01	0.015	0.01

Table 3.7: Model parameters for baseline, sluggish, and agile actuator models

actuator models. The δ values represent the difference, in milliseconds, of the sluggish and agile actuator model's rise and settling times to the baseline actuator model. The sluggish actuator takes a little over 400 milliseconds longer to settle, compared to the baseline model, whereas the agile actuator settles in a little over 100 milliseconds faster than the baseline model.

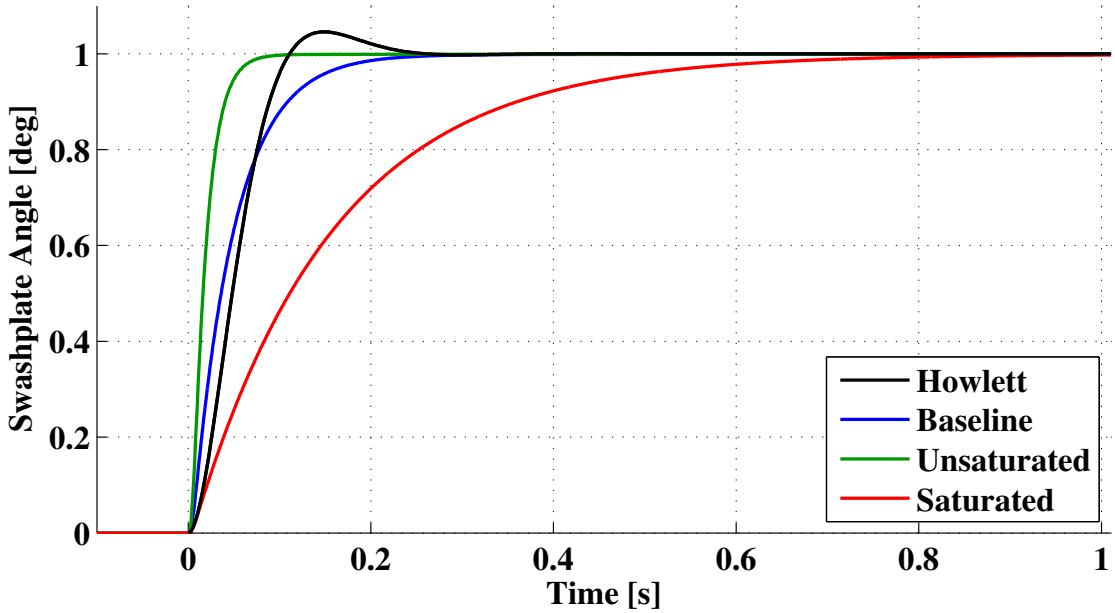

Fig. 3.13: Swashplate step response for unit degree step input for UH-60, baseline, sluggish, and agile actuator models

Actuator Config.	Rise Time $[ms]$	δ_{rt} $[ms]$	Settling Time $[ms]$	δ_{st} $[ms]$
Sluggish	339.3	239.4	614.7	431.2
Baseline	99.9		183.5	
Agile	34.8	-65.1	65.3	-118.2

Table 3.8: Step response rise time and settling time for baseline, sluggish, and agile actuator models

Figures 3.14 and 3.15 show the actuator rate and chamber A flow rate time histories for each of the actuator step response simulations. Table 3.9 lists the maximum actuator rate and max chamber flow rate corresponding to the unit degree swashplate step response. The actuators themselves have vastly different velocities

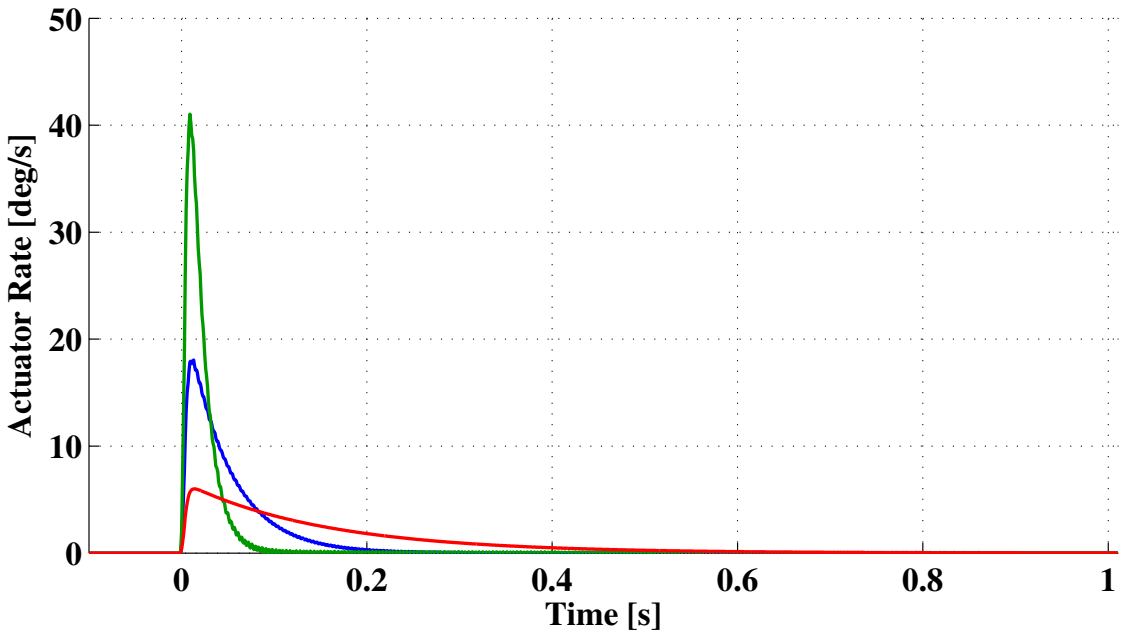

Fig. 3.14: Swashplate rates for unit degree step input for baseline, sluggish, and agile actuator models

but because the actuator, and swashplate, displacement is so short, these velocities manifest themselves as millisecond delays in the swashplate step response.

Actuator Config.	Max Rate [deg/sec]	Max Flow Rate [l/min]
Sluggish	6.15	47.29
Baseline	19.28	94.59
Agile	42.26	214.00

Table 3.9: Step response max swashplate rate and max flow rate for baseline, sluggish, and agile actuator models

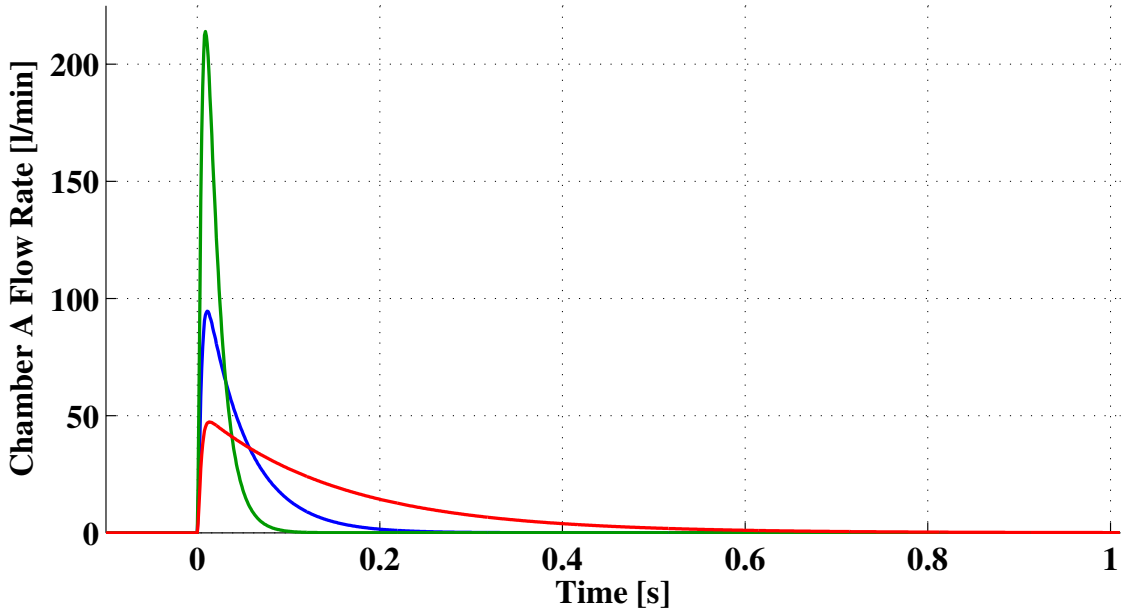

Fig. 3.15: Chamber A flow rate for unit degree step input for baseline, sluggish, and agile actuator models

Chapter 4

Rotorcraft-Actuator Linearized Model

4.1 Overview

The equations of motion describing the rotorcraft dynamics used in the present study are all written as first-order ordinary differential equations. Because of this, it is easy to perform a numerical linearization based on a first-order Taylor series expansion of the nonlinear system about a trimmed equilibrium position. Creating the small-perturbation linearized model is an efficient way to extract a state-space model of the rotorcraft.

4.2 Linearization Methodology

In the present study, the rotorcraft equations are written in the form

$$\mathbf{f}(\dot{\mathbf{y}}, \mathbf{y}, \mathbf{u}; t) = \mathbf{0} \tag{4.1}$$

In trim, using the subscript $(\,)_0$ to denote a trim condition, the equations become

$$\mathbf{f}(\dot{\mathbf{y}}_0, \mathbf{y}_0, \mathbf{u}_0; t) = \mathbf{0} \tag{4.2}$$

Using a Taylor series expansion about Equation 4.2, Equation 4.1 can be rewritten as

$$\mathbf{0} = \mathbf{f}(\dot{\mathbf{y}}_0, \mathbf{y}_0, \mathbf{u}_0; t) + \left.\frac{\partial \mathbf{f}}{\partial \dot{\mathbf{y}}}\right|_{trim} \Delta\dot{y} + \left.\frac{\partial \mathbf{f}}{\partial \mathbf{y}}\right|_{trim} \Delta y + \left.\frac{\partial \mathbf{f}}{\partial \mathbf{u}}\right|_{trim} \Delta u + \mathcal{O}\left(\|\Delta\dot{\mathbf{y}}\|^2, \|\Delta\mathbf{y}\|^2\|\Delta\mathbf{u}\|^2\right) \quad (4.3)$$

where

$$\Delta\dot{\mathbf{y}} \equiv \dot{\mathbf{y}} - \dot{\mathbf{y}}_0 \quad (4.4)$$

$$\Delta\mathbf{y} \equiv \mathbf{y} - \mathbf{y}_0 \quad (4.5)$$

$$\Delta\mathbf{u} \equiv \mathbf{u} - \mathbf{u}_0 \quad (4.6)$$

By assuming small perturbations, the higher order terms can be neglected and the resulting linearized model

$$0 = \left.\frac{\partial \mathbf{f}}{\partial \dot{\mathbf{y}}}\right|_{trim} \Delta\dot{\mathbf{y}} + \left.\frac{\partial \mathbf{f}}{\partial \mathbf{y}}\right|_{trim} \Delta\mathbf{y} + \left.\frac{\partial \mathbf{f}}{\partial \mathbf{u}}\right|_{trim} \Delta\mathbf{u} \quad (4.7)$$

is used to describe small perturbation motion about trim. The partial derivatives taken about trim can be renamed as described below.

$$\left.\frac{\partial \mathbf{f}}{\partial \dot{\mathbf{y}}}\right|_{trim} \equiv [E(t)] \quad (4.8)$$

$$\left.\frac{\partial \mathbf{f}}{\partial \mathbf{y}}\right|_{trim} \equiv [F(t)] \quad (4.9)$$

$$\left.\frac{\partial \mathbf{f}}{\partial \mathbf{u}}\right|_{trim} \equiv [G(t)] \quad (4.10)$$

Equation 4.7 can be rearranged to form

$$[E(t)]\Delta\dot{\mathbf{y}} = -[F(t)]\Delta\mathbf{y} - [G(t)]\Delta\mathbf{u} \quad (4.11)$$

and

$$\Delta\dot{\mathbf{y}} = -[E(t)]^{-1}[F(t)]\Delta\mathbf{y} - [E(t)]^{-1}[G(t)]\Delta\mathbf{u} \tag{4.12}$$

where

$$[A(t)] = [E(t)]^{-1}[F(t)] \tag{4.13}$$

$$[B(t)] = [E(t)]^{-1}[G(t)] \tag{4.14}$$

$[A(t)]$ and $[B(t)]$ are the linearized state space matrices used for linearization analysis.

$[E(t)]$, $[F(t)]$, and $[G(t)]$ are calculated using

$$[E(t)] = \left[\frac{\partial \mathbf{f}}{\partial \dot{\mathbf{y}}}\right]_{trim} = \left[\begin{array}{ccccccc} \frac{\partial \mathbf{f}}{\partial \dot{y}_1} & \frac{\partial \mathbf{f}}{\partial \dot{y}_2} & \cdots & \frac{\partial \mathbf{f}}{\partial \dot{y}_k} & \cdots & \frac{\partial \mathbf{f}}{\partial \dot{y}_n} \end{array}\right]_{trim} \tag{4.15}$$

$$[F(t)] = \left[\frac{\partial \mathbf{f}}{\partial \mathbf{y}}\right]_{trim} = \left[\begin{array}{ccccccc} \frac{\partial \mathbf{f}}{\partial y_1} & \frac{\partial \mathbf{f}}{\partial y_2} & \cdots & \frac{\partial \mathbf{f}}{\partial y_k} & \cdots & \frac{\partial \mathbf{f}}{\partial y_n} \end{array}\right]_{trim} \tag{4.16}$$

$$[G(t)] = \left[\frac{\partial \mathbf{f}}{\partial \mathbf{u}}\right]_{trim} = \left[\begin{array}{ccccccc} \frac{\partial \mathbf{f}}{\partial u_1} & \frac{\partial \mathbf{f}}{\partial u_2} & \cdots & \frac{\partial \mathbf{f}}{\partial u_k} & \cdots & \frac{\partial \mathbf{f}}{\partial u_m} \end{array}\right]_{trim} \tag{4.17}$$

for n states and m controls.

Central differencing is used to numerically calculate column k for each matrix using

$$\left\{\frac{\partial \mathbf{f}}{\partial \dot{y}_k}\right\}_{trim} \approx \frac{\mathbf{f}(\dot{\mathbf{y}}_0 + \Delta\dot{\mathbf{y}}_k, \mathbf{y}_0, \mathbf{u}_0; t) - \mathbf{f}(\dot{\mathbf{y}}_0 - \Delta\dot{\mathbf{y}}_k, \mathbf{y}_0, \mathbf{u}_0; t)}{2\Delta\dot{y}_k} \tag{4.18}$$

$$\left\{\frac{\partial \mathbf{f}}{\partial y_k}\right\}_{trim} \approx \frac{\mathbf{f}(\dot{\mathbf{y}}_0, \mathbf{y}_0 + \Delta\mathbf{y}_k, \mathbf{u}_0; t) - \mathbf{f}(\dot{\mathbf{y}}_0, \mathbf{y}_0 - \Delta\mathbf{y}_k, \mathbf{u}_0; t)}{2\Delta y_k} \tag{4.19}$$

$$\left\{\frac{\partial \mathbf{f}}{\partial u_k}\right\}_{trim} \approx \frac{\mathbf{f}(\dot{\mathbf{y}}_0, \mathbf{y}_0, \mathbf{u}_0 + \Delta\mathbf{u}_k; t) - \mathbf{f}(\dot{\mathbf{y}}_0, \mathbf{y}_0, \mathbf{u}_0 - \Delta\mathbf{u}_k; t)}{2\Delta u_k} \tag{4.20}$$

where

$$\Delta\dot{\mathbf{y}}_k = \begin{bmatrix} 0 & 0 & \cdots & \Delta\dot{y}_k & \cdots & 0 \end{bmatrix}^T \tag{4.21}$$

$$\Delta\mathbf{y}_k = \begin{bmatrix} 0 & 0 & \cdots & \Delta y_k & \cdots & 0 \end{bmatrix}^T \tag{4.22}$$

$$\Delta\mathbf{u}_k = \begin{bmatrix} 0 & 0 & \cdots & \Delta u_k & \cdots & 0 \end{bmatrix}^T \tag{4.23}$$

$$\{\dot{\mathbf{x}}_H\} = [A_H]\{\mathbf{x}_H\} + [B_H]\{\delta\} \tag{4.24}$$

$$\begin{Bmatrix} \dot{\mathbf{x}}_H \\ \dot{\mathbf{x}}_A \end{Bmatrix} = \begin{bmatrix} A_{HH} & A_{HA} \\ A_{AH} & A_{AA} \end{bmatrix} \begin{Bmatrix} \mathbf{x}_H \\ \mathbf{x}_A \end{Bmatrix} + \begin{bmatrix} B_H \\ A_H \end{bmatrix} \{\delta\} \tag{4.25}$$

$$\{\dot{\mathbf{x}}_A\} = [A_A]\{\mathbf{x}_A\} + [B_A]\{\delta\} \tag{4.26}$$

Three different linearized models were computed. The first model, Case A, does not include actuator dynamics. Equation (4.24) shows the state space representation of this model. In the next model, Case B, the actuator dynamics are fully coupled with the rest of the rotorcraft dynamics. The state space representation for Case B is found in Eq. (4.25). In the last model, Case C, linearized models of the actuators and of the aircraft are extracted independently, and the transfer functions are combined. This model uses state-space Eqs. (4.24) and (4.26). Figure 4.1 shows an overview of each case (HeliUM is the name of the simulation used in the study).

The A_A and B_A actuator state space matrices account for the 18 different states of the actuators which must be converted to swashplate angles as the output. The C matrix of the state space model converts key actuator states, in this case actuator displacements, into swashplate angles. Equations 2.145, 2.146, and 2.147

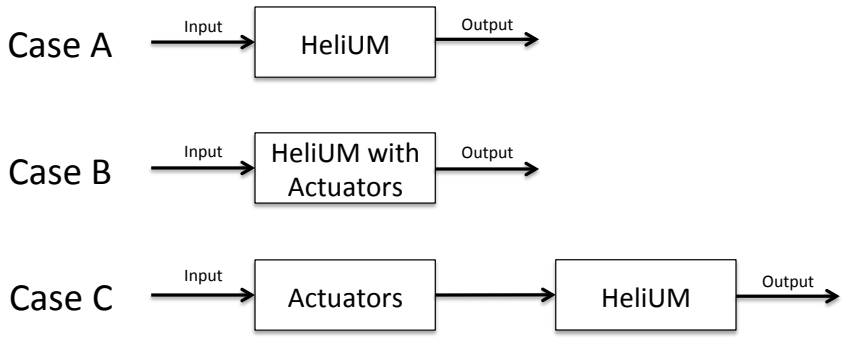

Fig. 4.1: Overview of linearized test cases

which are originally used to convert reference swashplate angles to desired actuator displacements can be inverted to convert actual actuator displacements to actual swashplate angles.

After inverting to solve for swashplate angles, the equations are as follows:

$$\theta_{1c} = \frac{1}{\kappa}\left[-x_1 + \frac{x_7}{2} + \frac{x_{13}}{2}\right] \tag{4.27}$$

$$\theta_{1s} = \frac{1}{\kappa}\left[\frac{x_7}{2} - \frac{x_{13}}{2}\right] \tag{4.28}$$

$$\theta_0 = \frac{1}{\kappa}\left[\frac{x_7}{2} + \frac{x_{13}}{2}\right] \tag{4.29}$$

where x_1, x_7, and x_{13} represent displacements of actuators 1, 2, and 3, respectively. These equations can then be put in matrix form.

$$\begin{Bmatrix} \theta_{1c} \\ \theta_{1s} \\ \theta_0 \end{Bmatrix} = \frac{1}{\kappa}\begin{bmatrix} -1 & 0.5 & 0.5 \\ 0 & 0.5 & -0.5 \\ 0 & 0.5 & 0.5 \end{bmatrix}\begin{Bmatrix} x_1 \\ x_7 \\ x_{13} \end{Bmatrix} \tag{4.30}$$

This matrix can now be expanded to include states x_1 through x_{18} resulting in the state space C_A matrix for the actuator linearization.

$$\begin{Bmatrix} \theta_{1c} \\ \theta_{1s} \\ \theta_0 \end{Bmatrix} = \frac{1}{\kappa} \underbrace{\begin{bmatrix} -1 & \cdots & 0.5 & \cdots & 0.5 & \cdots \\ 0 & \cdots & 0.5 & \cdots & -0.5 & \cdots \\ 0 & \cdots & 0.5 & \cdots & 0.5 & \cdots \end{bmatrix}}_{\stackrel{def}{=} [C_A]} \begin{Bmatrix} x_1 \\ \vdots \\ x_7 \\ \vdots \\ x_{13} \\ \vdots \end{Bmatrix} \tag{4.31}$$

In Equation 4.31 the dots in the C_A matrix are zeros corresponding to the unused states.

The linearized actuator model only has 3 inputs, θ_{1c}, θ_{1s}, and θ_0. The actuator model does not affect pedal inputs. We can pass this fourth input directly to an output through the use of the D_A matrix of the state space model. We add a 1 in $D_A(4,4)$ to pass through the fourth input directly to the fourth output.

$$\Big[D\Big] = \begin{bmatrix} 0 & 0 & 0 & 0 \\ 0 & 0 & 0 & 0 \\ 0 & 0 & 0 & 0 \\ 0 & 0 & 0 & 1 \end{bmatrix} \tag{4.32}$$

Since we have passed through a fourth output, we must make a few changes to both the B_A and C_A state space matrices. The B_A matrix must have a fourth column of zeros appended. This ensures the fourth pedal input has no influence on the actuator states. Additionally, the C_A matrix must have a fourth row appended to ensure the states have no influence on the pedal output.

Now that the state space matrices have been extended to allow for four inputs

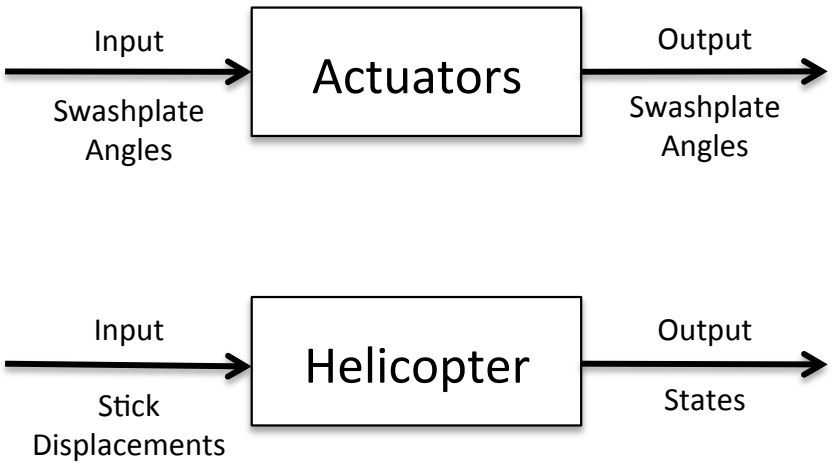

Fig. 4.2: Inputs and outputs of linearized actuator and linearized helicopter dynamics

and four outputs, the actual inputs and outputs must be compatible. As shown in Figure 4.2 the inputs and outputs of the linearized actuator model and linearized helicopter dynamics are different. In this case, the outputs from the linearized actuator model cannot be sent directly to the inputs of the linearized helicopter model. Additionally, in Case C, the inputs to the entire linearized system are different than both Case A and Case B. Instead of stick displacements as inputs, Case C uses swashplate angles as the input.

To remedy this situation, we need a transformation matrix to convert between swashplate angles and stick displacements. On a helicopter, this is often known as the "mixer". When the pilot adds collective or cyclic in the form of stick and pedal displacement, the input goes through the mixer and the resulting output is a set of

four swashplate angles, that is

$$\begin{Bmatrix} \theta_{1c} \\ \theta_{1s} \\ \theta_0 \\ \theta_{tr} \end{Bmatrix} = \Big[\text{Mixer}\Big] \begin{Bmatrix} \delta_{lat} \\ \delta_{lon} \\ \delta_{col} \\ \delta_{ped} \end{Bmatrix} \tag{4.33}$$

In the present study, the mixer matrix is representative of the UH-60 pitch control chain. Figure 4.3 shows the modified block diagram with the inclusion of the mixer matrix to convert stick displacements to swashplate angles as well as the inverse mixer matrix to convert swashplate angles to stick displacements.

$$\Big[\text{Mixer}\Big] = \begin{bmatrix} -1.6 & 0 & 0.256 & 0 \\ 0 & 2.83 & -0.464 & -1.6262 \\ 0 & 0 & 1.6 & 0 \\ 0 & 0 & 1.6 & -5.539 \end{bmatrix} \tag{4.34}$$

Now the transfer functions can be compiled for comparison. Case A and B are quite straightforward. The transfer functions can be computed as follows using the state space matrices derived from the each linearization repectively.

$$G(s) = C(sI - A)^{-1}B + D \tag{4.35}$$

Using this equation twice for Case A and Case B results in transfer functions $G_{HeliUM}(s)$ and $G_{HeliUM+Actuators}(s)$ respectively. These transfer functions will be labeled G_A and G_B for simplicity.

For Case C, the transfer function for the individual actuator linearized model

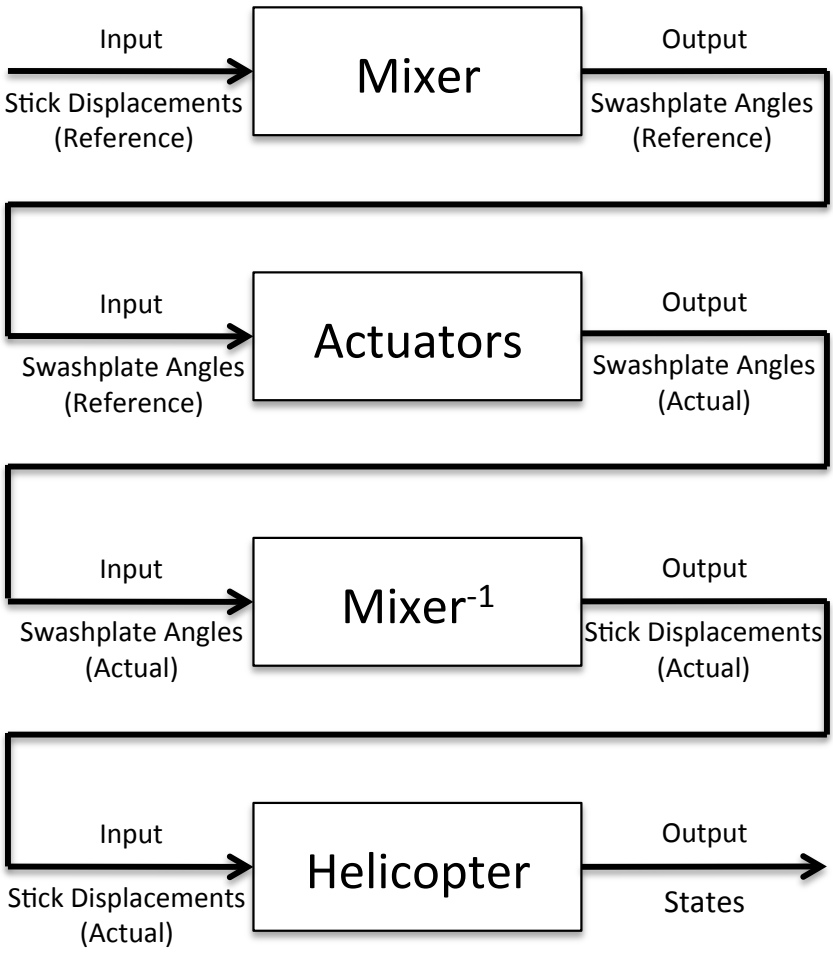

Fig. 4.3: Solution to input-output problem for test case C

must be computed. This transfer function $G_{Actuators}(s)$ is calculated using the state space matrices of the actuator model modified above and Equation 4.35.

Now we can order the transfer functions as shown in Figure 4.3. It's important to note, the "mixer" described in this study pertains only to the matrix used to convert stick displacements to swashplate angles.

$$G_C(s) = G_{HeliUM}[Mixer]^{-1} G_{Actuators}[Mixer] \tag{4.36}$$

Now the three transfer functions, G_A, G_B and G_C, are calculated, with uniform inputs and outputs, for comparison.

To make sure the linearized models are accurate frequency responses from the linearized Case B and Case C can be compared to one another. To do this comparison, the longitudinal frequency response of a rotorcraft in hover will be examined. The three actuator models discussed in Section 3.2.5 will be used.

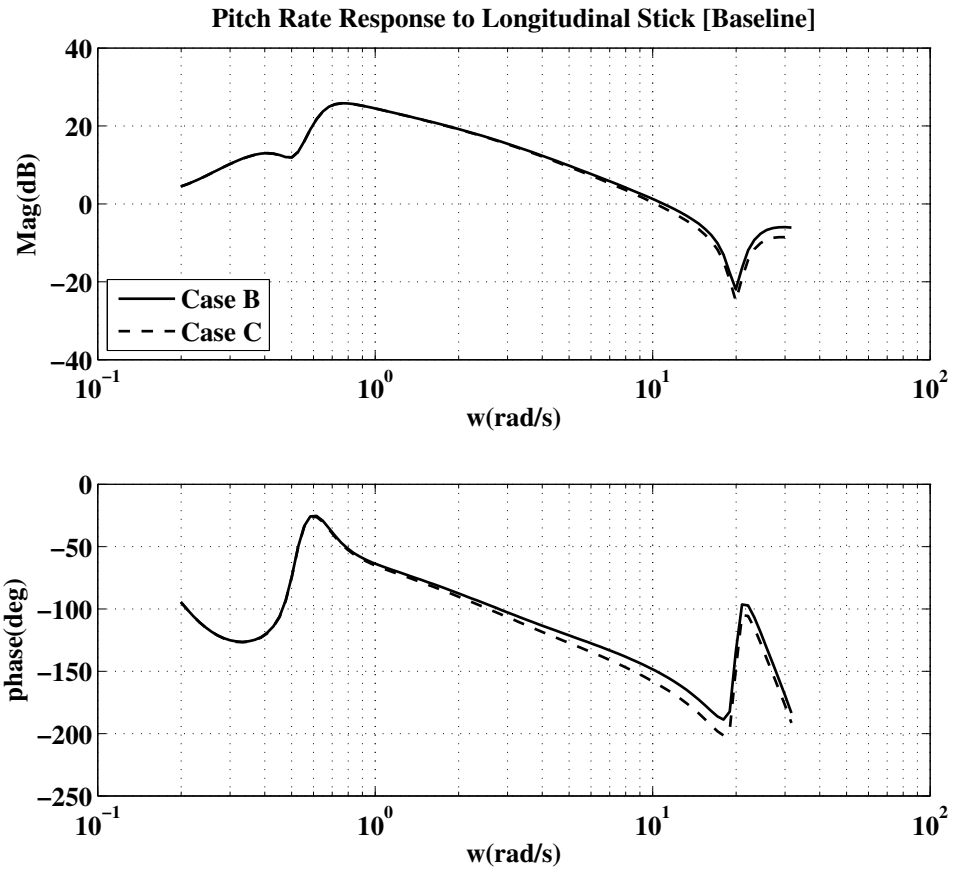

Fig. 4.4: Pitch rate response to longitudinal stick for rotorcraft in hover, using baseline actuator model Case B and Case C

Figure 4.4 shows the longitudinal frequency response of the rotorcraft-actuator baseline model. The blue line represents Case B, integrated rotorcraft and actuator

dynamics. The black dotted line represents Case C, rotorcraft and actuator dynamics linearized independently then combines using the methodology above. Good agreement is shown between the two models, verifying the methodology above and showing the integrated rotorcraft-hydraulic model is behaving appropriately.

Figure 4.5 shows the longitudinal frequency response of the rotorcraft-actuator agile model. Again, good agreement is shown between Case B and Case C.

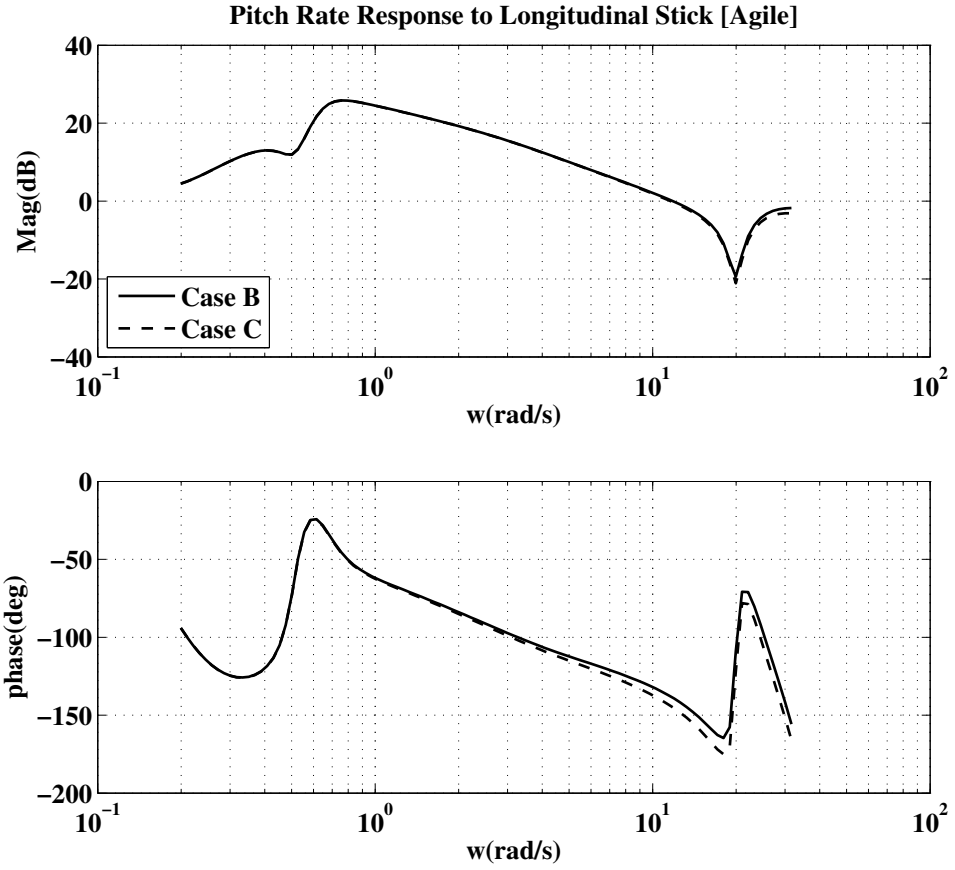

Fig. 4.5: Pitch rate response to longitudinal stick for rotorcraft in hover, using agile actuator model Case B and Case C

Figure 4.6 shows the longitudinal frequency response of the rotorcraft-actuator sluggish model. The discrepancies between the actuators are much more apparent

in this model. This is likely due to the approximations involved in linearizing the actuator and rotorcraft system separately. Because good agreement is shown in Figures 4.4 and 4.5, and poor but acceptable agreement is shown in Figure 4.6, the linearized model is ready for further analysis.

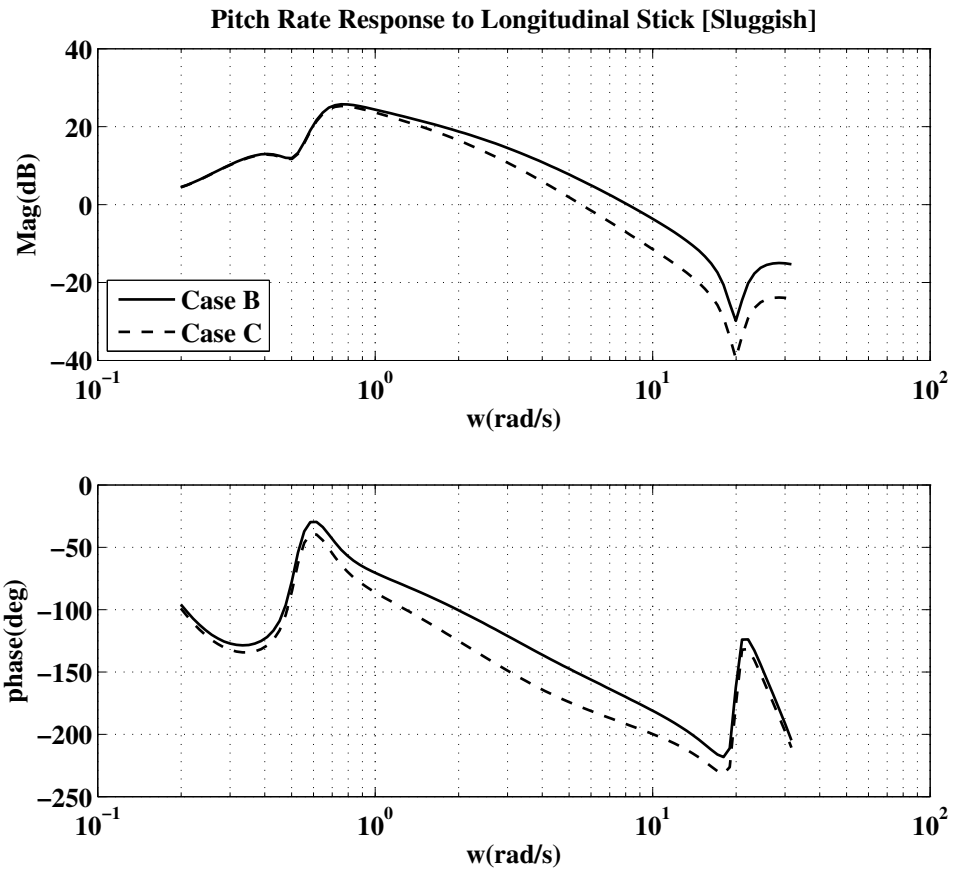

Fig. 4.6: Pitch rate response to longitudinal stick for rotorcraft in hover, using sluggish actuator model Case B and Case C

4.3 Results

4.3.1 Supply Pressure

The supply pressure was varied for the actuator model integrated with HeliUM. The simulation was run and linearized state space matrices were extracted. Supply pressures chosen for this study are listed in Table 4.1.

Parameter	Value
P_s	50 $[bar]$
P_s	125 $[bar]$
P_s	200 $[bar]$
P_s	300 $[bar]$

Table 4.1: Supply pressures used in linearized actuator-rotorcraft study

Figure 4.7 shows the rotorcraft pitch rate response to longitudinal stick. Decreasing the actuator supply pressure does not change the magnitude of the response below 10 rad/s, and decreases it only slightly at higher frequencies. The effect on phase is more significant.

The roll rate response to lateral cyclic, Fig. 4.8, and the heave response to collective, Fig. 4.9, exhibit similar behavior. At frequencies above approximately 4 rad/s, all of the responses exhibit a decrease in phase with decreasing P_s. Similar to the step response plots of Figs. 3.1 through 3.4, small changes in supply pressure at high P_s do not have a significant impacts on the frequency response. This, again, is due to the chamber flow rate increasing with the square root of supply pressure.

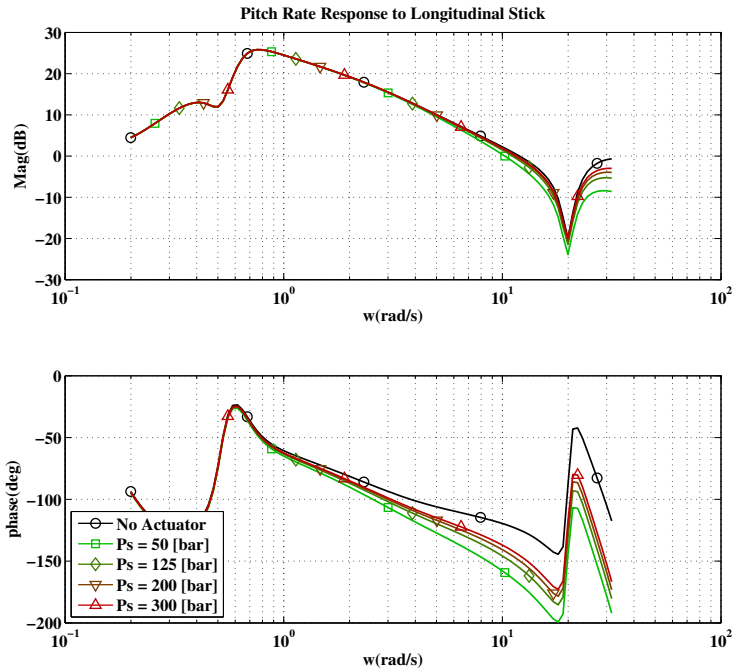

Fig. 4.7: Pitch rate response to longitudinal stick in hover as a function of supply pressure

Because of its effect on phase, supply pressure can affect handling qualities by changing bandwidth and phase delay of the pitch and roll response. Figure 4.10, taken from ADS-33 [3], summarizes the procedure by which bandwidth and phase delay can be extracted from the frequency response.

To calculate bandwidth, ω_{BW}, first the crossover frequency, ω_{180} must be calculated. This corresponds to the frequency at which the phase delay is equal to -180°. At this frequency, the gain is determined. The frequency at which the gain is 6dB higher than the gain at ω_{180} is known as the gain bandwidth $\omega_{WB_{gain}}$. The phase bandwidth, $\omega_{BW_{phase}}$ is the frequency at which the phase margin is +45°, or equivalently, the phase delay is equal to -135°. The rotorcraft bandwidth is defined

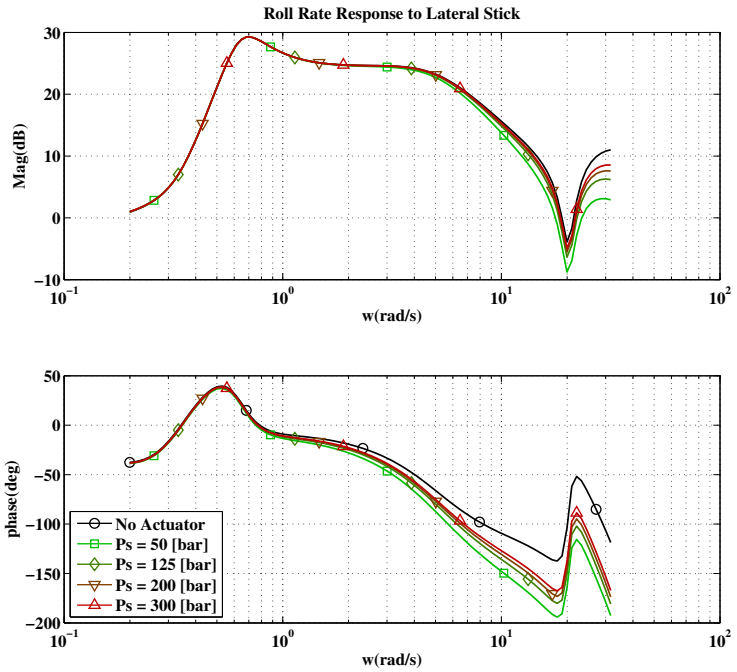

Fig. 4.8: Roll rate response to lateral stick in hover as a function of supply pressure

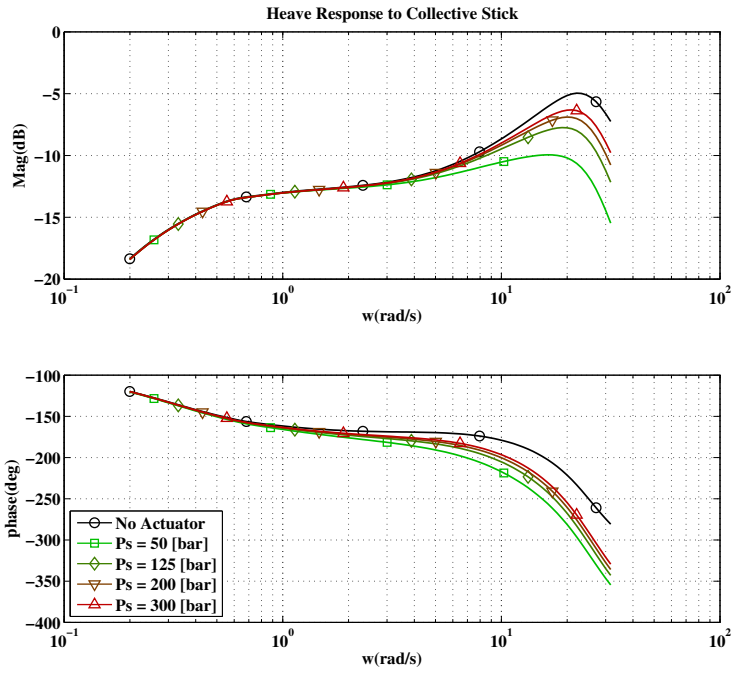

Fig. 4.9: Heave response to collective stick in hover as a function of supply pressure

as the smaller of either phase or gain bandwidth.

The phase delay, τ_p is determined by calculating the phase delay at the frequency corresponding to $2 \cdot \omega_{180}$, and taking the additional phase delay $\Delta\Phi_{2\omega_{180}}$ between ω_{180} and $2\omega_{180}$. The phase delay is then converted to time by

$$\tau_p = \frac{\Delta\Phi_{2\omega_{180}}}{\left(\frac{180}{\pi}\right)(2\omega_{180})} \tag{4.37}$$

The bandwidth and phase delay can be placed on specification charts to categorize performance based on a level of 1 to 3, from best to worst.

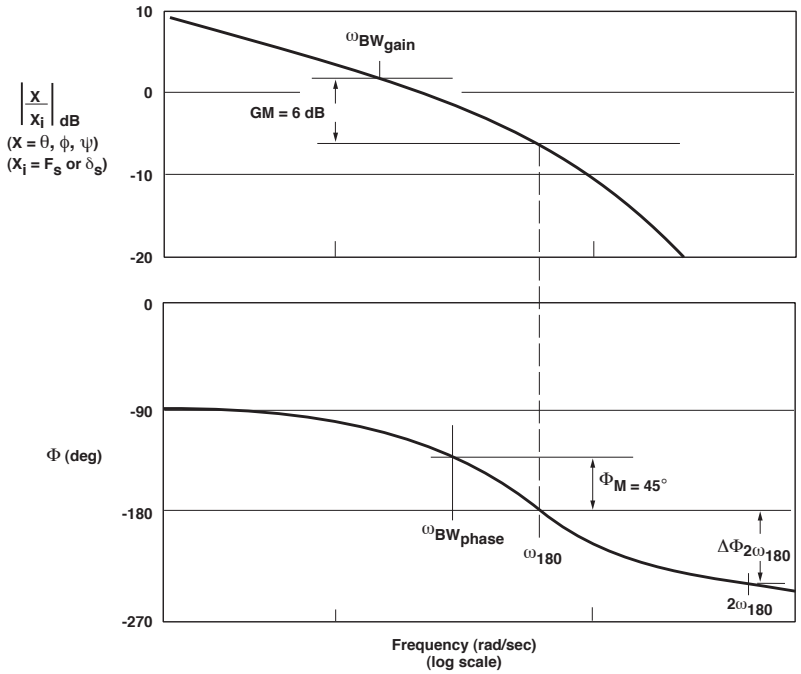

Fig. 4.10: Definitions of bandwidth and phase delay from Ref. [3]

Figure 4.11 shows the bandwidth and phase delay as a function of supply pressure. The points are placed on the ADS-33 requirements for small-amplitude pitch and roll attitudes, Paragraph 3.3.2.1, respectively [3]. In the pitch axis, as supply pressure decreases, bandwidth does not change, but phase delay increases. In a typ-

ical pitching maneuver, the rotor and rigid body inertia dominate the bandwidth calculation. It is not until much higher frequencies that the effects of the actuator add additional phase delay, which can be seen by the increasing phase delay as supply pressure decreases.

In the roll axis, bandwidth decreases and phase delay increases. Because the inertia about the roll axis, and thus delays associated with inertia, are much smaller, the additional delay due to the hydraulic system are more prominent and manifest themselves in both the bandwidth and phase delay.

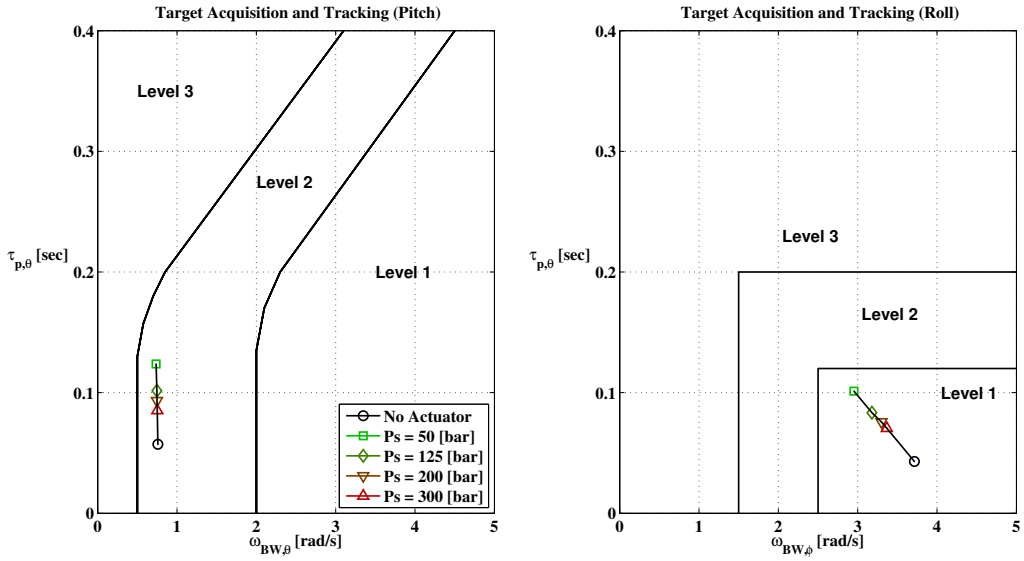

Fig. 4.11: Satisfaction of ADS-33 requirements for small-amplitude pitch and roll attitude changes for target acquisition and tracking, Par. 3.3.2.1, as a function of supply pressure.

4.3.2 Valve Pressure Drop

The simulation is repeated for changes in valve pressure drop, P_v, listed in Table 4.2. Pitch, roll, and vertical velocity frequency responses can be found in Figs 4.12, 4.13, and 4.14, respectively.

Parameter	Value
P_v	50 $[bar]$
P_v	100 $[bar]$
P_v	150 $[bar]$
P_v	199 $[bar]$

Table 4.2: Valve pressure drops used in the present study

In general, the dynamics behave similarly to those seen when adjusting supply pressure. This is to be expected, after looking at the step response characteristics in Chapter 3. This is because the flow rates Q_A and Q_B are functions of the chamber pressure differential between both supply pressure P_s and tank pressure P_T as found in Eqs. (2.22) and (2.23). Figure 4.15 places bandwidth and phase delay on the ADS-33 small-amplitude pitch and roll bandwidth handling qualities specification charts. In the pitch axis, the bandwidth remains constant and phase delay increases as the valve pressure drop decreases. This may be due to the inertial dynamics dominating rotorcraft response during a pitching maneuver at low frequencies. However, as input frequency increases, phase lag due to the actuators increases, raising the phase delay. This effect increases as the valve pressure drop decreases.

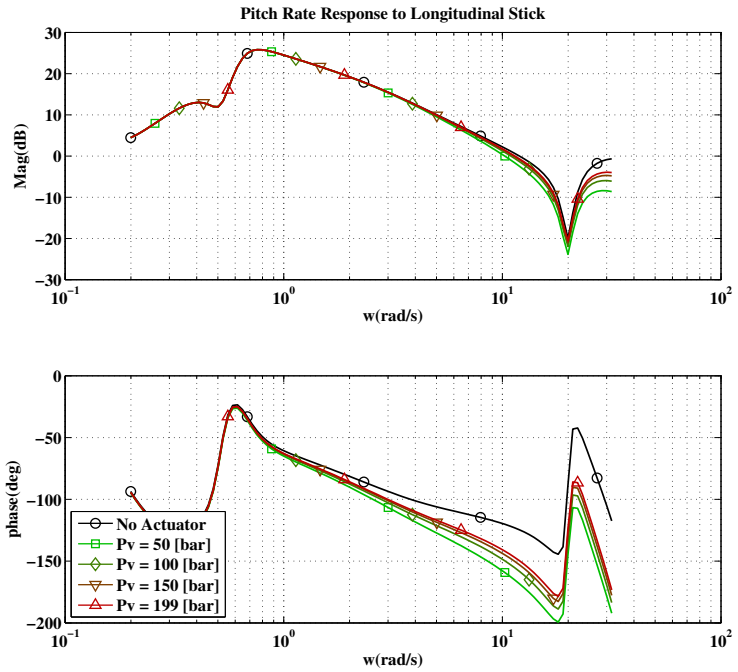

Fig. 4.12: Pitch rate response to longitudinal stick in hover as a function of valve pressure drop

4.3.3 Valve Flow Coefficient

Figures 4.16 through 4.18 show the pitch, roll, and vertical velocity frequency responses over a range of valve flow coefficients, c_v, shown in Table 4.3. This range was chosen to study the impact of rate saturation on rotorcraft dynamics.

As the valve flow coefficient decreases, the frequency response magnitude decreases and phase increases. This effect is amplified as the valve flow coefficient increase is decreased. In the heave axis the response flattens entirely out for valve flow coefficients $c_v = 5.0\text{x}10^{-7}$ and $c_v = 1.0\text{x}10^{-6}$.

Figure 4.19 shows the impact of the valve flow coefficient in terms of bandwidth and phase delay. In the pitch axis, bandwidth remains nearly constant and phase

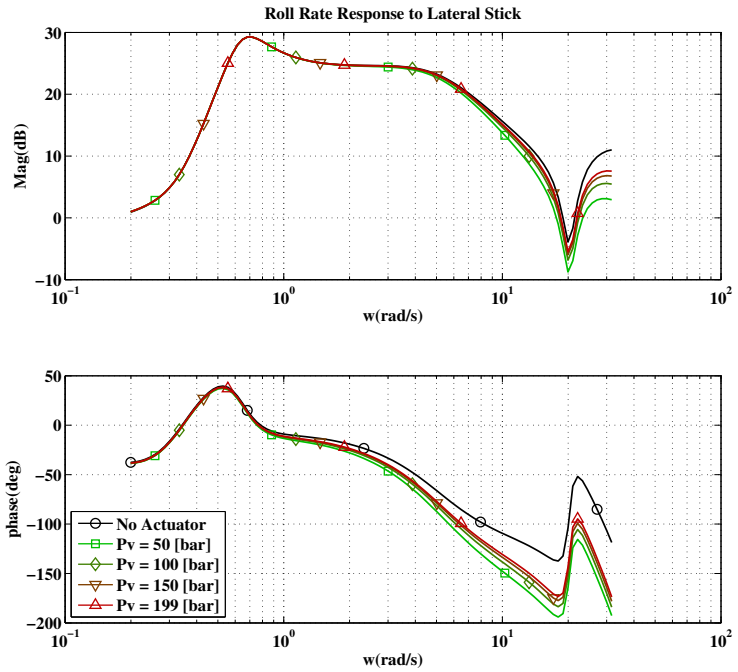

Fig. 4.13: Roll rate response to lateral stick in hover as a function of valve pressure drop

Parameter	Value
c_v	5.0x10^{-7}
c_v	1.0x10^{-6}
c_v	2.5x10^{-6}
c_v	5.0x10^{-6}

Table 4.3: Valve flow coefficients used in linearized actuator-rotorcraft study

delay increases as valve flow coefficient decreases. The actuator is rate saturated and the handling qualities level drops from 2 to 3. In the roll axis, this decrease in c_v drops the handling qualities rating from a level 1 well into the level 2 zone. This is a very significant change in both axes and can be attributed to the reduction in

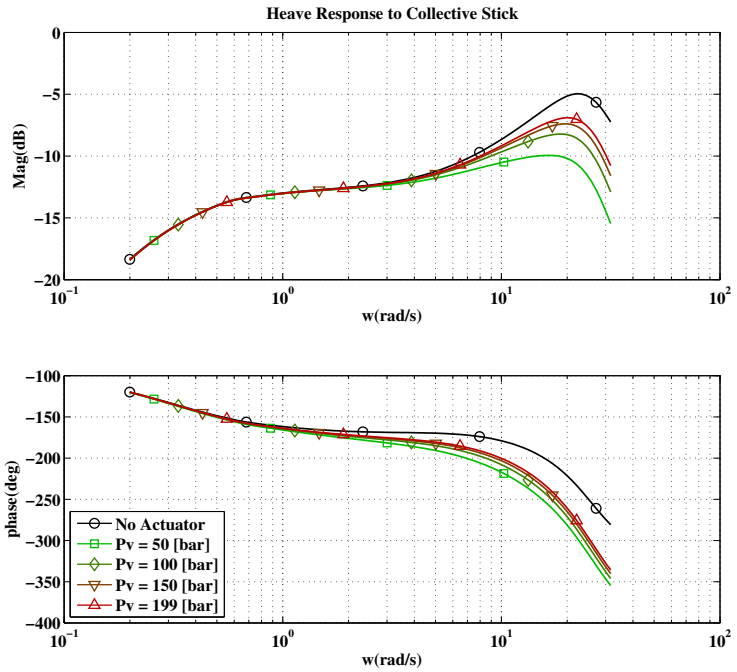

Fig. 4.14: Heave response to collective stick in hover as a function of valve pressure drop

valve flow efficiency, restricting the maximum flow rate of each actuator.

4.3.4 Piston Area

The final parameter analyzed is actuator piston area A_p. Table 4.4 details the values of piston area used for in this simulation. The results can be seen in Figures 4.4 through 4.22. The ADS-33 handling qualities are plotted in Figure 4.23 and show the piston area's significant effect on handling qualities. In the pitch axis, the phase delay increases as piston area increases. This is due to the increase in fluid required to fill each chamber as well as an increase in the surface area the pressure differential has available to generate a force. In the roll axis, bandwidth decreases

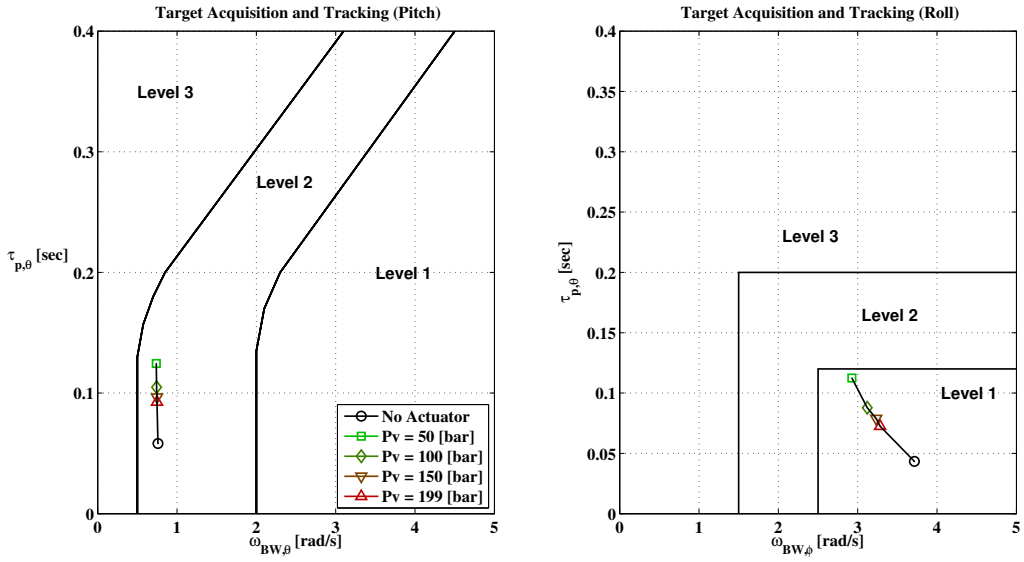

Fig. 4.15: ADS-33 requirements for small-amplitude pitch and roll attitude changes for target acquisition and tracking as a function of valve pressure drop

and the phase delay increases in response to an increasing piston area.

In Section 3.2.4 the swashplate step responses for increasing piston area are relatively quick compared to equivalent step responses for decreasing valve flow coefficient. Interestingly enough, the bandwidth and phase delay exhibit extremely similar magnitudes despite the faster rise and settling time shown by increasing actuator piston area. What the step response plots do not show, however, is the response to an oscillatory input. In the case of increasing actuator piston area, the step response appears quick and efficient but the volume of the actuator chamber creates an inertia like effect reducing the actuator's acceleration in the presence of a high frequency input.

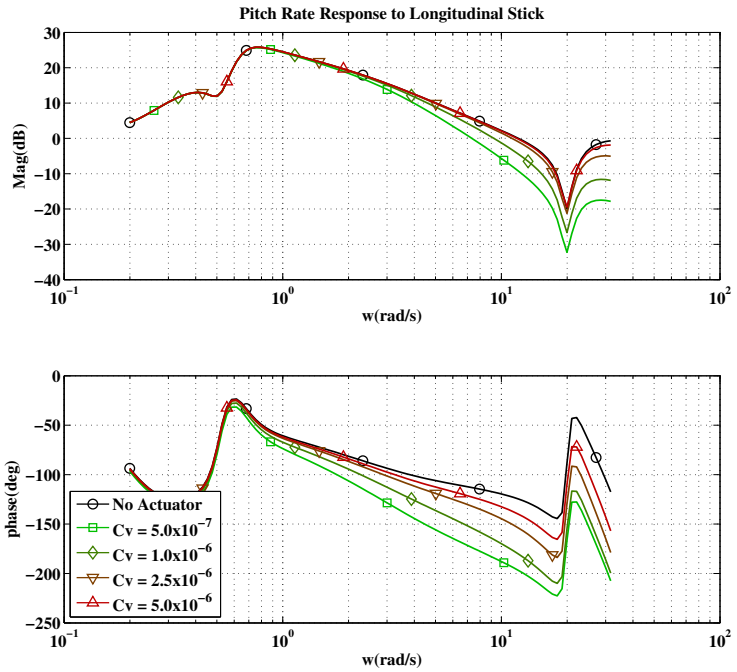

Fig. 4.16: Pitch rate response to longitudinal stick in hover as a function of valve flow coefficient

Parameter	Value
A_p	0.05 $[m^2]$
A_p	0.04 $[m^2]$
A_p	0.03 $[m^2]$
A_p	0.02 $[m^2]$
A_p	0.01 $[m^2$

Table 4.4: Piston areas used in linearized actuator-rotorcraft study

4.3.5 Actuator Test Cases

This section compares the frequency response for the four actuator types defined in Section 3.2.5. The same linearization study was performed on the baseline,

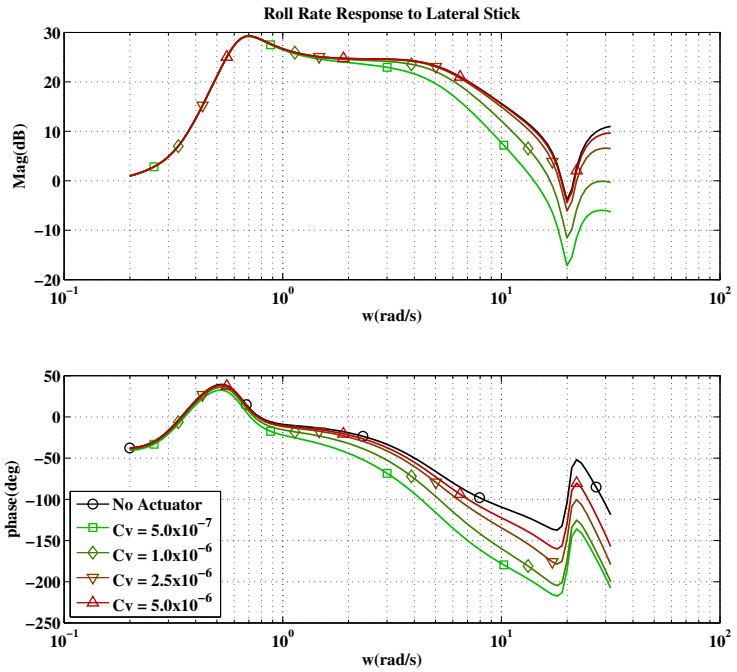

Fig. 4.17: Roll rate response to lateral stick in hover as a function of valve flow coefficient

sluggish, agile, and UH-60 actuator models. The roll and pitch frequency response data are shown in Figs. 4.24 and 4.25, respectively.

The agile actuator tracked the HeliUM model without actuators the closest. This is to be expected as the agile actuator had the shortest rise and settling time when analyzing the swashplate step response statistics. Despite the fact that the actuator was relatively quick, the phase lagged behind that of the HeliUM model above frequencies around 4 rad/s.

The baseline actuator model, configured to behave like the UH-60 transfer function model did just that. Across nearly the entire frequency spectrum, the baseline actuator and UH-60 model performed comparably.

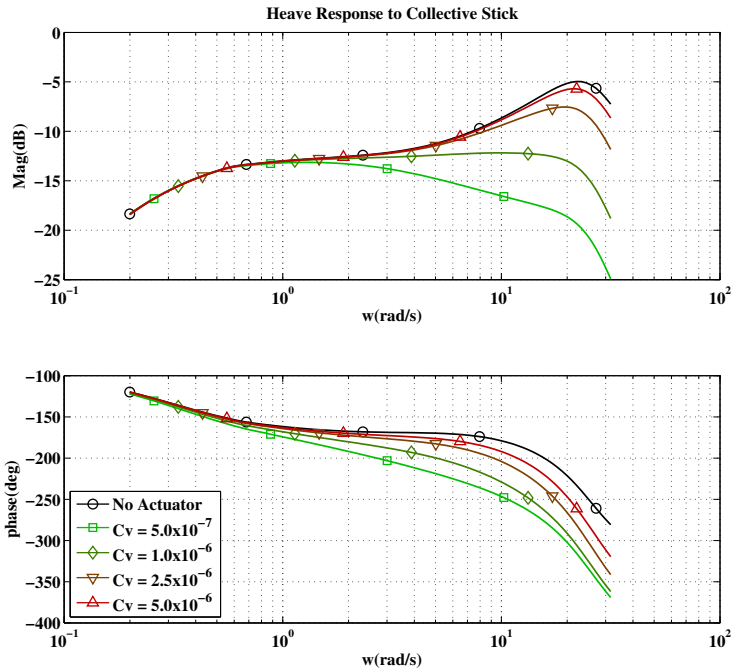

Fig. 4.18: Heave response to collective stick in hover as a function of valve flow coefficient

The slowest actuator tested, the sluggish actuator, stood out from the rest. Unlike the others, the sluggish actuator was unable to maintain a comparable magnitude response above 3 rad/s. This means that as the helicopter pilot, or control system, attempting to perform a maneuver requiring inputs around or above 0.5Hz will experience sluggish controls and difficulty maneuvering the rotorcraft.

Figure 4.26 shows the handling qualities ratings for each of the models. In the pitch axis, all models maintain the same bandwidth, and phase delay increases as the actuator is saturated. Applying the UH-60 transfer function model to the simulation increases the predicted phase delay by 77%. By applying the very fast, agile actuator model to the simulation, predicted phase delay is increased 30% and

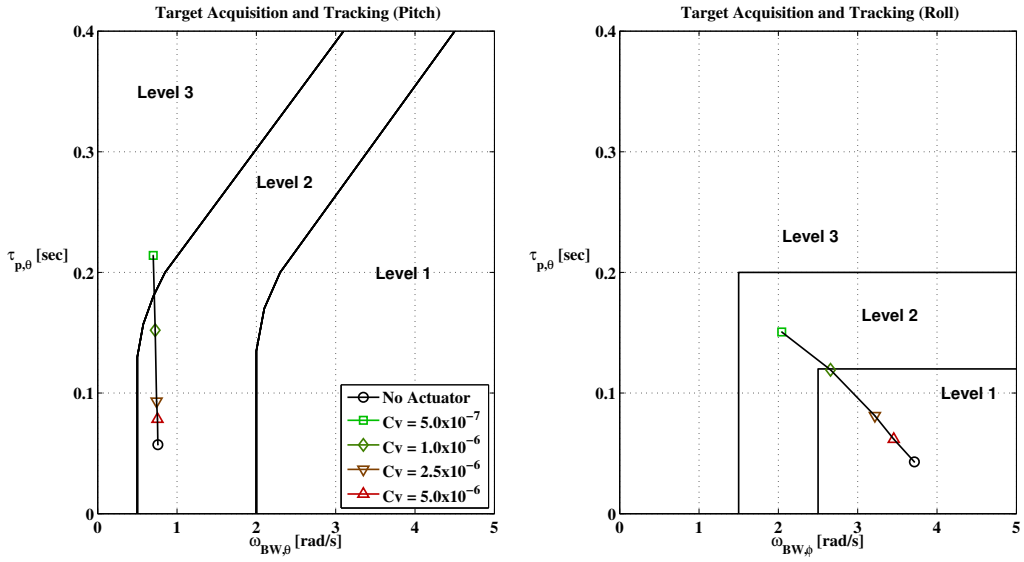

Fig. 4.19: ADS-33 requirements for small-amplitude pitch and roll attitude changes for target acquisition and tracking as a function of valve flow coefficient

by applying the sluggish actuator model to the simulation, predicted phase delay is increased 229% in the pitch axis.

In the roll axis, both bandwidth decreases and phase delay increase as the actuator models become saturated. Applying the UH-60 transfer function model to the simulation, phase delay is doubled and bandwidth decreases by 13%. The agile actuator model increases phase delay 44% and decreases bandwidth by 7%. The sluggish model increases phase delay 227% and decreases bandwidth 37%.

These numbers are significant. Based on the linearize analysis of the actuator-rotorcraft system, even a well behaved agile actuator is going to delays to the system. These delays manifest primarily as phase lag in the frequency domain and can be quantized as a decrease in bandwidth and increased phase delay.

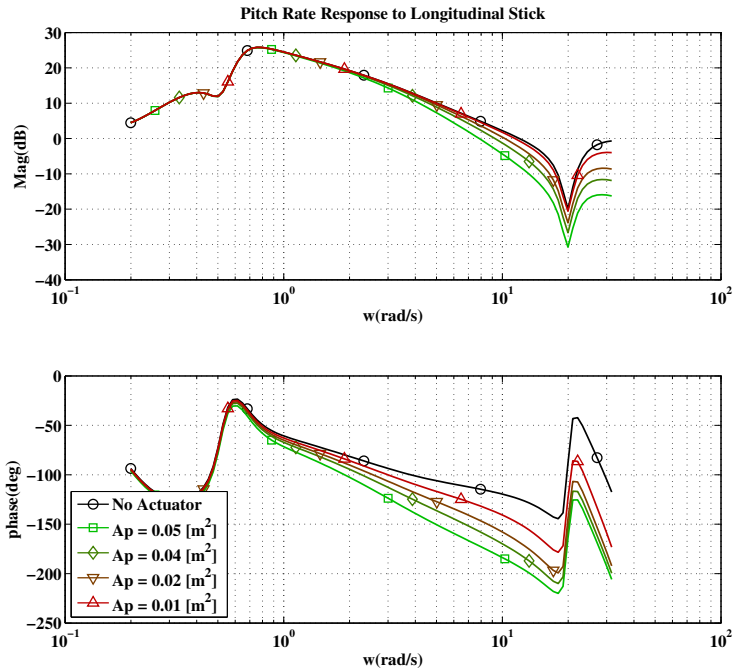

Fig. 4.20: Pitch rate response to longitudinal stick as a function of actuator piston area

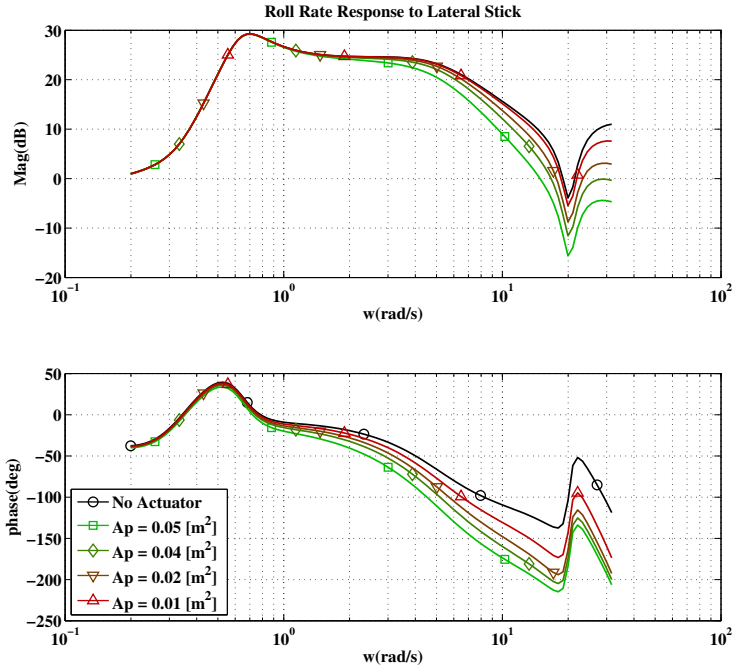

Fig. 4.21: Roll rate response to lateral stick as a function of actuator piston area

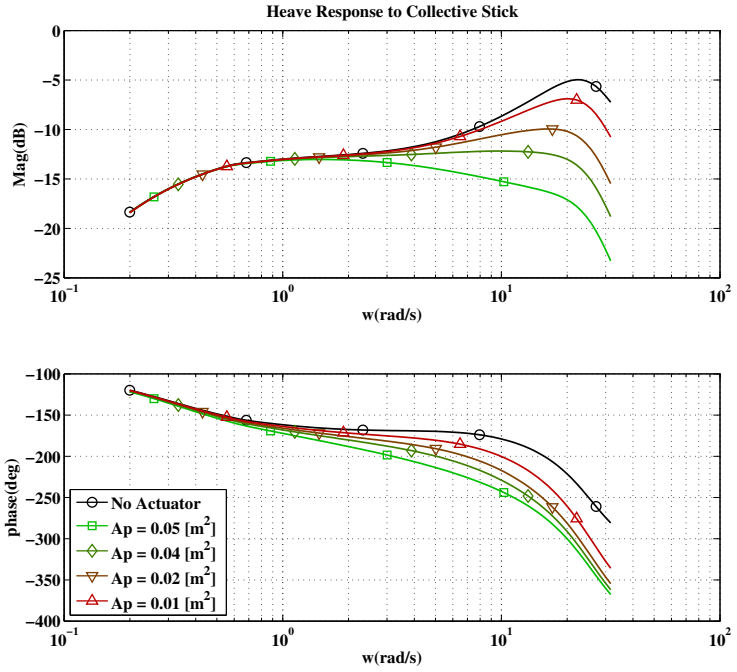

Fig. 4.22: Heave response to collective stick as a function of actuator piston area

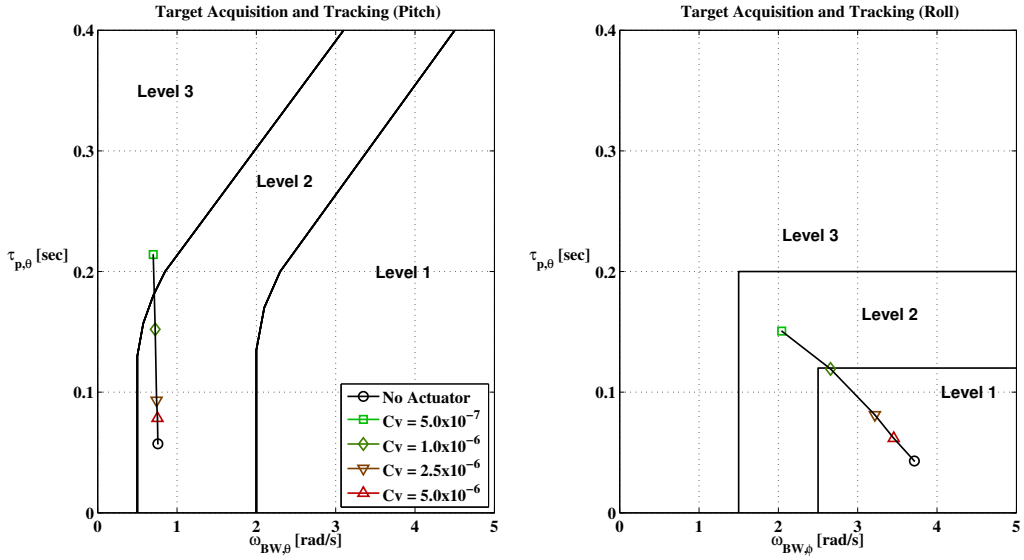

Fig. 4.23: ADS-33 requirements for small-amplitude pitch and roll attitude changes for target acquisition and tracking as a function of actuator piston area

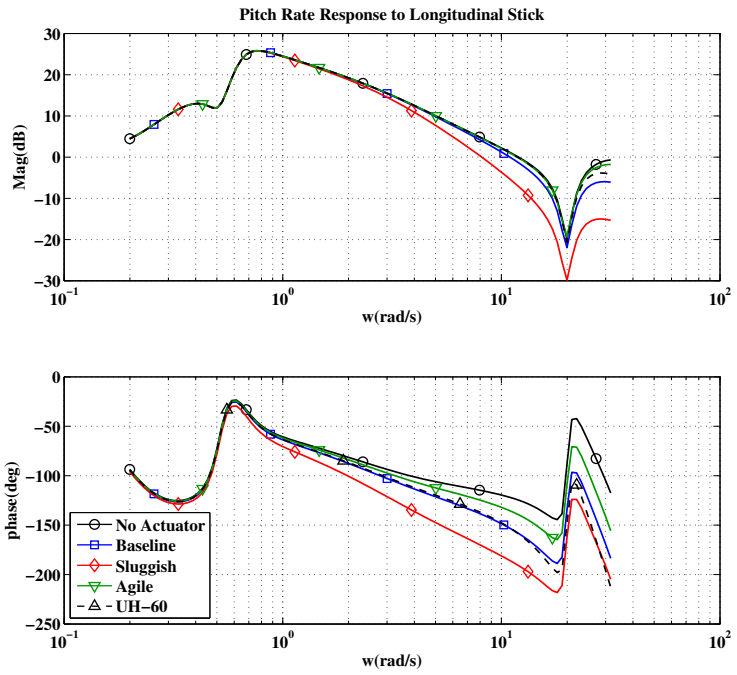

Fig. 4.24: Pitch rate response to longitudinal stick for baseline, sluggish, agile, and UH-60 transfer function models

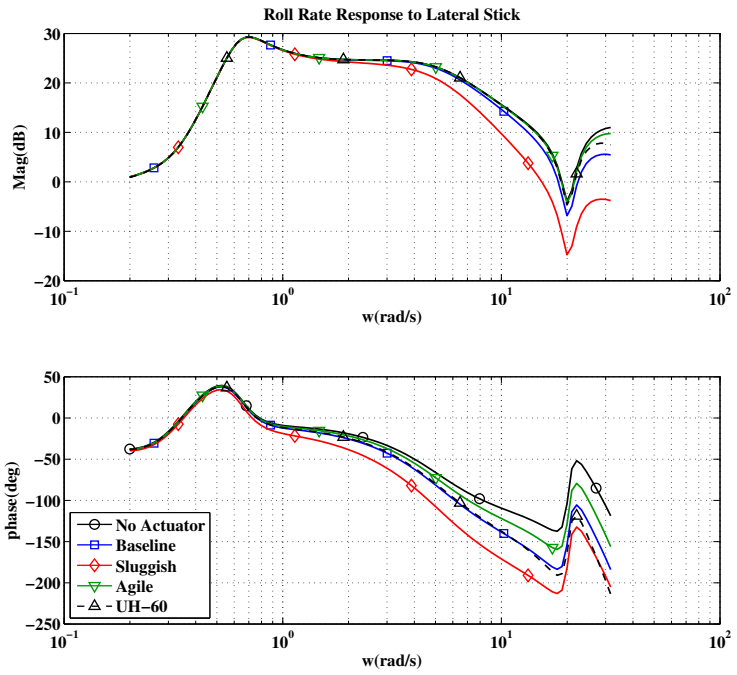

Fig. 4.25: Roll rate response to lateral stick for baseline, sluggish, agile, and UH-60 transfer function models

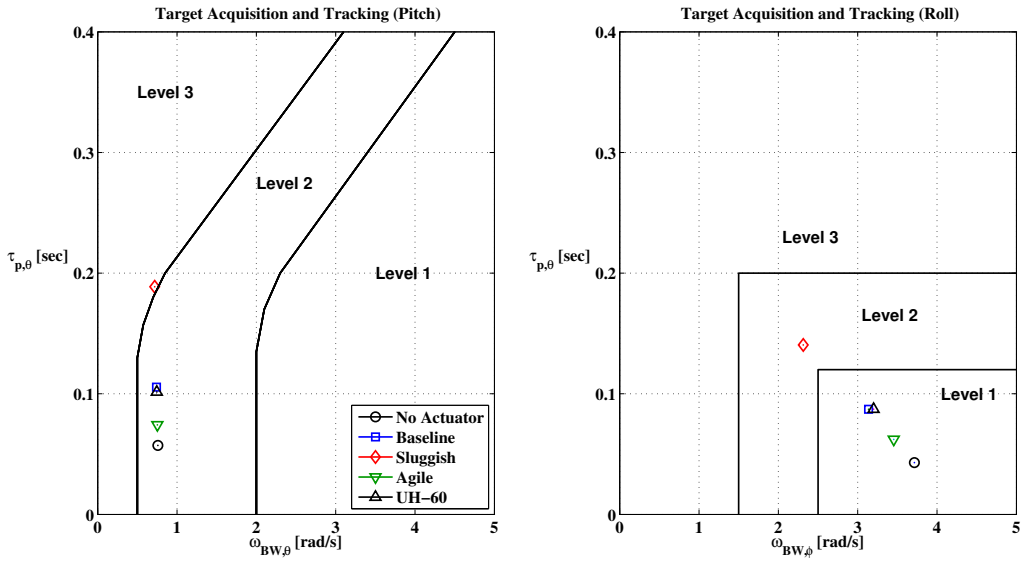

Fig. 4.26: ADS-33 requirements for small-amplitude pitch and roll attitude changes for target acquisition and tracking for baseline, sluggish, agile, and UH-60 transfer function models

Chapter 5

Rotorcraft-Actuator Time History Model

5.1 Overview

The linearized model presented in Chapter 4 was obtained by numerical perturbation of the equations of motion about a trimmed equilibrium position. This is a computationally efficient method of obtaining a linear state-space model of the coupled actuator-rotorcraft dynamics, but it may not be accurate in the presence of the nonlinearities causes by actuator saturation (both in displacement and rate). Additionally, increasing nonlinearity increases the sensitivity of the linearized model to the size of the numerical perturbations. With this in mind,the next step of the present study is to extract a linearized model using frequency domain based system identification. This model will be compared with that obtained from numerical perturbations.

5.2 CIFER

CIFER, Comprehensive Identification from FrEquency Responses, is a powerful system identification tool. CIFER was designed for rotorcraft system identification which is notoriously difficult. Rotorcraft are unstable, nonlinear aircraft with multiple flight modes. Additionally, rotorcraft dynamics are highly cross correlated

making isolation of particular single input single output much more difficult.

CIFER uses an advanced Fast Fourier Transform algorithm, the Chirp-Z transform. The single input single output (SISO) frequency response for each input/output pair is determined using a range of different window sizes. Large windows allow high resolution in time, wide dynamic range, whereas small windows allow high resolution in frequency. This is common tradeoff of using a Fourier Transform. CIFER uses a weighted nonlinear least-squares procedure to achieve a composite conditioned frequency response with good coherence and low random error of the entire frequency range of interest. More information on CIFER can be found in Ref. [**?**].

5.3 System Identification Methodology

An accurate system identification requires an input with good energy content of the frequency range of interest. In order to achieve a wide dynamic range of frequencies, a frequency sweep input is prescribed from 0.01Hz up to 60Hz. Stick input δ for a given time was calculated using

$$\delta(t) = Asin[\omega(t)t] \tag{5.1}$$

where

$$\omega(t) = \frac{t}{T}(\omega_{max} - \omega_{min}) + \omega_{min} \tag{5.2}$$

with T being the total sweep duration. An example frequency sweep is plotted in Figure 5.1

In addition to the frequency sweep on the main controls, low amplitude gaussian noise was added to the other input channels. This gaussian noise, recommended

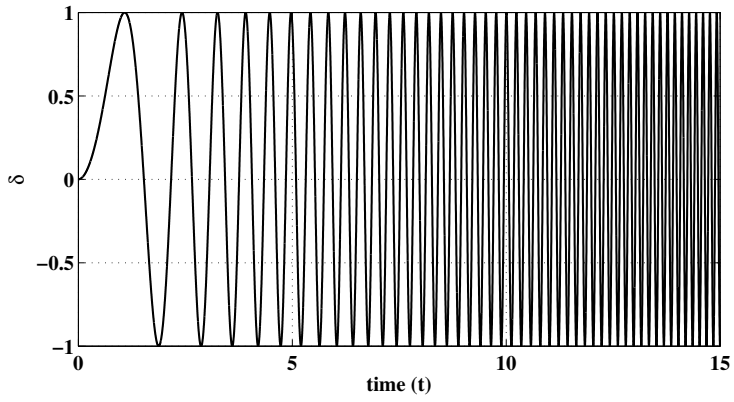

Fig. 5.1: Sample frequency sweep input function

when using CIFER for a computer simulation, helps add random high frequency content to the control signal for additional energy content. This noise is naturally present in flight test data and must be artificially added to the simulated sweep.

For each actuator configuration, the time history must be calculated for each set of dynamics of interest. A frequency sweep was performed for lateral and longitudinal dynamics for HeliUM with no actuator model and the baseline, sluggish, and agile actuator model.

5.4 Results

First frequency response data derived from CIFER is compared to the frequency response derived from the linearized model in Chapter 4. Figure 5.2 shows the magnitude and phase of pitch rate response, q, to longitudinal stick, δ_{lon}. The numerically linearized model and the identified model are similar. The coherence of the identified model, plotted at the bottom of the figure, drops at frequencies below 1 rad/s and dips around 20 rad/sec. This drop at frequencies below 0.7 rad/s is

caused by the frequency sweep length. This frequency response data was derived from a chirp signal over 300 rotor revolutions adding up to around 70 seconds per run. The dip around 20 rad/s is due to the coupled roll/rotor lag mode.

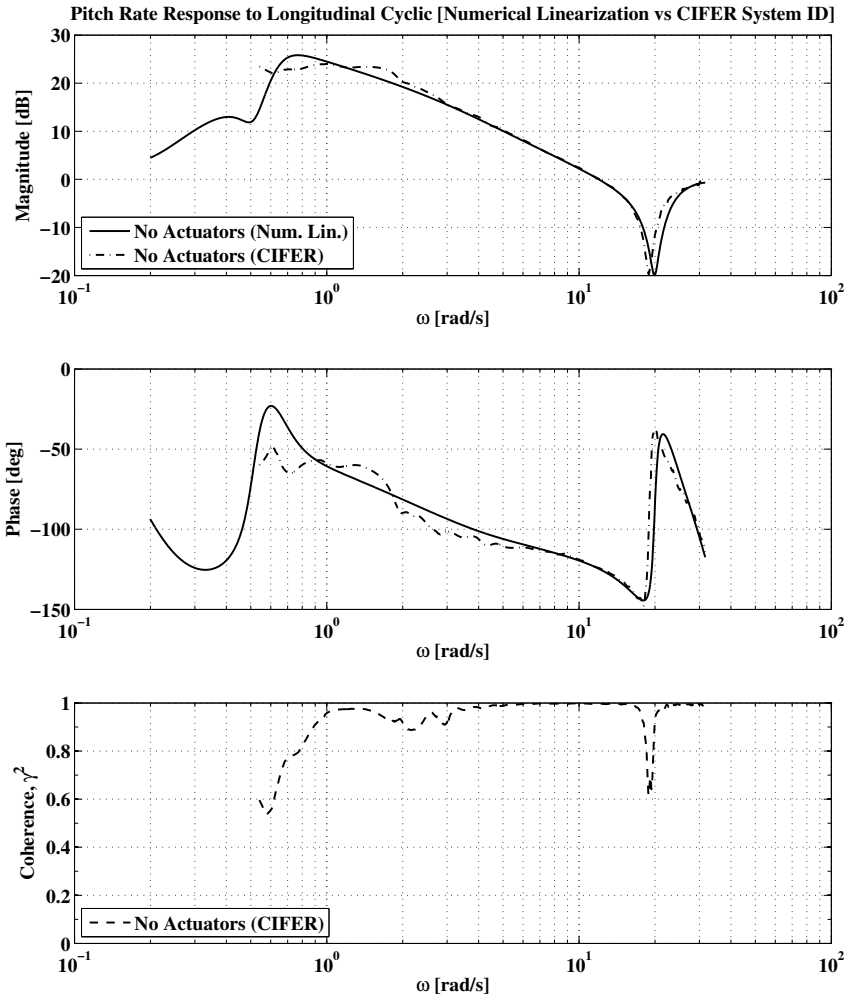

Fig. 5.2: Pitch rate frequency response to longitudinal stick δ_{lon} with no actuator dynamics model, for the numerically linearized model and the model identified using CIFER

Another area of interest is the drop of coherence if Figure 5.7 below about 2 rad/s. This plot is the roll rate frequency response with the sluggish actuator

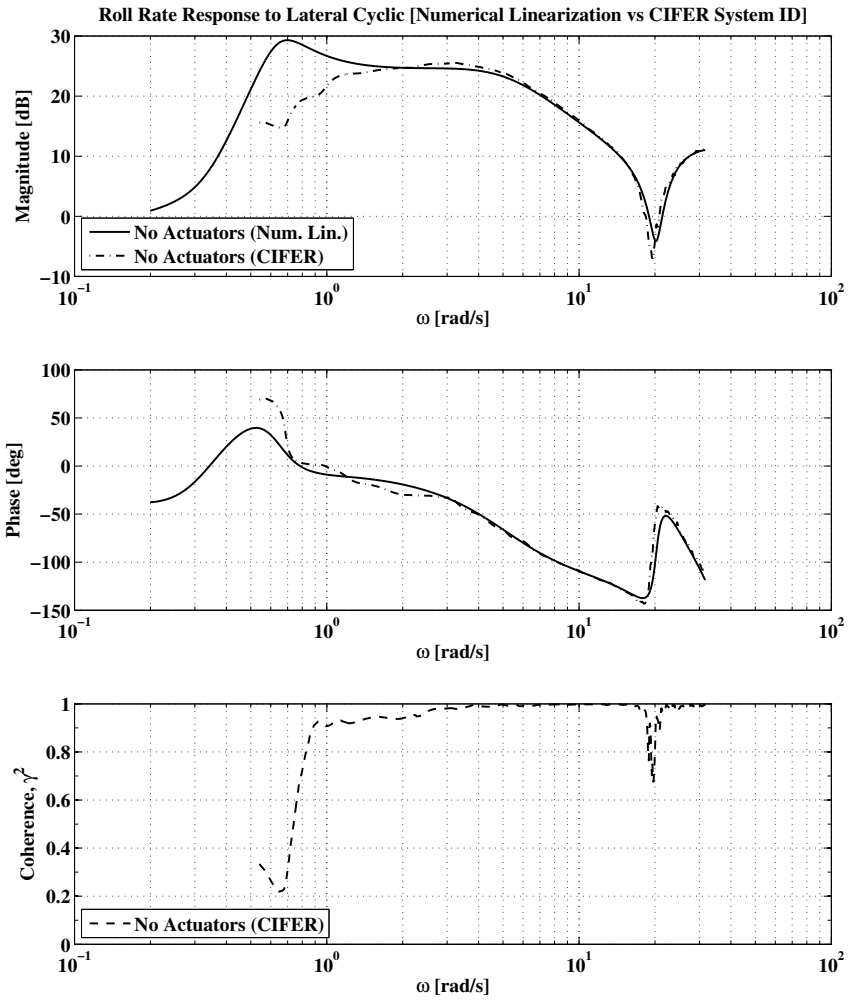

Fig. 5.3: Roll rate frequency response to lateral stick δ_{lat} with no actuator dynamics model, for the numerically linearized model and the model identified using CIFER

model. Part of this drop in coherence at low frequencies is due to the sample length as discussed previously. Another reason may be due to the nonlinear nature of the sluggish actuator at low frequencies. The agreement between the linearized and the identified model is good.

The roll and pitch bandwidth and phase delay predicted by the two models are compared in Fig. 5.10.

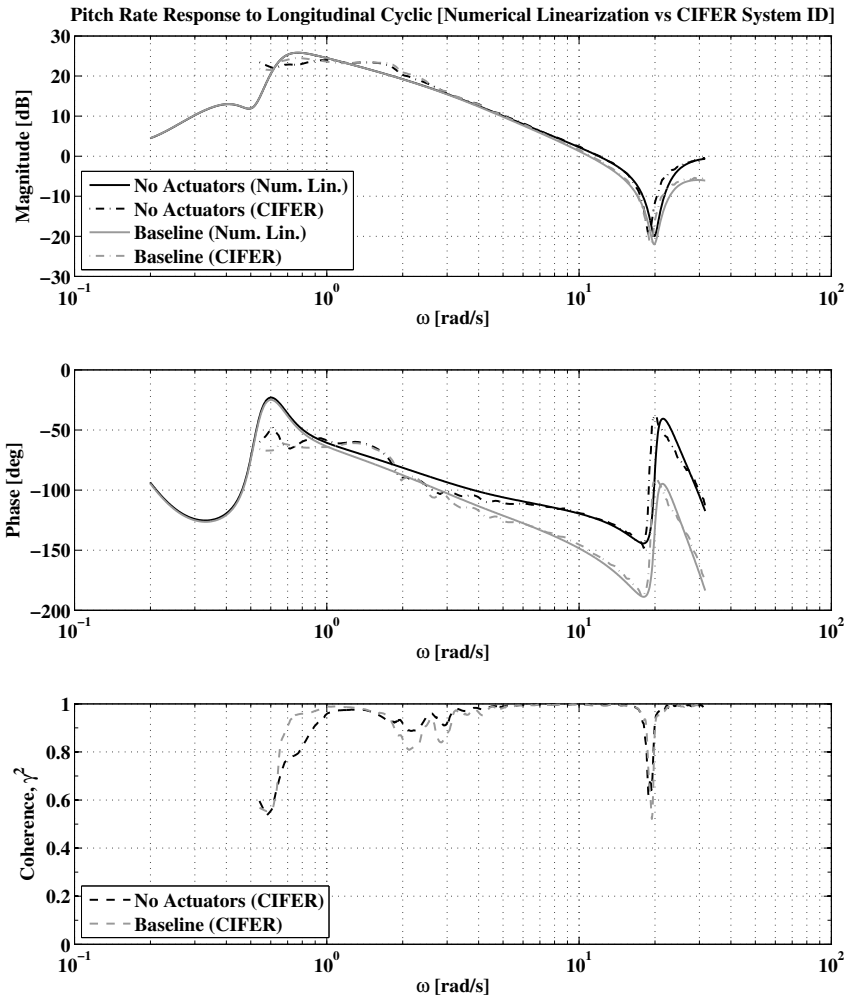

Fig. 5.4: Pitch rate frequency response to longitudinal stick δ_{lon} with baseline actuator dynamics model, for the numerically linearized model and the model identified using CIFER

Predicted pitch bandwidth is slightly higher in the linearized model for no actuator model and the baseline actuator model. Predicted phase delay, however, lower in the linearized models as compared to the identified models. The difference in phase delay for the HeliUM model is 0.022s. Additionally, linearized model underestimates the baseline model phase delay by 0.018s, the sluggish model by 0.036s,

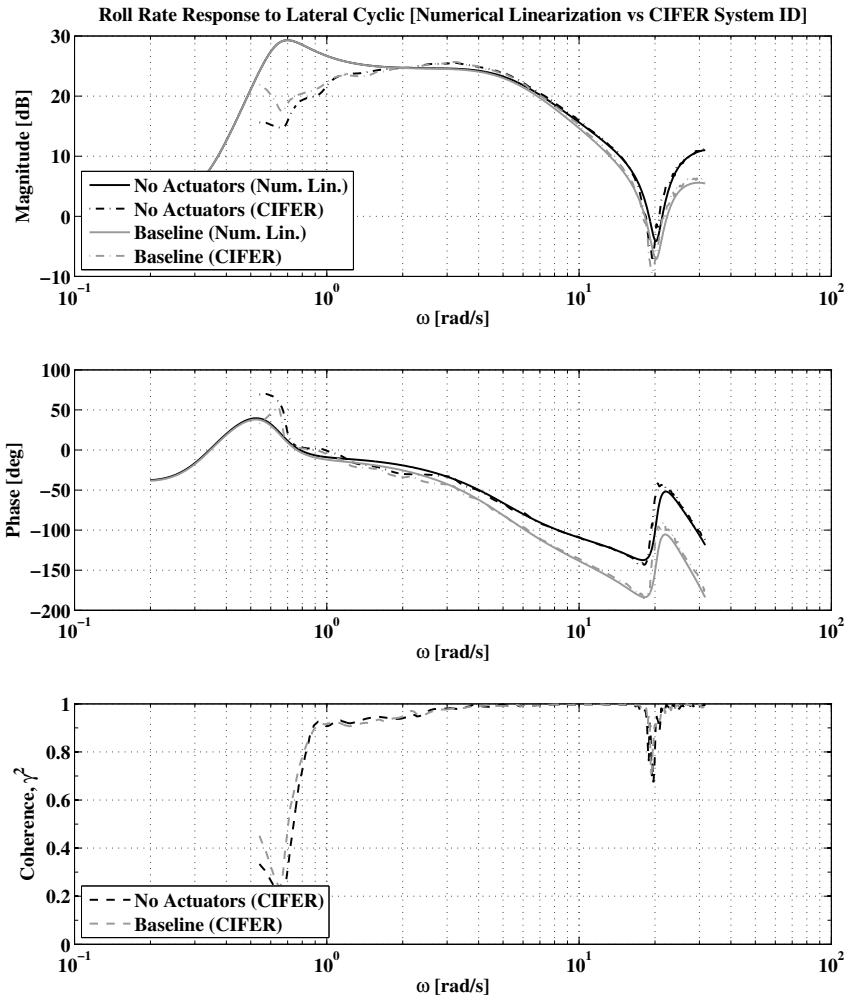

Fig. 5.5: Roll rate frequency response to lateral stick δ_{lat} with baseline actuator dynamics model, for the numerically linearized model and the model identified using CIFER

and the agile model by 0.024s. In the right situation, these differences in phase delay are enough to drive the predicted handling qualities rating from a level 2 to a level 3.

For roll, the phase delay, the equivalent between the linearized and CIFER models however the bandwidth is overestimated by the linearized model. The band-

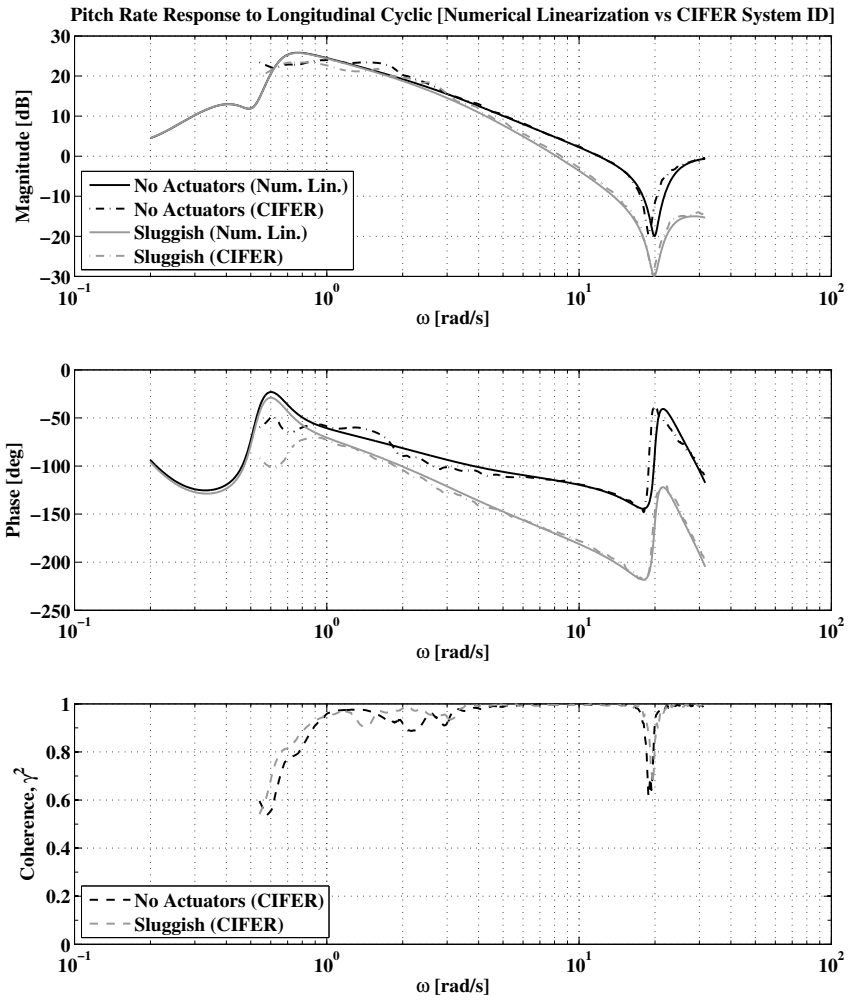

Fig. 5.6: Pitch rate frequency response of HeliUM with sluggish actuator dynamics model, for the numerically linearized model and the model identified using CIFER

width is overestimated by 0.40 rad/s for the HeliUM model, 0.68 rad/s for the baseline model, 1.05 rad/s for the sluggish model, and 0.29 rad/s for the agile model. The width of the level 2 handling qualities requirement is 1 rad/s. The sluggish actuator model shows a discrepancy over 1 rad/s meaning the accuracy of the model can make the difference between an excellent performing rotorcraft and a poorly performing rotorcraft.

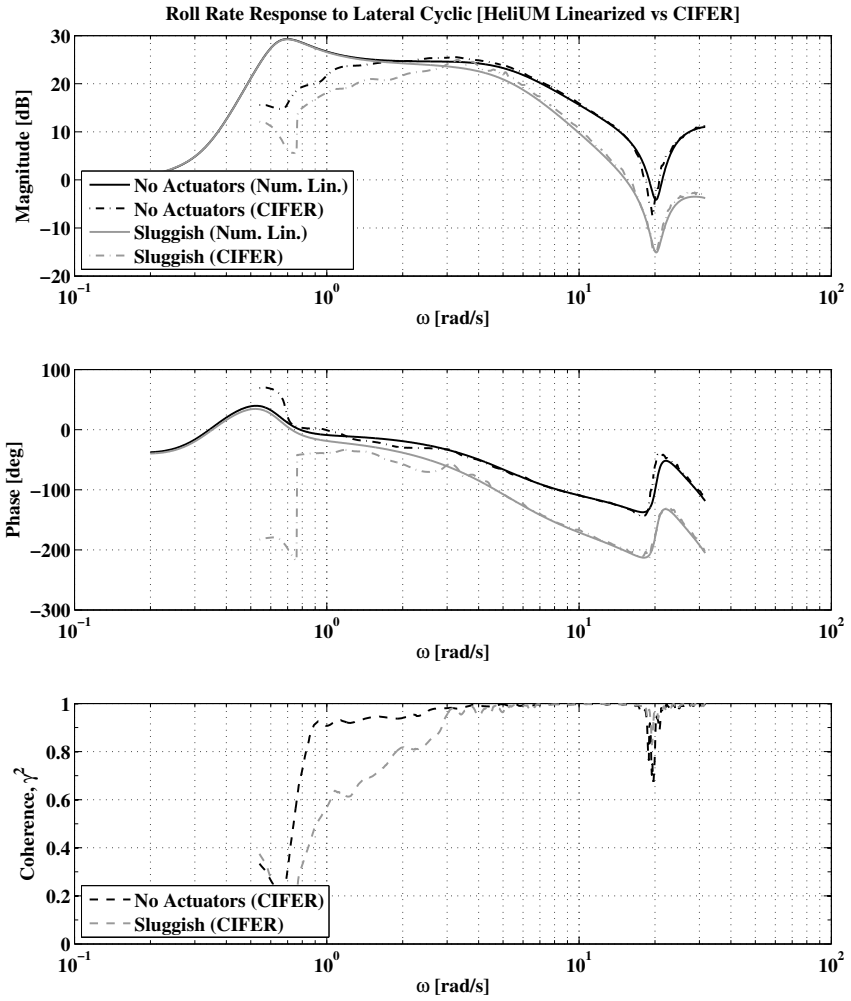

Fig. 5.7: Roll rate frequency response of HeliUM with sluggish actuator dynamics model, for the numerically linearized model and the model identified using CIFER

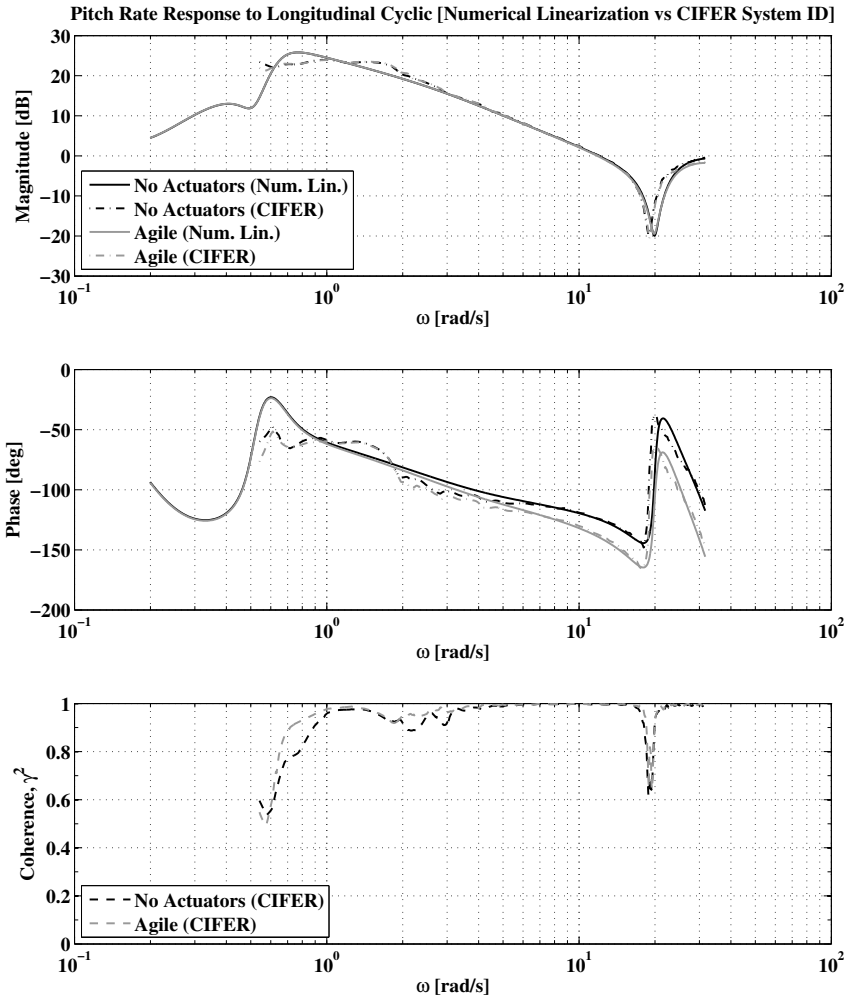

Fig. 5.8: Pitch rate frequency response of HeliUM with agile actuator model, for the numerically linearized model and the model identified using CIFER

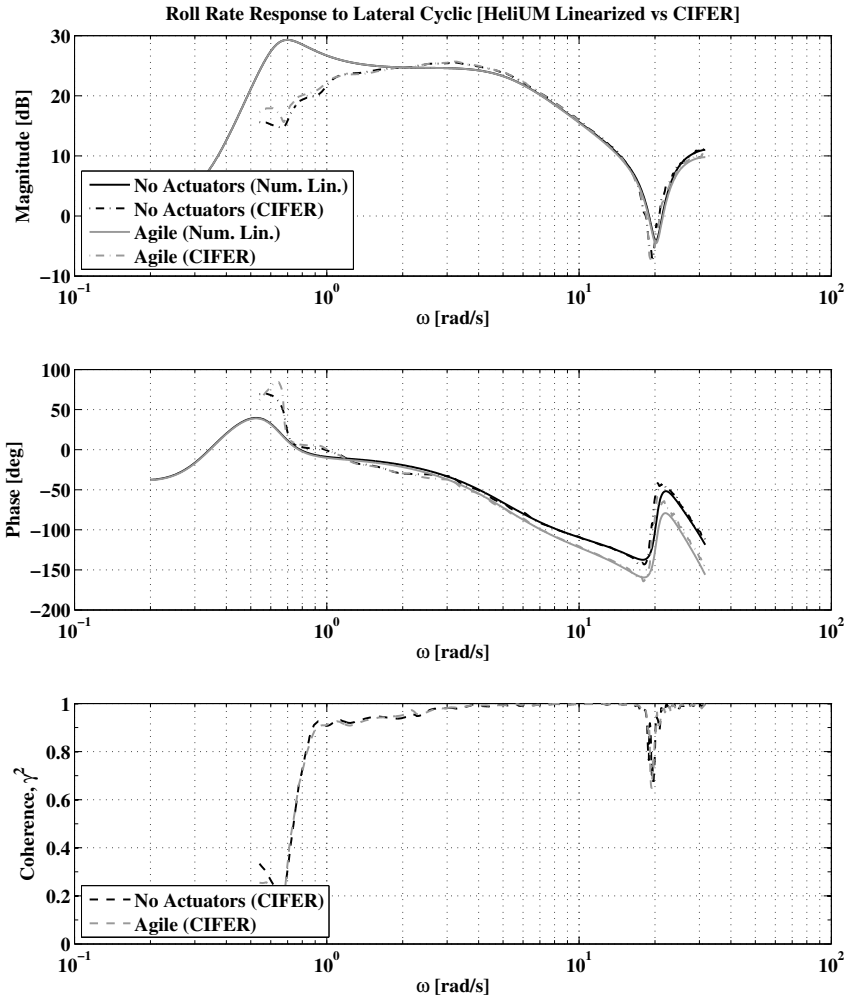

Fig. 5.9: Roll rate frequency response of HeliUM with agile actuator model, for the numerically linearized model and the model identified using CIFER

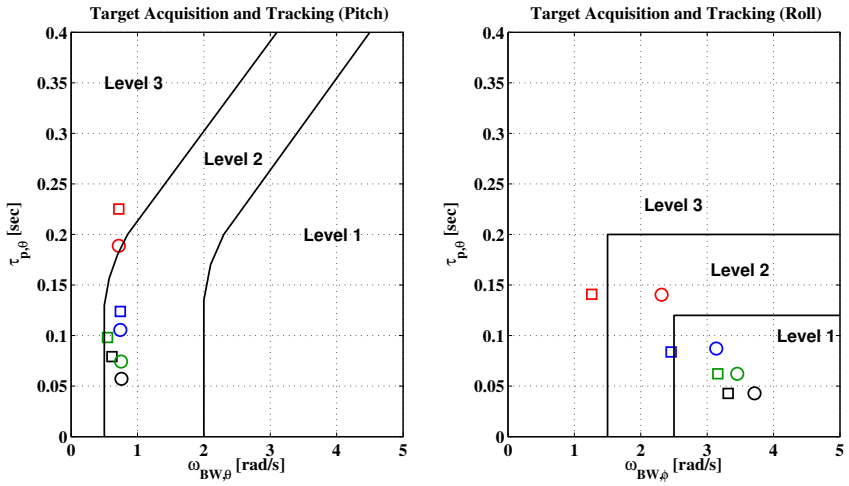

Fig. 5.10: ADS-33 requirements for small-amplitude pitch and roll attitude changes for target acquisition and tracking without actuators (black), baseline (blue), sluggish (red), and agile (green) models derived from numeric linearization (circles) and CIFER (squares)

Chapter 6

Concluding Remarks

6.1 Overview

Development of a high fidelity actuator model is necessary for accurate high frequency modeling of rotorcraft. As rotorcraft performance requirements increase, the demand for high bandwidth controllers to augment pilot operation of rotorcraft becomes paramount. Actuators are a key component of the control system and they exhibit nonlinearities at high frequency that can have a negative impact on predicted versus actual rotorcraft performance.

First a nonlinear state space actuator model was developed. Six first-order implicit differential equations were used to describe a single actuator. Three actuators composed the simplified rotorcraft hydraulic system for a total of 18 first-order differential equations. The actuators were integrated into the nonlinear state space rotorcraft model, HeliUM, by intercepting pilot stick inputs and rerouting them to the actuator dynamics. The actuator dynamics then fed back their positions to the helicopter model for an accurate representation of the swashplate.

A parametric study was performed on the swashplate-actuator dynamics, first ignoring the rotorcraft model. Step responses were generated for a variety of key hydraulic parameters and their effects analyzed.

With knowledge of the essential actuator-swashplate interaction, the entire

coupled actuator-rotorcraft system was used to investigate the effects of actuator dynamics on a rotorcraft. A linearized model was derived using first-order Taylor series expansion over a variety of key hydraulic parameters. The coupled actuator-rotorcraft dynamics were analyzed in the frequency domain through the use of Bode plots and key flight dynamics quantities such as bandwidth and phase delay.

Time integration over several hundred blade revolutions was performed for a series of three hydraulic configurations, a baseline, a saturated actuator, and an unsaturated actuator. The coupled system was subjected to frequency sweeps about the longitudinal and lateral axis to extract a more accurate frequency response representation encompassing all the nonlinear effects of both the actuator and the rotorcraft. The software package CIFER was used to convert the time history frequency sweep data into accurate frequency response data through the use of an advanced Fourier algorithm.

The full nonlinear CIFER model was then compared to the first order Taylor series linearized model derived previously. Observations are made regarding the differences between the linearized and CIFER models for the three actuator models and handling qualities parameters bandwidth and phase delay for the models is discussed.

6.2 Conclusion of the Study

1. Hydraulic model parameters such as supply pressure, pressure drop, valve coefficients, and actuator piston are all have a unique roll in the overall dy-

namics of the hydraulic system. Actuator design must be carefully considered to optimize these parameters for the coupled actuator-swashplate system.

2. An reasonably accurate linearized model of the actuator-rotorcraft system can be constructed using a small perturbation first-order Taylor series method. This model can be used to analyze key flight dynamics parameters such as bandwidth and phase delay. The inclusion of actuator dynamics can have a significant role on the predicted handling qualities of rotorcraft in hover.

3. The coupled actuator-rotorcraft linearized model can be validated using independent linearization of actuator and rotorcraft dynamics.

4. Coupled actuator-rotorcraft time history frequency sweep data can be used to reconstruct the lateral and longitudinal frequency response of rotorcraft in hover. Actuator dynamics, including nonlinear rate saturation, play an important role in rotorcraft frequency response.

5. The derived linearized model frequency response and time history frequency response were cross-validated. Key differences in flight dynamics parameters such and bandwidth and phase delay are noted between the models.

6.3 Remarks for Future Work

The findings presented in this paper only lay the framework for future work. Rotorcraft fly many different flight conditions and the coupled actuator-rotorcraft interaction can be of use. The actuator model presented here can be used and

expanded for future work.

1. Forcing on the actuator plays a large role in the overall actuator dynamics and can be seen in the analysis of valve pressure drop on rotorcraft dynamics. When rotorcraft perform aggressive maneuvers, nonstandard loads can be placed on the rotor and transferred to the swashplate. By simulating rotorcraft maneuvers with the coupled actuator-rotorcraft system, the effects of time-varying loads can be analyzed.

2. The actuator model described uses specialized constraint equations to keep actuator displacement within normal operating limits. Placing the actuator-rotorcraft under certain conditions, can excite the dynamics associated with the physical limits of the actuator. By simulating the coupled system dynamics in this compromised position could yield valuable insight into the limits of the flight envelope.

3. As more and more rotorcraft rely on hydraulic flight control systems, the opportunity for failure increases. Various hydraulic system failures can be analyzed and flight dynamics extracted. Failures such as a locked actuator, a leaking pipeline, and air entrained in the hydraulic fluid can have disastrous real world consequences and should be studied in further detail by simulation.

4. The model presented has simplifying assumptions and simulates a single stage servo valve and actuator. A higher fidelity model including a multi-stage valve, hydraulic pumps, and pipelines could serve as a useful tool going forth. The

hydraulic systems on modern rotorcraft are highly complex, featuring trim actuators, stability augmentation actuators, boost actuators and complex swashplate arrangements can create quite a complex coupled system. Simulating such dynamics could prove useful to optimizing such complex arrangements.

The research presented in this thesis provides merely a framework for the understanding of the complex interactions between the coupled actuator-rotorcraft dynamic system. Such a system can become infinitely complex leaving many avenues for future research.

Bibliography

[1] Howlett, J., "UH-60 Black Hawk Engineering Simulation Program: Volume 1 - Mathematical Model," Tech. rep., Sikorsky Aircraft.

[2] Jelali, M. and Kroll, A., *Hydraulic Servo-systems: Modelling, Identification and Control*, Springer-Verlag London Limited.

[3] "Aeronautical Design Standard Performance Specification Handling Qualities Requirements for Military Rotorcraft," Tech. rep.

[4] Dieterich, O., Götz, J., Vu, B. D., Haverdings, H., Masarati, P., Pavel, M., Jump, M., and Gennaretti, M., "Adverse Rotorcraft-Pilot Coupling: Recent Research Activities in Europe," 34th European Rotorcraft Forum, Liverpool, UK, September 2008.

[5] Serafini, J., Gennaretti, M., Masarati, P., Quaranta, G., and Dieterich, O., "Aeroelastic and Biodynamic Modelling for Stability Analysis of Rotorcraft-Pilot Coupling Phenomena," 34th European Rotorcraft Forum, Liverpool, UK, September 2008.

[6] Ashkenas, I. L., Jex, H. R., and McRuer, D. T., "Pilot-Induced Oscillations: Their Cause and Analysis," Tech. rep.

[7] Mitchell, D. G., Kish, B. A., and Seo, J. S., "A Flight Investigation of Pilot Induced Oscillation Due to Rate Limiting," Aerospace Conference, 1998 IEEE , Vol. 3, March 1998, pp. 5974.

[8] Tischler, M. B. and Cauffman, M. G., "Frequency-Response Method for Rotorcraft System Identification with Applications to the BO 105 Helicopter," American Helicopter Society 46th Annual Forum, Washington, D.C., May 1990.

[9] Fu, K. H. and Kaletka, J., "Frequency-Domain Identification of BO 105 Derivative Models with Rotor Degrees of Freedom," 16th European Rotorcraft Forum, Glasgow, UK, September 1990.

[10] Shim, D. H., Kim, H. J., and Sastry, S., "Control System Design for Rotorcraft-based Unmanned Aerial Vehicles using Time-domain System Identification," International Conference on Control Applications, Anchorage, AK, September 2000.

[11] Tischler, M. B., Fletcher, J. W., Morris, P. M., and Tucker, G. T., "Applications of Flight Control System Methods to an Advanced Combat Rotorcraft," Tech. rep., National Aeronautics and Space Administration, Ames Research Center, Moffett Field, CA 94035.

[12] Chen, R. T. N. and Hindson, W. S., "Influence of High-Order Dynamics on Helicopter Flight Control System Bandwidth," 11th European Rotorcraft Forum, London, UK, September 1985.

[13] Ballin, M. G. and Dalang-Secrétan, M.-A., "Validation of the Dynamic Response of a Blade-Element UH-60 Simulation Model in Hovering Flight," 46th Annual Forum of the American Helicopter Society, Washington, D.C., May 1990.

[14] Fletcher, J. W., "A Model Structure for Identification of Linear Models of the UH-60 Helicopter in Hover and Forward Flight," Tech. rep.

[15] Mitchell, D. G. and Sahasrabudhe, V., "Determining Bandwidth in the presence of Nonlinearities," 37th AIAA Aerospace Sciences Meeting and Exhibit, Reno, NV, January 1999.

[16] Nikiforuk, P., Ukrainetz, P. R., and Tsai, S. C., "Detailed Analysis of a Two-Stage Four-Way ElectroHydraulic Flow-Control Valve," *Journal of Mechanical Engineering Science*, April 1969.

[17] van Schothorst, G., *Modelling of Long-Stroke Hydraulic Servo-Systems for Flight Simulator Motion Control and System Design*, Ph.D. thesis, Technische Universiteit Delft.

[18] Stribeck, R., "Die wesentlichen Eigenschaften der Gleitund Rollenlager," Zeitschrift des Vereins Deutscher Ingenieure, No. 36, 1902, pp. 13411348.

[19] Lee, K., "Dynamisches Verhalten der Steuerkette Servoventil-Motor-Last," dissertation, Technical University of Aachen, Aachen, Germany, 1977.

[20] Walters, R., *Hydraulic and Electric-Hydraulic Control Systems*, Second Enlarged Edition, Kluwer Academic Publishers, 2000.

[21] P. N. Brown, A. C. Hindmarsh, and L. R. Petzold, Using Krylov Methods in the Solution of Large-Scale Differential-Algebraic Systems, SIAM Journal of Scientific Computing, 15 (1994), pp. 1467-1488.

[22] P. N. Brown, A. C. Hindmarsh, and L. R. Petzold, Consistent Initial Condition Calculation for Differential-Algebraic Systems, SIAM Journal of Scientific Computing, 19 (1998), pp. 1495-1512.

[23] Howlett, J., "UH-60 Black Hawk Engineering Simulation Program: Volume 2 - Background Report," Tech. rep., Sikorsky Aircraft.

[24] Turnour, S. R., '*Flight Dynamics Modeling of Hingeless and Bearingless Rotor Helicopters*, Ph.D. thesis, University of Maryland, College Park, MD, 1996.

[25] Ballin, M. G., "Validation of Real-Time Engineering Simulation of the UH-60A Helicopter," Tech. rep., NASA,

[26] Kim, F. D., Celi, R., and Tischler, M. B., "High Order State Space Simulation Models of Helicopter Flight Mechanics," *Journal of the American Helicopter Society*, Vol. 38, October 1993.

[27] Turnour, S. R. and Celi, R., Modeling of Flexible Blades for Helicopter Flight Dynamics Applications, *Journal of the American Helicopter Society*, Vol. 41, January 1996.

[28] Spence, A. M., *A Design-Oriented Aeromechanical Analysis for Hingeless Rotor Helicopters in Straight and Turning Flight*, Ph.D. thesis, University of Maryland, College Park, MD, 1994.

[29] He, C. J. and Peters, D. A., "Optimization of Rotor Blades for Combined Structural, Performance, and Aeroelastic Characteristics," Structural Optimization, Vol. 5, December 1992.

[30] Theodore, C. R., *Helicopter Flight Dynamic Simulation with Refined Aerodynamics Modeling*, Ph.D. thesis, University of Maryland, College Park, MD, 2000.

[31] Shamie, J. and Friedmann, P. P., "Effect of Moderate Deflections on the Aeroelastic Stability of a Rotor Blade in Forward Flight," Proceedings of the 3rd Annual European Rotorcraft and Powered Lift Aircraft Forum, No. Aix-en-Provence, France, September 1977.